IPP-Report

Max-Planck-Institut für Plasmaphysik

Tobias Max-Josef Engelhardt

Comparing the fuelling performance of gas and pellets in the all-metal-wall tokamak ASDEX Upgrade

IPP 2021-10
Juni 2021

HOCHSCHULE COBURG

Max Planck Institute
for Plasma Physics

University of Coburg
Faculty of Applied Sciences

Department of Technical Physics

Bachelor Thesis

submitted for the degree of

Bachelor of Engineering

Comparing the fuelling performance of gas and pellets
in the all-metal-wall tokamak
ASDEX Upgrade

by

Tobias Max-Josef Engelhardt
Matriculation Nr.: 01513817

Submission Date: November 26, 2020
Supervisors: Prof. Dr. Martin Prechtl, Dr. Peter Lang

Erklärung der Urheberschaft

Ich erkläre hiermit an Eides statt, dass ich die vorliegende Arbeit ohne Hilfe Dritter und ohne Benutzung anderer als der angegebenen Hilfsmittel angefertigt habe; die aus fremden Quellen direkt oder indirekt übernommenen Gedanken sind als solche kenntlich gemacht. Die Arbeit wurde bisher in gleicher oder ähnlicher Form in keiner anderen Prüfungsbehörde vorgelegt und auch noch nicht veröffentlicht.

Ort, Datum Unterschrift

Abstract

A dataset, containting data from pellet-fuelled discharges in the high density regime of the Tokamak ASDEX Upgrade with full tungsten plasma facing components has been collected. The dataset covers eight years of operation with several methods to achieve high performance e.g. Nitrogen Seeding or high plasma shaping as well as scenarios of moderate performance.

Analysis [1] has shown, that beyond the Greenwald density n_{Gw} enhanced confinement, gained by several methods cannot be maintained. A rising separatrix density $n_{e,sep}$ was assumed to be a pivotal reason for this feature, analysis has shown, that a loss in confinement seems likely when the separatrix density is increased. Therefore, a scenario to control the separatrix (edge-) density had to be developed. Furthermore, the dependence between $n_{e,sep}$ and the neutral divertor density n_0^{Div} has been observed. For this dataset, the separatrix density was derived from available data of Thomson Scattering profiles, which were fitted by a mtanh [2]. In first approximation, a separatrix temperature of $T_{e,sep}$ = 100 eV has been assumed, however since $T_{e,sep}$ can vary up to 30 eV according to [3], a more precise analysis has been carried out, using a 2-point model to determine the position of the separatrix [4].

Attaining efficient core particle fuelling will be one of the key tasks in a future fusion reactor. A high fuel confinement time, as well as a high burnup-fraction is required, in order to keep the required tritium inventory as low as possible. In addition, high energy confinement has to be maintained to ensure self-sustained burn. To compare the fuelling performance of gas-puffing and pellets, a dedicated series of experiments was carried out, in which the total Deuterium fuelling particle flux Γ_{tot} was kept approximately constant by stepwise replacing the initial gas flux by pellets. Keeping a fixed pellet mass, the pellet contribution was raised by increasing the injection rate, with a maximum of 85 % flux share. The experiments were carried out during the recommissioning phase of the revised pellet system, thus a very robust low shaping, high q_{95} = 5.2 plasma scenario at I_p = 0.8 MA had to be chosen.

Increasing the pellet flux forced a core density raise while the edge density remained virtually unaffected, confirming that the recycling of plasma particles only depends on the total particle throughput but not on the specific kind of refuelling. Pellet actuation raised the core density up to three times the Greenwald density n_{Gw}, while also maintaining an approximately constant kinetic energy confinement, corresponding to an initially moderate level of H06 $\approx$ 0.87. As – progressing into the high core density regime - a dramatic drop in the fast particles takes place, this actually implied a gain in thermal energy content of approximately 10-20 %, due to an increasing core pressure and an approach to $T_e = T_i$. The strong peaking of the density profile was accompanied by a significant increase of the total plasma particle content N_p. Since Γ_{tot} = const. was pre-set, this is equivalent to an enhanced particle confinement time $\tau_{p,tech}$ = N_p/Γ_{tot}; substantiating the improved fuelling capacity of pellets with respect to gas. Moreover, a supra linear response of the core density with increasing pellet flux was observed. The trivial effect of the deeper penetration - as a higher pellet flux causes a more intensified plasma cooling - would underestimate this non-linear increase in $\tau_{p,tech}$. The observations are in agreement, however, with the effects of an increased collisionality on turbulent particle confinement predicted in ref. [5].

Zusammenfassung

Die Voranalyse zur Thematik bezog sich auf eine Datenbank, welche Entladungen des Hochdichteregimes des Tokamaks ASDEX Upgrade (Wolfram Wandung) beinhaltet. Die große Mehrheit der Entladungen wurde außerdem unter Verwendung von Pellets als Nachfüllmethode durchgeführt und erstreckt sich über einen Zeitraum von acht Jahren. In Hinblick auf Leistung, beinhaltet die Datenbasis Szenarien, bei welchen auf das Abzielen hoher Leistungen geachtet wurde (z.B. Stickstoff-Seeding oder ITER Baseline Szenarien), aber auch Entladungen mit mäßiger Leistung.

Analaysen [1] haben gezeigt, dass beim Überschreiten der Greenwalddichte n_{Gw} die zusätzliche Leistungsverbesserung bei den oben genannten Methoden verloren geht. Es wurde vermutet, dass dies von einer steigenden Separatrixdichte $n_{,esep}$ herrührt. Durchgeführte Analysen lassen diese Vermutung nun noch wahrscheinlicher erscheinen. Um dies weiter zu ergünden, wird zunächst eine Methodik benötigt, die Separatrixdichte (Randdichte) zu kontrollieren. Neben dieser Analyse, wurde auch die Abhängigkeit der Separatrixdichte von der Divertor- Neutralgasdichte n_0^{Div} untersucht.

Die Position der Separatrixdichte kann zwar dadurch abgeschätzt werden, dass für H-Moden eine Separatrixtemperatur von $T_{e,sep}$ = 100 eV angenommen wird, was jedoch bis zu 30 eV variieren kann [3]. Daher wurde ein 2-Punkt Wärmeleitungsmodell genutzt [4], um die Separatrixposition präziser zu bestimmen.

In einem zukünfigten Fusionsreaktor wird es von großer Wichtigkeit sein, ein effiziente Plasmanachfüllung und einen hohen Anteil an Abbrand zu erzielen, um die Anforderung an Tritium, so gering wie möglich zu halten. Daher beschäftigte sich der Hauptteil dieser These mit dem Vergleich zwischen Gas- und Pelletnachfüllung. Hierzu wurde eine Reihe von Experimenten durchgeführt, bei welchen der Gesamtteilchenfluss Γ_{tot} annäherungsweise konstant gehalten wurde. Dabei wurde so vorgangen, dass jede Entladung ausschließlich mit Gasfluss gestartet wurde, welcher dann schrittweise durch Pelletfluss ersetzt worden ist. In dieser Experimentreihe wurde unter Maximalfrequenz der Pelletzentrifuge ein Pelletflussanteil von circa 85 % erre-

icht.

Die Experimente wurden im Rahmen der Wiederinbetriebnahme von ASDEX Upgrade durchgeführt und hatten mit dem Test des verbesserten Pelletsystems einen technischen Fokus. Folglich wurde ein robustes Plasmaszenario mit q_{95} = 5,2 und I_p = 0,8 MA gewählt. Eine Erhöhung des Pelletflusses sorgte für ein Ansteigen der Zentraldichte, währrend die Randdichte nahezu konstant gehalten werden konnte. Dadurch wurde die Vermutung bestätigt, dass das Recyceln der Plasmapartikel lediglich vom Gesamtteilchenfluss abhängt und nicht von der jeweiligen Nachfüllart. Durch die Verwendung von Pellets, konnte zudem die Zentraldichte auf die dreifache Greenwalddichte angehoben werden, während das Energieconfinement annäherungsweise konstant blieb (H06 $\approx$ 0,87). Der Übergang in das Hochdichtegregime ging mit einem starken Rückgang schneller Teilchen einher. Dies bedeutet, dass ein Anstieg des thermischen Energieinhaltes vorliegen muss, welcher mit ungefährt 10-20 % abgeschätzt werden konnte und durch einen Anstieg des Zentraldrucks und $T_e = T_i$, verursacht wurde. Das Zuspitzen der Dichteprofile durch die Pelletinjektion, wurde von einem Anstieg im Teilcheninventar N_p begleitet. Da der Gesamtteilchenfluss Γ_{tot} konstant gehalten wurde, ist dies equivalent zu einem Anstieg der Teilcheneinschlusszeit $\tau_{p,tech}$ = N_p/Γ_{tot}. Der Anstieg der Zentraldichte folgte einem nicht-linearen aufsteigendem Trend. Unter Betrachtung des tieferen Eindringens von Pellets, durch das Abkühlen des Plasmas wurde der Trend unterschätzt. Erst unter Berücksichtigung von turublentem Teilcheneinschluss, dominiert von Kollisionalität [5], konnte der experimentelle Trend modelliert werden.

Acknowledgement

It is my pleasure to acknowledge the roles of several individuals who were instrumental for completing this Bachelor thesis.

First and foremost, I would like to pay my special regards to Prof. Martin Prechtl, who not only supervised this thesis in an extremely supportive manner, but also established the initial contact between myself and the IPP. On the behalf of myself and every student who, thanks to Prof. Prechtl, had the pleasure of working on a project at the IPP, I want to express my gratitude.
I would like to express my deepest gratitude to Dr. Peter Lang, who provided me with valuable input on a daily basis and also encouraged me regularly. Thereby, he had the lion's share in terms of my personal growth within the last year. Him and Dr. Otto Kardaun were my internal supervisors at the IPP and constantly provided me with guidance and new innovative ideas.
I would also like to thank Prof. Karl Lackner, who brought up the intial idea for the experiments, which have been carried out for this thesis. In long meetings, he also broadened my knowledge in the field of fusion research remarkably. Regarding the analysis of the experiments, Dr. Clemente Angioni was an integral part, who was always eager to help resolving modelling issues.
This work would not materialize, without the trust and guidance of Prof. Arne Kallenbach. He not only approved the experiments, but also provided me with invaluable advise prior to the experiments.
These acknowledgements would not be complete without paying my special regards to Dr. Rainer Fischer, who conducted additional analyses which made plenty of my own analyses possible in the first place. Furthermore, I am indebted to my fellow student Jakob Elsner, who turned a weekly visit at the IPP, into an analysis algorithm. Without that, the benevolence of my results would have been inconceivable.
My deepest appreciation belongs to my family for their patience and emotional support.

Abbreviations

ASDEX	Axially Symmetric Divertor Experiment
AUG	ASDEX Upgrade
CXRS	Charge Exchange Recombination Spectroscopy
D	Deuterium
DEMO	DEMOnstration Power Plant
DCN	Deuterium cyanide
ECRH	Electron Cylclotron Resonance Heating
GIZ	Grazing Incidence
HS	High Shaping
ICRH	Ion Cyclotron Resonance Heating
IDA	Integrated Data Analysis
IPP	Max Planck Insitute for Plasma Physics
ITER	International Thermonuclear Experimental Reactor
ITER BL	ITER Baseline
JET	Joint European Torus
LCFS	Last Closed Flux Surface
MHD	Magnetohydrodynamics
NBI	Neutral Beam Injection
N-Seeding	Nitrogen Seeding
Nd-YAG	Neodymium-doped Yttrium Aluminum Garnet
OLS	Ordinary Least Squares
PFC	Plasma facing components

Ref	Reference (discharges)
RMP	Resonant magnetic pertubations
SOL	Scrape off layer
Tokamak	Toroidal Chamber with Magnetic coils
T	Tritium
TS	Thomson Scattering
vav	Volume-averaged

Contents

1 Introduction

This Chapter provides an overview about the importance of nuclear fusion as a future source of energy. Moreover, an outline of the topic of the thesis is also contained.

1.1 General Introduction

Providing energy to human mankind has been a very controversial topic and is of current relevance for politics. A dream scenario would involve a method, which is powerful enough to supply billions of people, while simultaneously being environmentally compatible, especially in terms of CO_2 emission. While fission is a suitable candidate to fit these conditions, it still involves problems like final disposal, as well as safety aspects.

Furthermore, when considering the growth of global population, a tremendous rising trend within the subsequent years is expected. A possible extrapolation of this trend is depicted in figure 1.

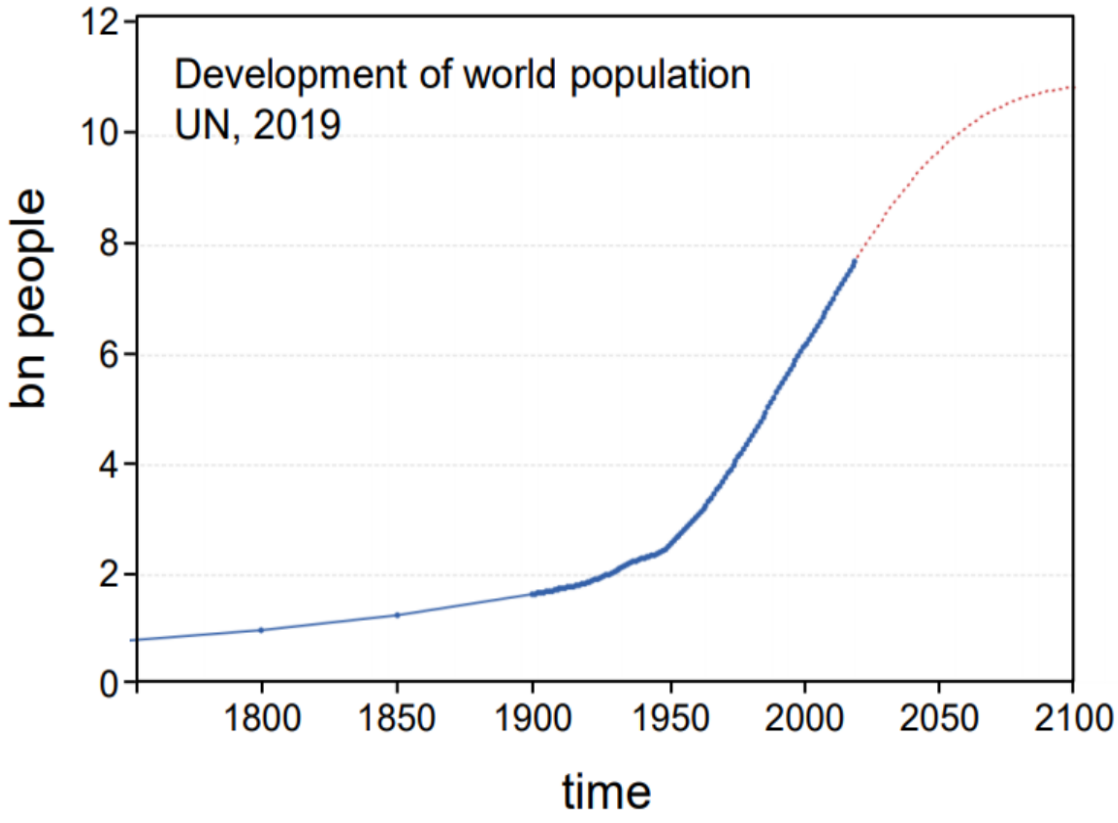

Figure 1: Extrapolation of the growth of human mankind [6]

It should also be noted, that there is a supra-linear dependency between energy consumption and population growth. This can be attributed to the fact, that a rising population is correlated with further industrial development and thereby also a rise in living standards, which require more energy [7].

Figure 2 depicts the non-linear increase in energy consumption of previous decades.

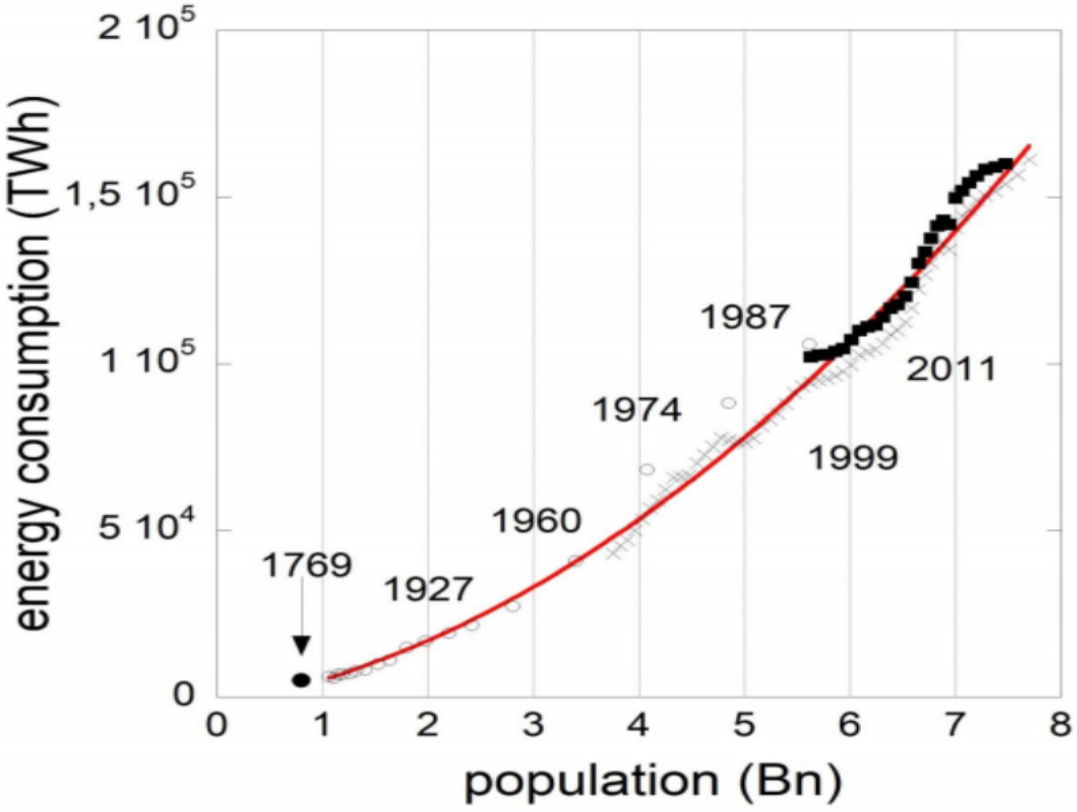

Figure 2: Energy consumption depending on global population [6]

As illustrated in figure 2, the energy consumption increased approximately quadratically as a function of the population. This intensifies the problem of future energy supply even more.

Due to the problems of fission, nuclear fusion has to be considered. If implemented successfully, it would provide similar advantages as fission, while also getting rid of final disposal and long half-lives of the educts. Chapter 3 will provide further details, on how fusion on earth could be achieved. When considering possible fusion reactions, the only reactant with a considerable half-life is tritium, the heaviest and most rare isotope of hydrogen, with a half-life of roughly 12.3 years [8]. Typical half-lives

of fission products, however, are typically around the order of 60,000 years, or even more [9].

Another aspect, which should be discussed are the resources (materials), which will be needed for nuclear fusion on earth to be conducted. As for that, the most suitable fusion reaction is introduced. The reasons for other fusion reactions to not be suitable for nuclear fusion on earth, will be discussed in chapter 3.

$$D_1^2 + T_1^3 \longrightarrow He_2^4 + n_0^1 + 17.6\,\text{MeV}$$

Here, D and T refer to the isotopes of hydrogen, deuterium and tritium. The educts of the reaction are helium, as well as a neutron. The isotope deuterium occurs as one part out of 6400 (156 ppm) in naturally occurring hydrogen [10] and is therefore easier accessible compared to tritium, which only takes up 10^{-15} % of natural hydrogen [11]. Hence, after a couple years of operation, the vast majority of natural tritium resources would be exhausted [12]. However, tritium can be bred in a so called breeding blankets, which will be installed in future reactors. There, neutrons produced as described by the equation above are used to breed Tritium out of either ^{6}Li or ^{7}Li [13].

$$n + {}^6\text{Li} \longrightarrow {}^4\text{He} + T + 4.8\,\text{MeV}$$

$$n + {}^7\text{Li} \longrightarrow {}^4\text{He} + T + n - 2.5\,\text{MeV}$$

While the first reaction with ^{6}Li allocates extra energy, an extra neutron is provided by the second reaction, which can be used to create another tritium atom, by using the reaction with ^{6}Li involved. It also has to be taken into account, that naturally occurring Lithium consists of 7.5 % ^{6}Li and 92.5 % ^{7}Li [13].

Since there is no doubt, that fusion will be a key factor for solving future energetic problems, its research has to be on point, in order to achieve a reactor capable concept. While the tokamak JET has shown the best results so far, the next big step called ITER, is currently under construction and is expected to firstly operate in 2025 [14]. If ITER achieves its goals (chapter 3), the construction of DEMO, a demonstration reactor, will be started immediately [15].

Lastly, aspects of safety have to be taken into consideration. In terms of radioactive contamination, only Tritium and material, activated by neutrons are possible dangers.

As mentioned above, Tritium has a half-life of 12.3 years. If Tritium is absorbed by the human body, 97 % of the Tritium only has a half-life of approximately ten days. The remaining three per cent have a half-life of up to one year. Therefore, the mean biological mean half-time of Tritium is 11 days, but can vary up to 40 days [16]. Core meltdowns, analogous to fission, are also not a potential danger in the context of nuclear fusion, since it is difficult enough, to reach and maintain the necessary conditions for nuclear fusion in the first place [17]. In case of a severe technical problem, the plasma would immediately cool down and the reactions would stop [17].

1.2 Introduction to the topic

While the main topic of this thesis covers a new series of experiments, where the total particle-influx Γ_{tot} has been keept approximately constant, by exchanging gas-puff by pellets, the whole topic started off with analyses of the high confinement, pellet fuelled database of ASDEX Upgrade (AUG). The database comprises scenarios with moderate performance (technical discharges), as well as attempts to achieve high performance by applying either N-Seeding or high shaping (HS). The database currently contains a total of 54 different discharges (2011-2019) and 667 datapoints. The data has been used, to compare two scalings for energy confinement. The concepts of energy confinement and empirical scaling laws will be further discussed in chapters 3 and 4. A primary incentive for this thesis was the fact, that in both confinement scalings, a loss in extra confinement (due to confinement enhancing methods), when exceeding the Greenwald density n_{Gw} was exceeded, could be perceived.

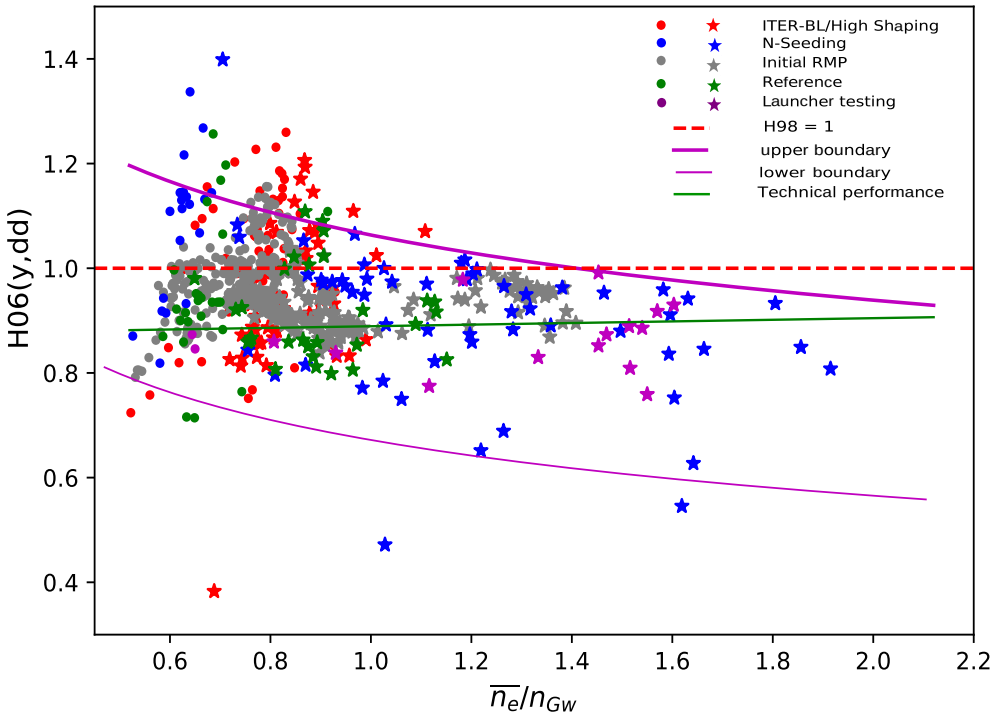

Figure 3: Confinement scaling H06(y,dd) as a function of the normalized electron density $\overline{n_e}/n_{Gw}$. At $\overline{n_e}/n_{Gw} \approx 1$, a degradation of extra confinement can be seen, since neither N-Seeding (blue) or high shaping/ITER BL (red) datapoints exceed H06(y,dd) = 1.

As shown in figure 3, beyond $\overline{n_e}/n_{Gw} \approx 1$, no datapoints of confinement enhanced methods (red and blue stars) indicate any extra confinement.

A possible candidate to explain this degradation was assumed to be a rising separatrix density $n_{e,sep}$ [2]. This thesis therefore also focused on determining $n_{e,sep}$, which is not simply obtainable by accessing global data, but requires additional profile analysis.

A pivotal topic which arised from analysing this feature, was to find a way to control the separatrix density $n_{e,sep}$. Therefore, experiments have been carried out to show that the edge density (separatrix density) only depends on the total particle-influx, but not on the kind of refuelling. Besides this observation, this series of experiments also provided several other findings, e.g. peaking of the core pressure profile, shifts in plasma energy, a non-linear increase in core density and new plasma physical parameters, which describe the change in transport, induced by the change in particle

sources. Analysis has shown that pellet usage will be essential for running a future reactor as efficient as possible.

2 Content of the thesis

Chapter 3 contains a theoretical introduction into fusion-oriented plasma physics and fusion research, as well as diagnostics and other technical aspects of ASDEX Upgrade. The main purpose of this section is to facilitate the comprehension of the following chapters.

Chapter 4 firstly introduces and compares the two energy confinement time saclings H98(y,2) and H06(y,dd)) and provides an overview, why one of them is significantly more suitable, for describing data in the high density regime. Furthermore, it is described how the separatrix density can be determined, as well as its correlation with the divertor neutral gas density n_0^{Div}. Moreover, the measurement and calibration of n_0^{Div} will be discussed. Lastly, the impact of the separatrix density $n_{e,sep}$ on energy confinement is observed.

Chapter 5 firstly provides an overview, on the series of gas-pellet exchange experiments, which have been carried out and which technical boundaries were given. Secondly, several experimental results are presented. Modeling and explanatory approaches for the respective results will be given. In this chapter, particle confinement times, as well as diffusion coefficients will be defined and discussed.

Chapter 6 gives a summary, as well as an outlook, in both English and German, to each respective chapter. Furthermore, future experimental set-ups are suggested.

The Appendix will provide an overview, over the different statistical tools and analyses (e.g. numeric volume integrals), which have been used for this thesis. Furthermore, additional information and figures, to provide further context on specific topics, are contained.

3 Theoretical Concepts

In this chapter, an introduction into fusion oriented plasma physics and fusion research is given. Furthermore, more specific concepts, which are relevant to comprehent the following chapters are also discussed.

3.1 Plasma and methods of confinement

Despite the vast majority of the known universe being in the plasma states, it is rather unfamiliar for most people. Plasma can be defined as ionized gas, which means, that most of its components are free electrons and ions [18]. As a consequence, plasma can be impacted by magnetic fields. A very important parameter when it comes to describing plasma, is the particle density n, given in particles per unit volume. With the introduction of the particle density, the equation of ideal gas reads as:

$$p = n \cdot k_B \cdot T \tag{1}$$

where k_B is the Boltzmann constant.

When it comes to the parameters density and temperature, plasma cover a wide margin. The sun surface for instance, radiates at a temperature of approximately $T_{sun,surf.}$ = 5700 K. Its core, however, has a temperature of roughly 17 million degrees [18].

Since relatively high temperatures (by human standard) are not a rarity when it comes to describing plasma, temperatures are usually given in electron volts (eV) with 1 eV being equivalent to $\approx$ 11605.4 K [18].

Now the question remains, whether the equation of ideal gas is appropriate when it comes to describing (fusion-) plasma. For a more precise description, the Van-der-Waals equation might be necessary:

$$\left(p + \frac{a}{{V_m}^2}\right)(V_m - b) = RT \tag{2}$$

where V_m is the molar volume, parameter b the volume occupied by one mol and a, a parameter which describes the attraction of the particles. As described in reference [19], a classical plasma can occupy solid, liquid and non-ideal gas phases. For this thesis, however, the description of an ideal gas is appropriate.

3.2 Characterization of plasma

As outlined above, temperature T and the particle density n are the most pivotal plasma physical parameters when it comes to characterizing plasma. Therefore, plasma regimes are usually depicted in a T-n phase diagram, as illustrated in figure 4:

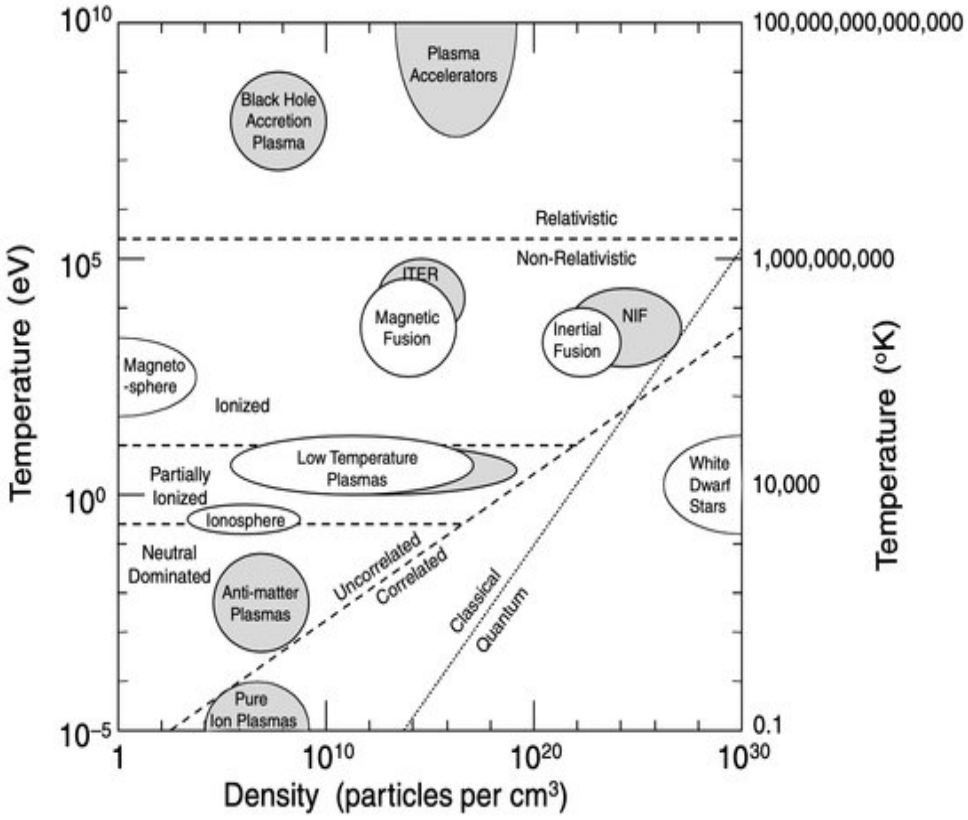

Figure 4: Plasma regime characterization in a temperature-density-diagram [20]

Figure 4 includes the boundaries between different plasma regimes. The plasma state heavily depends on the thermal energy of the plasma. A plasma is for instance declared as relativistic, if the mean thermal energy is equal to the resting energy of the electron [18]:

$$\frac{3}{2}k_B T = m_{0,e}c^2 \tag{3}$$

The most likely plasma to occur in nature is ideal classical plasma. An ideal plasma is given, if the mean thermal energy exceeds the electrostatic interaction [18]. The electrostatic interaction for hydrogen can be expressed by $E_e = \left(e^2 \cdot n^{1/3}\right)/(4\pi\epsilon_0)$. Therefore, the balance for an ideal plasma reads:

$$\frac{3}{2}k_B T = \frac{e^2 \cdot n^{1/3}}{4\pi\epsilon_0} \tag{4}$$

Considering the the balance in equation 4, this would numerically mean, that a temperature of $T \approx 10^{-9} n^{1/3}$ is needed for a plasma to be ideal.

Typical fusion plasma is expected to have a temperature of around $\approx 10^8$ K and particle densities of more than $10^{20}\, m^{-3}$, which would mean that it is partially relativistic plasma [18]. Therefore, hot fusion plasma cannot be described by a Maxwell-Boltzmann distribution anymore, but by a Maxwell-Jüttner distribution. While the Maxwell-Jüttner distribution also assumes the particles to be dilute and to not interact with each other, the main difference to a Maxwell-Boltzmann distribution is, that effects of special relativity are taken into account [21].

The respective probability density distribution for $\gamma = 1/\sqrt{1 - v^2/c^2}$ is then given by:

$$f(\gamma) = \frac{\gamma^2 \beta}{\theta K_2(1/\theta)} \exp\left(-\frac{\gamma}{\theta}\right) \tag{5}$$

Where $\beta = \sqrt{1 - 1/\gamma^2}$, $\theta = \frac{kT}{mc^2}$ and K_2 is the modiefied Bessel function of 2nd kind [22].

An ubiquitous relativistic effect in fusion plasma are so called runaway electrons. Since a tremendous current has to be carried by plasma particles, the magnetic energy is significantly exceeding the thermal energy of the particles, carrying the current. Therefore, the electrons recession velocity is usually smaller than their thermal velocity [23]. Nevertheless, there might be a fraction of faster particles and there is a chance, these particles are the main carrier of the current.

At a given velocity, the friction force in plasma decreases with rising velocity. Thereby, these particles can accelerate unlimitedly. These fast electrons often tend to excite waves within plasma which might lead to instabilities [23].

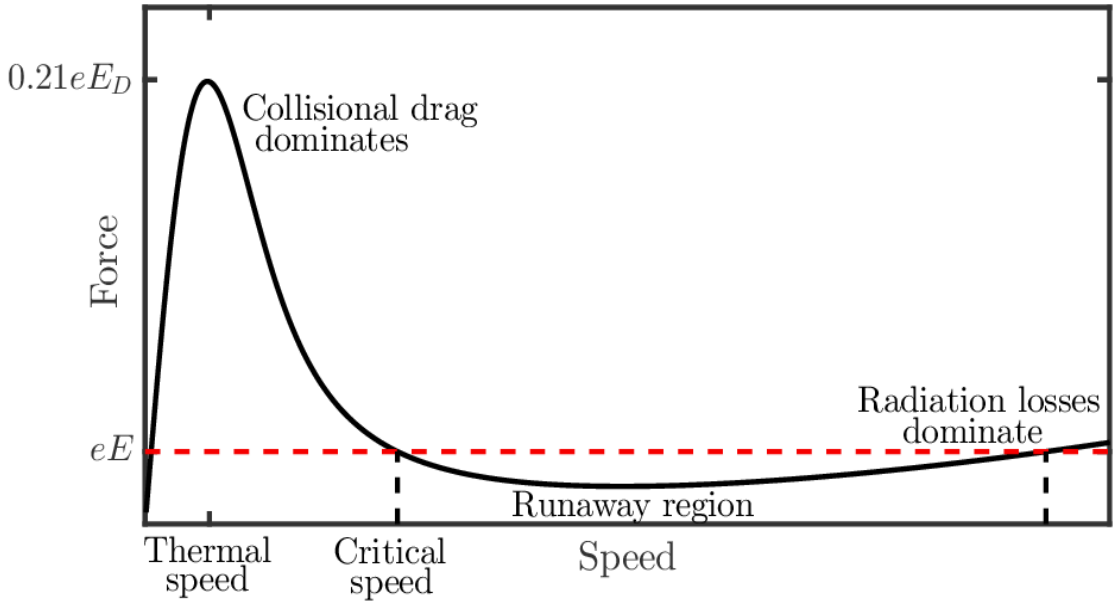

Figure 5: Friction force in plasma as a function of the particle speed [24]

Figure 5 depicts the friction force within a plasma, as a function of the momentum of particles. If relativistic effects carry in, for instance due to particles, within the tail of a Maxwell-Boltzmann distribution and the momentum $p_{crit} = m \cdot v_{crit}$ is exceeded, they count as runaways.

3.3 ASDEX Upgrade

ASDEX Upgrade (AUG) is a tokamak experiment which started its operation in 1991. Ever since, AUG conducted roughly 37,000 discharges. AUG aims to observe to observe plasma parameters such as particle density or temperature, as well as the edge physics for future machines like ITER [25] or even future fusion devices like DEMO [26]. ASDEX Upgrade unique characteristic are full metal (tungsten) plasma facing components (PFCs). Future machines will most likely have Beryllium as PFCs. Tungsten has a melting temperature of $\approx$ 3695 K and is thereby a suitable candidate for PFCs.

ASDEX Upgrade can provide a total of 27 MW of heating power. The respective

heating methos are further explained in chapter 3.7. With a small plasma radius of a $\approx$ 0.5 m and a major plasma radius of R $\approx$ 1.6 m, AUG is regarded as a medium sized tokamak [27]. Roughly more than a temperature of T $\approx 10^8\ K$ can be achieved. In terms of spatial geometry, AUG resembels a torus:

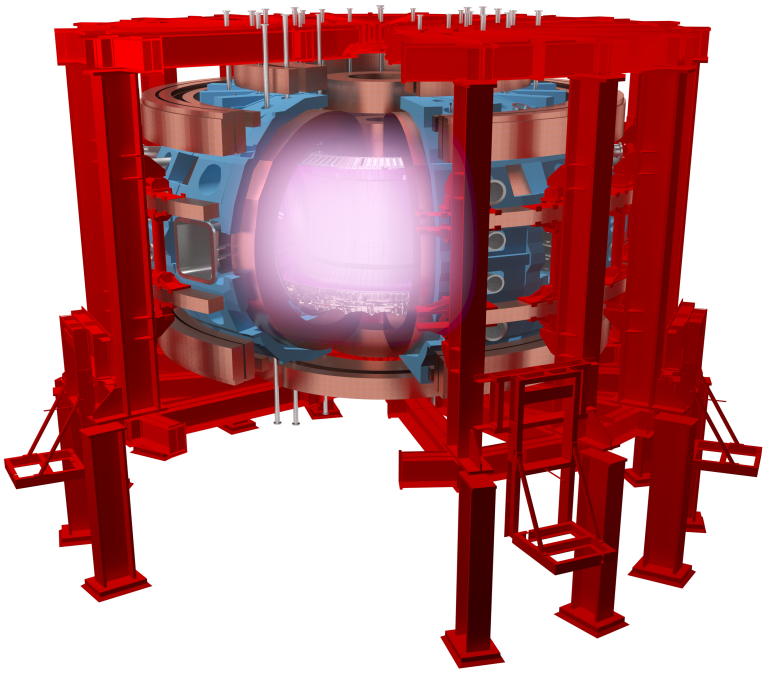

Figure 6: 3 D model of ASDEX Upgrade, containing Plasma, divertor, plasma vessel and several supporting structures [28]

As illustrated in Figure 6, AUG has two kinds of magnetic field coils. While the outer (poloidal) field coils provide an outer magnetic field, the inner (toroidal) field coils serve as primary coil of a transformer, which induces a current into the plasma. The plasma itself, serves as the secondary coil of the transformer. The fact that the plasma carries its own current, is the main difference to the second method of confinement the Stellarator [29].

Ás a comparison, ITER will have a major radius of R = 6.2 m [30] which will lead to a tremendous increase in expenses compared to AUG.

Besides the geometrical paramters, the cross-section of AUG should also be considered and is thereby given in figure 7

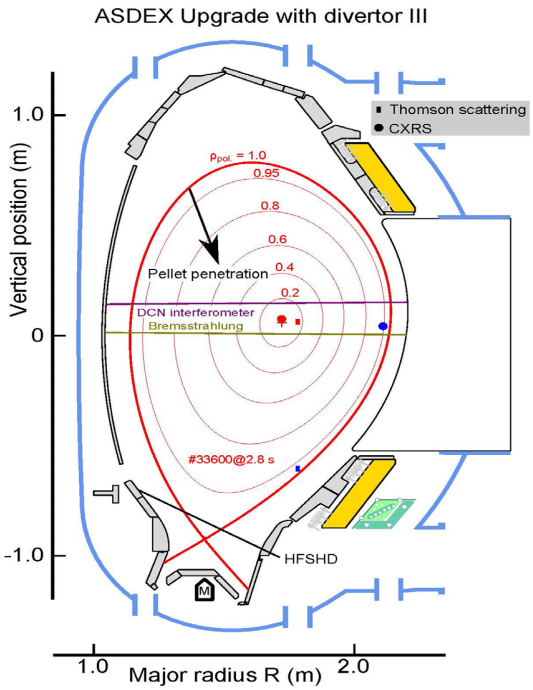

Figure 7: Cross-section of AUG, containing magnetic flux surfaces, the Divertor and some key diagnostics [2]

Figure 7 also contains the closed magnetic flux surfaces, which, at one point (ρ_{pol} = 1) split up and end in the so called Divertor [31, 32]. A Divertor is a magnetical concept, which ensures that plasma does not disrupt due to impurities, e.g. ablated tungsten particles of the plasma wall. The Divertor has a certain potential which solely attracts particles whose charge number is greater than one. Hence, the plasma particles are not being attracted to the Divertor, while high-Z impurities (like tungsten) get partially removed from the plasma. Since the arriving particles damage the Divertor, it has to get replaced after approximately two years of reactor operation. ASDEX Upgrade currently has Divertor III installed, which is equipped with an in vessel gyro pump [33].

3.4 Nuclear Fusion on Earth

With the sun as prototype, fusion has been regarded a potential soucre of energy ever since Einstein discovered the equivalency of mass and energy [13]. There is not doubt, that only one fusion reaction is suitable for fusion on earth, which is the reaction of deuterium and tritium to helium and a neutron.

$$D_1^2 + T_1^3 \longrightarrow He_2^4 + n_0^1 + 17.6\,MeV$$

The sun, however, uses the most efficient reaction, in which four protons are fused to helium. Within this reaction, 7.07 MeV per nucleon is released, since the helium nuclear has a very high binding energy (full outermost shell) [13]. Why this reaction is not a possible candidate for fusion on earth, will be explained below.

In general, energy will be released, if two elements, lighter than iron are fusing. This can be attributed to the fact, that the binding energy has its maximum at iron.

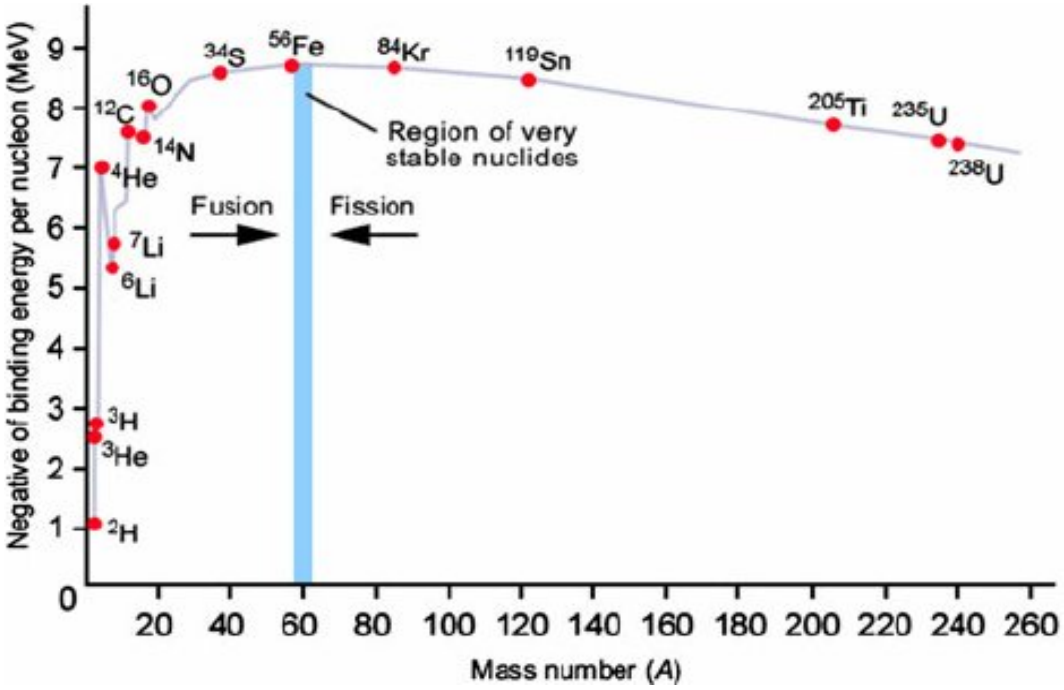

Figure 8: Averaged binding energy as a function of the mass number [34]

Figure 8 shows the averaged binding energy as a function of the mass number.

While beyond the nucleon number of ≈ 60, the binding energy decreases due to Coulomb repulsion of the large amount of protons, the binding energy decreases left from iron as the surface to volume ratio of the nucleus increases. Since the strong force only interacts on its nearest neighbors, a large surface to volume ratio would mean that there are less neighbors and therefore less contribution to the binding force. However, the rise in binding energy when approaching helium cannot be explained by this so called liquid-drop model. Instead, it can be attributed to special configurations

of proton and neutron numbers which lead to a more stable nucleus, similar to noble gases [18].

While up to approximately one Fermi ($10^{-15}\ m$), the repulsive Coulomb force is dominant, for smaller radii, the strong force prevails. In order for two nuclei to fuse, energies around the order of 500 keV would be required when considering the fusion progress in a classical way [18].

However, by taking quantum mechanics into account, the process of overcoming this energy barrier can take place, despite the energies being insufficient. This can be attributed to the effect of tunneling. With that being said, there is always, for temperatures greater than zero, a finite probability for a nuclei to approach closer to the Coulomb barrier and eventually to tunnel through. This process is being illustrated in figure 9

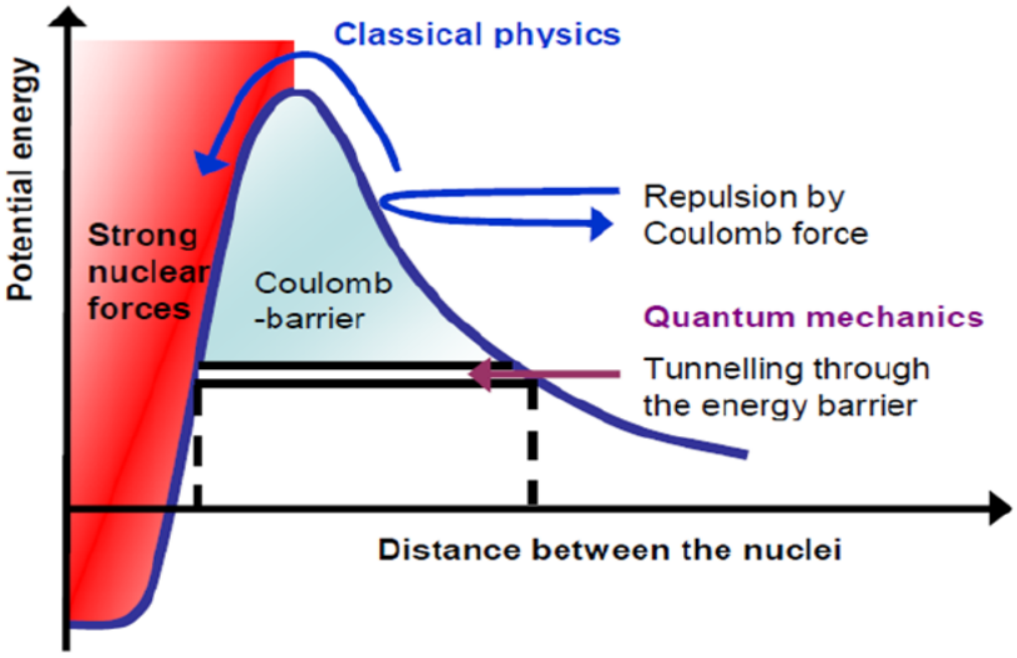

Figure 9: Potential energy decreasing with $\approx 1/r$ with rising distance between nuclei [35]

The probability dependencies of nuclei tunneling through the Coloumb barrier is given by:

$$p_{tunnel} \propto exp(-\frac{2\pi Z_1 Z_2 e^2}{\hbar v}) \tag{6}$$

with Z_1 and Z_2 being the charge numbers of the nuclei and v their relative velocity. Considering equation 6, another reason becomes evident, why nuclei with a charge number greater than one would not be suitable for fusion reactions since the probability of tunneling would decrease exponentially.

3.4.1 The sun as model for fusion

While fusion is the main source of all stars, it has been there, since any and all elements with a number of nucleons smaller than 60, have been created by Fusion [18]. The main reactions in the sun are:

$$\mathrm{p} + \mathrm{p} \longrightarrow \mathrm{D} + \mathrm{e}^{+} + \nu_e$$

$$\mathrm{D} + \mathrm{p} \longrightarrow {}^{3}\mathrm{He} + \gamma$$

$${}^{3}\mathrm{He} + {}^{3}\mathrm{He} \longrightarrow {}^{4}\mathrm{He} + 2\,\mathrm{p}$$

Here, p stands for a proton, e^+ denotes a positron, γ_e an electron neutrino and ν_e a high energy photon. ${}^3He$ and ${}^4He$ are the respective isotopes of Helium. While there are other reaction chains, this is the most important one, since it produces $85\ \%$ of the total energy. As further explained in [18], the weak interaction is involved in this reaction chain, which leads to the emission of neutrinos. Since all reactions, involving weak interaction have a relatively low cross-section and thereby a low reaction rate, this makes this kind of reaction chain not suitable for fusion on earth. To observe fusion processes in stars externally, neutrinos are studied. This can be attributed to the fact that solely the neutrinos leave the sun, since they are neither affected by electromagnetical-, nor by strong interaction.

3.4.2 Choice of the D-T reaction for Fusion on earth

While stars can compensate the low reaction rates, caused by weak interaction, with their tremendous volume, one earth, reactions involving weak interaction cannot be achieved.

Besides the D-T reaction, there would be other candidates to fulfill this role, e.g. D-D reactions and D-^3He reactions. The D-D reaction would only require deuterium as reactants, which is significantly less rare than tritium. However, the D-T reaction has still, even at low energies, the highest cross-section, as shown in figure 10

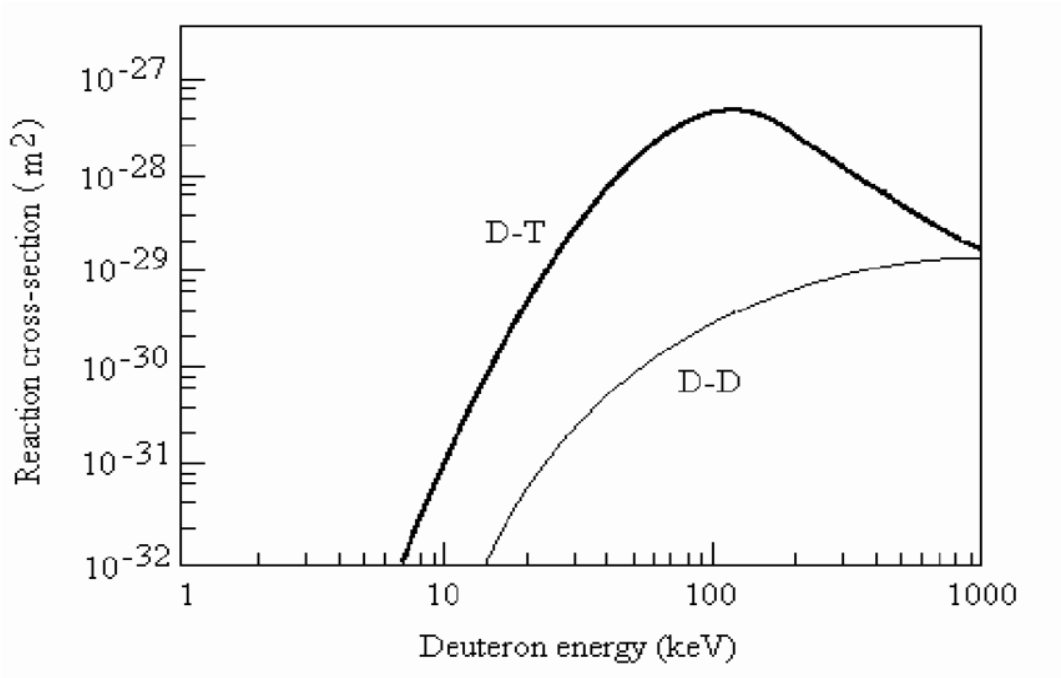

Figure 10: Crossection comparision of the D-T and the D-D reaction as function of Deuteron energy [36]

Lastly it has to be mentioned that the released energy of $\approx$ 17.6 MeV of the D-T reaction comes from mass defect [37] and can therefore be calculated by:

$$\Delta E_{D-T} = \delta m \cdot c^2 = 2.818 \cdot 10^{-12} joules = 17.59 MeV \tag{7}$$

3.5 Plasma ignition

Since an outline on fusion reactions and fusion concepts has been presented above, the efficiency and feasibility of nuclear fusion should now be discussed.

As further elaborated in [18], a criterion for a positive power balance has been firstly described by John D. Lawson. As shown in equation 7, 17.59 MeV are produced by a single D-T reaction. While the majority of energy is carried by the neutrons, approximately 3.5 MeV are carried by helium, the so called $\alpha-$ particles. Since the

neutrons cannot be magnetically confined, they leave the plasma and their energy is further transformed, similar to ordinary reactor concepts [38]. The $\alpha-$ particles however, can be confined within the plasma. Moreover, the $\alpha-$ particles slow down due to collisions and are thereby releasing the energy to the plasma, which leads to a heating of the plasma.

In newer criteria for a positive power balance, the energy of the $\alpha-$ particles has to compensate any and all energy losses. The power loss in a fusion the device can be considered as the sum of the inner plasma power P_{inner} and the bremsstrahlung $P_{bremsstrahlung}$. The two losses can be calculated, using:

$$P_{inner} = \frac{W_{inner}}{\tau_e} = \frac{3 n_e k_B T}{\tau_e} \tag{8}$$

$$P_{bremsstrahlung} = c_1 n_e^2 Z_{eff} (k_B T)^{1/2} \tag{9}$$

It should be noted, that the numerator in equation 8 is twice the equation of ideal gas, since every hydrogen atom splits into electron and nucleus. The energy confinement time τ_e describes several transport processes like convection, diffusion and charge exchange. In equation 9, c_1 is the bremsstrahlung constant and Z_{eff} is the effective charge of the plasma, which is a measure for impurities in the plasma. Since $P_{bremsstrahlung} \propto Z_{eff}$, too high impurity concentrations can lead to plasma disruption, since a crucial amount of plasma energy is radiated.

The sum of equations 8 and 9 has to be compensated by the fusion power, in order to reach plasma ignition. The fusion power can be obtained, multiplying the reaction rate by the energy of the $\alpha-$ particles E_α.

$$P_{fus} = \left(\frac{n}{2}\right)^2 \langle \sigma v \rangle E_\alpha \tag{10}$$

With $\langle \sigma v \rangle$ being averaged product of the relative velocity of the reacting particles and their cross-section. With those equations, the power balance now reads:

$$\left(\frac{n_e}{2}\right)^2 \langle \sigma v \rangle E_\alpha = \frac{3 n_e k_B T}{\tau_e} + c_1 n_e^2 Z_{eff} (k_B T)^{1/2} \tag{11}$$

Applying algebra, equation 11 can be converted to $n\tau T$, which is the so called **fusion triple product** and is solely a function of temperature, which has its minimum at 35 $\cdot 10^{35} keVs/m^3$, at a temperature of approximately 10 keV, as illustrated in Figure 11

$$n\tau_e T = \frac{12 k_B T^2}{\langle \sigma v \rangle E_\alpha - 4 c_1 Z_{eff} (k_B T)^{1/2}} \tag{12}$$

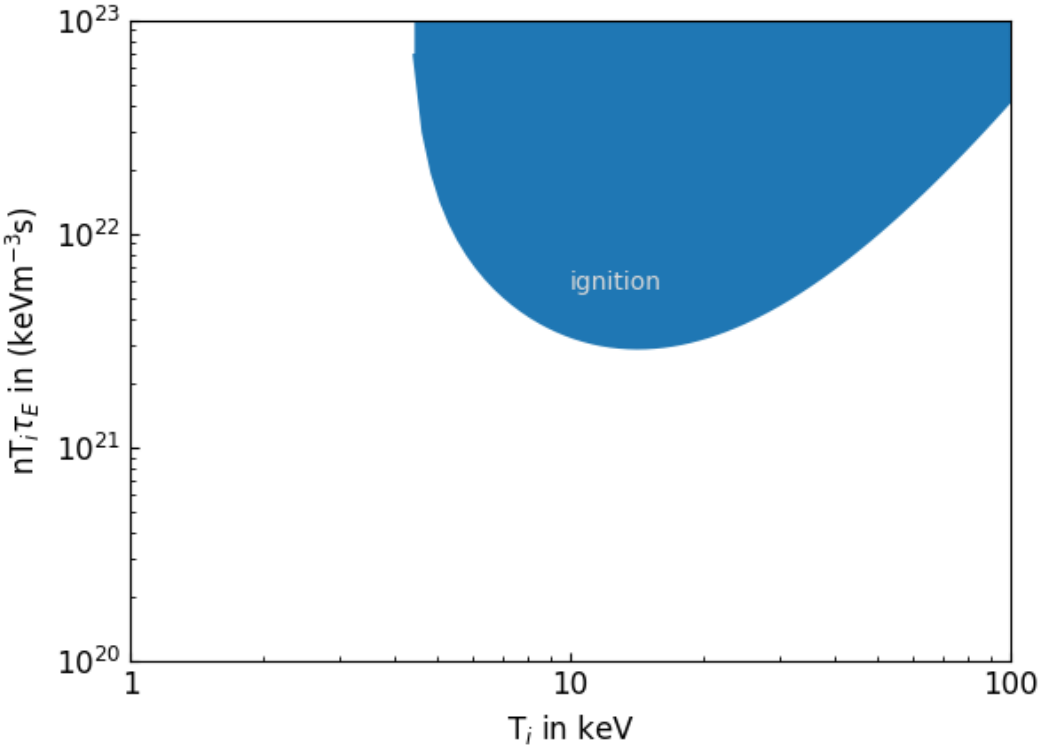

Figure 11: fusion triple product as function of temperature [39]

By considering equation 12, it becomes evident, that temperature of approximately 10 keV have to be achieved, while simultaneously achieving high densities and a high energy confinement time.

While the best devices in the mid-sixties fell short about five orders of magnitude to reach ignition, today's best experiments only fall short by a factor of seven. However, solely reaching ignition will, in the long run, not be enough, since very long spans of continuous energy production will be needed, until a marketable fusion reactor can be built.

The next step for achieving this goal will be ITER, a worldwide collaboration of Eruope, Russia, Japan and the US. ITER is expected to have pulse lenghts of up to 400 seconds. Moreover, the energy production which is expected to be roughly ten times higher than the energy needed, to induce and heat the plasma [18]. However, ITER will not be a reactor concept. In that regard, DEMO will be the next project which would go under construction, if ITER is able to achieve the expected goals. In order for DEMO to be built, both, the physics and the technology, e.g. low activation materials, have to be further developed.

3.6 High Confinement

The high confinement mode (H-mode) was discovered at ASDEX, the predecessor of ASDEX Upgrade, in 1982. Its existance became evident, during a phase of extensive heating, which led to an increase in plasma density, despite no further gas-puff had been brought into the plasma. The realisation of H-modes can be attributed to an edge transport barrier, the so called **pedestal**, which suppresses the local turbulence.

The impact of the H-mode on the fusion triple product is remarkable, since the energy confinement time increases by a factor of two, or even more. Therefore, the H-mode is considered as a standard scenario for magnetic fusion devices [40].

3.6.1 L- and H- modes

As explained in [41], the transition from L- to H-mode occurs when the heating power P_{heat} exceeds a certain threshold P_{thr}. Experimentally, this transition can be observed, as soon as the particle-outflux, as well as the the radiated plasma energy, is reduced.

Furthermore, L- and H- mode profiles are also easily distinguishable, due to the formation of the pedestal. Profiles are spatial functions of a respective plasma physical paramter.

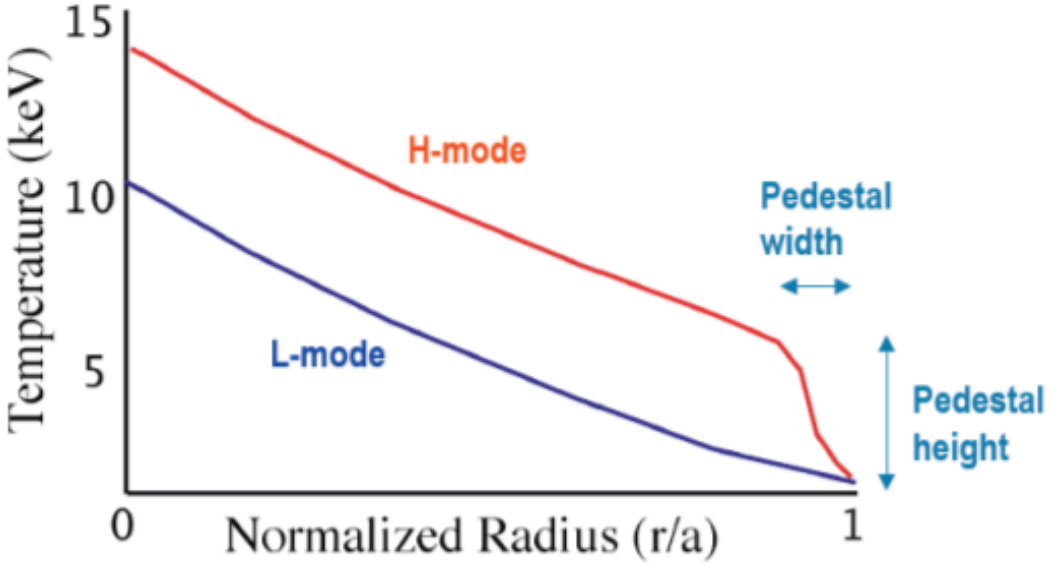

Figure 12: Comparison of a L- and H-mode temperature profile [42]

Figure 12 depicts temperature profiles for a H- (red) and L- (blue) mode, which are plotted against the normalized small plasma radius (usually given as ρ). Due to the pedestal, H-mode profiles are usually fitted by a mtanh [43], while the L-mode could be fitted by a msinh, due to less bending.

3.6.2 Confinement Scaling laws

Since turbulence in plasma is hard to quantify, transport processes and the respective energy confinement times τ_e are usually described by empirical scaling laws. The general ansatz of an empirical scaling law takes geometric parameters, like the major radius R, externally controlled parameters, like the heating power P, as well as parameters which depend on the respective hydrogen isotopes e.g. the atomic mass A, into account [18]. A possible ansatz can therefore be written as:

$$\tau_e = c_0 R^{c_1} a^{c_2} \kappa^{c_3} \delta^{c_4} B^{c_5} I^{c_6} P^{c_7} n^{c_8} A^{c_9} \tag{13}$$

The respective constants $c_0 ... c_9$ have to be fitted to the experiment. Alternatively, when considering confinement, the three dimensionless parameters β, r_{g*} and ν_{g*} can be taken into consideration [18, 37]. The parameter β is a measure for confining plasma pressure within a magnetic field. It can be defined as:

$$\beta = \frac{\langle p \rangle}{B^2/2\mu_0} \tag{14}$$

with $\langle p \rangle$ being the mean pressure of the plasma. The importance of the other two parameteres is furhter elaborated in [13]. The normalized gyro radius can be written as:

$$r_{g*} = r_{g,i}/L \tag{15}$$

and the normalized collisionality:

$$\nu_{g*} = \nu L/v_{th} \tag{16}$$

where L is a geometrical parameter, e.g. the minor plasma radius a. When using scaling laws, it should be kept in mind, that there is often a limited range of applicability. Several scalings were derived, using data from specific machines and for specific regimes. Therefore, extrapolations should be wielded carefully.

3.7 Heating Methods

As explained in chapter 3.5, the fusion triple product has its minimum at a temperature of approximately 10 keV. It should be noted, that one electron volt is equivalent to roughly 11,600 K.

In order to reach temperatures of this magnitude, there are usually several heating methods within magnetic fusion experiments, which will be introduced below.

3.7.1 Ohmic heating

In tokamaks, plasma carries its own current. Due to the resistivity of the plasma, the current leads to electron-ion collisions and thereby to a heating of the plasma. If an electric field is applied to a plasma, its electrons accelerate until a drift velocity v_d sets in. At this point, the force induced by the electric field is compensated by the force

due to collisions [37]:

$$eE = \dot{p_c} \tag{17}$$

where $\dot{p_c}$ describes the force due to collisions.

The resistivity is given by Ohms law E = $\eta \cdot j$. Furthermore, by introducing a momentum loss time τ_c for the electron, equation 17 can be rewritten as:

$$e\eta j = \frac{m_e v_d}{\tau_c} \tag{18}$$

Activating equation 18 towards the resistivity η, leads to:

$$\eta = \frac{m_e}{n_e e^2 \tau_c} \tag{19}$$

According to [37], collision times are proportional to $\propto \frac{\epsilon_0^2 \sqrt{m} T^{3/2}}{n e^4 ln\Lambda}$ with $ln\Lambda$ being the coulomb logarithm. Since equation 19 does not consider the fact, that particle velocities underlay a Maxwell-Boltzmann distribution, the resistivity of single charged ions is roughly the half of equation 19. By assuming that $\tau_c \approx \tau_e$, with latter being further described in [37], equation 19 can be written as:

$$\eta = 0.51 \frac{\sqrt{m_e} e^2 ln\Lambda}{3\epsilon_0^2 (2\pi T_e)^{3/2}} \tag{20}$$

The main focus should be put on the $\eta \propto T^{-3/2}$ dependency in equation 20 . As a consequence, ohmic heating is only effective for lower temperatures. As explained above, the standard scenario for Fusion devices will be the H-mode. As a result, ohmic heating will only provide a small friction of the needed heating power when transmitting to H-mode.

3.7.2 Neutral beam injection

The power source, which usually has the highest share at fusion experiments, is the neutral beam injection (NBI), which cover 20 MW out of a total of 27 MW heating power at ASDEX Upgrade.

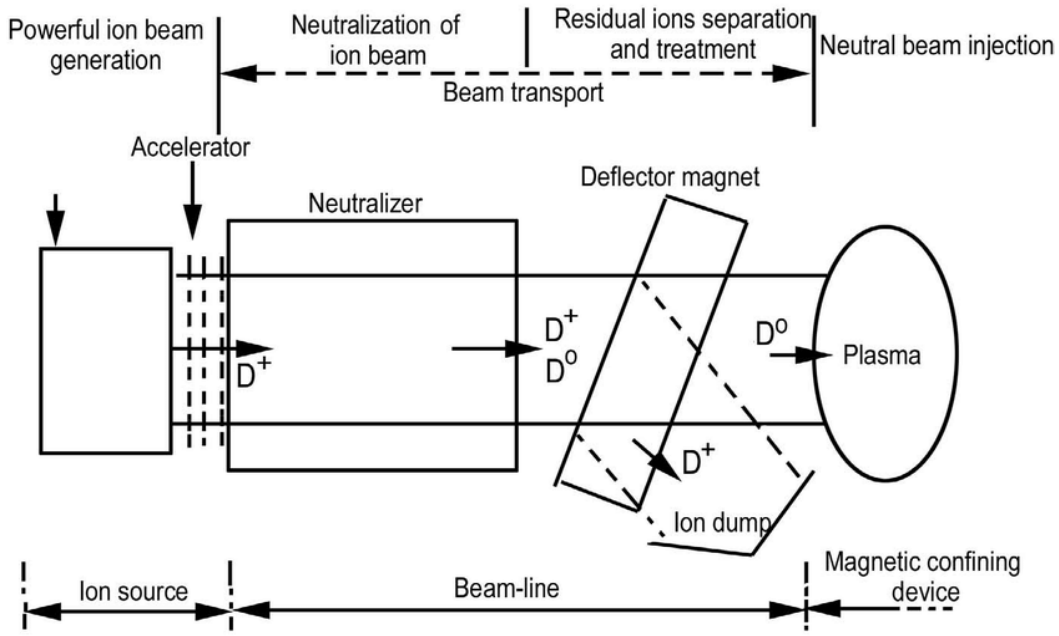

Figure 13: Schematic structure of NBI [44]

Figure 13 depicts the schematic structure of NBI. While there is no doubt, that neutral particles are needed to avoid a deflection of the beam, the process starts with a beam of charged Deuterons (D^+) which are accelerated by a certain potential. Then, the Deuterons undergo a neutralizer which is filled with gas. Thereby, the vast majority of Deuterons recombine to a neutral particles, since they absorb the surrounding free electrons of the gas. After passing the neutralizer, there are still charged particles left, which are then deflected by a magnet to ensure, there are no charged particles left. However, there is another issue that prevents a fraction of particles to not penetrate as deep as they should. It arises from the beam, also containing D_2^+- and D_3^+ ions, which undergo the same potential and are being accelerated to the same kinetic energy as the D^+ ions. As a result, they only have one half or one third of the velocity of the D^+ ions.

As described in [37], the particles aquire a charge, as soon as they collide with plasma particles. As a result the particles describe orbits within the plasma. This effect of particle trappings has to preferably happen in the center of the plasma, where the heating power is needed. Therefore, an appropriate absorption has to be present, since a too high absorption would lead to a primary heating of the plasma edge. A too low

absorption, would result in the beam transmitting trough the plasma and damaging the material. The absorption of the beam takes place, due to either charge exchange, ionization by ions, or ionization by electrons. For additional context, see reference [37].

3.7.3 Wave heating

When studying wave heating, Landau damping has to be considered firstly. If an external longitudinal wave traverses the plasma and latter is described by a velocity distribution, which contains more fast particles compared to the phase velocity of the wave, than slower ones, then the external wave would absorb the excessive energy. If, however, a distribution with less fast particles than slow particles is present, the wave would emit parts of its energy to the plasma, which would result in a damping of wave [18]. Landau damping therefore provides a procedure, in which waves, that are perpendicular to the plasma, are converted to longitudinal waves by a magnetic field. These waves, if a correct phase velocity is chosen, will provide their excessive energy to the plasma.

To achieve the necessary phase velocities for Landau damping to happen, the resonant frequencies for electrons and ions have to be considered. For electrons, this specific frequency is called electron cyclotron resonance frequency, is around the order of 70...200 GHz and leads to electron cyclotron resonance heating (ECRH). For ions, the frequencies are around the order of 20...100 MHz and lead to ion cyclotron resonance heating (ICRH). There are also so called hybrid frequencies, at which both electrons and ions could be heated, which range from 2 to 10 GHz. In fact by e.g. using ICRH, electrons are also indirectly being heated, since the rate of collisions is increased. According to ref. [37], the resonance frequency for a Deuteron is 38 MHz, which would result in a wave length of 8 m. Since the respective antenna has to be of similar dimension, the antennas for ICRH are way bigger compared to ECRH, where a resonance frequency of 100-200 GHz would result in a wavelength of 1-2 mm.

3.8 Measurement of density and temperature

Plasma diagnostics provide methods of observing and adapting plasma physical parameters. Furthermore, their data is the foundation for determining important quantities like plasma energy or impurity content (Z_{eff}).

Since, for this thesis, density and temperature data were accessed and processed quite often, methods of measuring these two parameters will be introduced below.

The most important diagnostics, when it comes to determining temperature and density, are laser diagnostics, which can provide high spatial and temporal resolution, a high spectral brightness and a negligible pertubation of the plasma. Furthermore, laser beams can interact with the plasma by either absorption, reflection, refraction and scattering [37]. While there are different diagnostics for each of these processes, this chapter will solely discuss interferometry, as well as Thomson Scattering (TS).

3.8.1 Interferometry

Interferometry is primarily used to measure the plasma electron density and is based on a phase shift of a laser beam which passes through the plasma. To connect the phase shift to a plasma density, a refractive index is needed which is, due to the high ratio of ion to electron mass (≈ 1862), in a hot plasma, vastly dominated by electrons. The plasma dispersion relation provides the relation between the electron density n_e and the refractive index μ, which usually has **n** as symbol, but has been changed to avoid a mix-up with particle density. Using equations (10.3.1) and (10.3.2) from [37], which assume a collision-free plasma, the refractive index can be computed, using:

$$\mu = 1 - \Big(\frac{e^2}{8\pi\epsilon_0 c^2 m_e}\Big) n_e \lambda_0^2 \tag{21}$$

where λ_0 is the wavelength of the laser.

ASDEX Upgrade uses a submillimeter inferometer, which uses a deuterium cyanide laser (DCN) with a wavelength of 195 μm [45]. There are five spatial sightlines, which provide a time continous measurement of electron density n_e, assuming that the den-

sity is constant on a flux surface ($n_e = n_e(\rho)$). As shown in figure 14, channels H1-H3 are dedicated to measuring the core density, while H4 and H5 are providing data for the edge density.

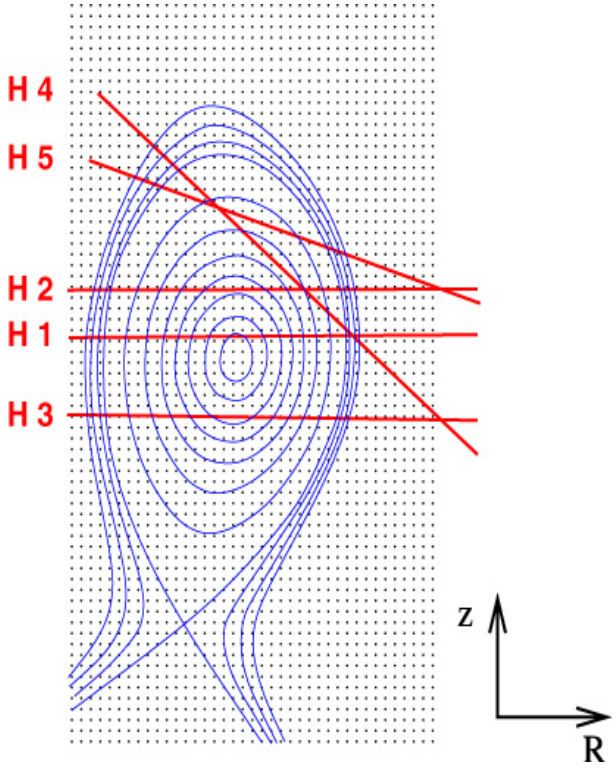

Figure 14: Spatial position of DCN channels [45]

3.8.2 Thomson Scattering

Thomson Scattering can be used to determine the electron density as well as the ion- and electron temperatures. At short laser wavelengths, the total scattered power can be obtained by summming over the scattered power from each electron. Therefore, the total scattered power can be used to determine the electron density [37]. However, if the wavelength of the laser is larger than the Deybe length λ_D [46], the scattering also descends from ions, turbulences and other collective effects [37].

Assuming a Maxwell-Boltzmann distribution for the electrons and laser wavelengths $<< \lambda_D$, the power scattered by electrons can be given by eq. (10.3.7) from [37]:

$$P_s = \frac{C_3 r_e^2}{\lambda_0} n_e L P_0 \frac{c}{v_{T,e}} \cdot \exp -C_4 \Big(\frac{c}{v_{T,e}} \Big)^2 \tag{22}$$

where r_e is the electron radius, L the interaction length between the scattered and incident ray and $v_{T,e}$ the thermal velocity of the electrons. Equation 22 solely describes plasma below $\approx$ 1 keV, since a partially relativistic plasma would require a Maxwell-Jüttner distribution to be taken into account.

The electron temperature T_e can be obtained, by considering the width of corresponding curve of equation 22.

Reference [47] can be considered, for a detailed overview of the technical implementation of TS at ASDEX Upgrade. AUG is provided with six Nd-YAG lasers, with each laser having a repetition rate of 20 Hz. The scattered light is recorded by 16 spatial channels which are aligned along each other, with a spacing of 2 mm.

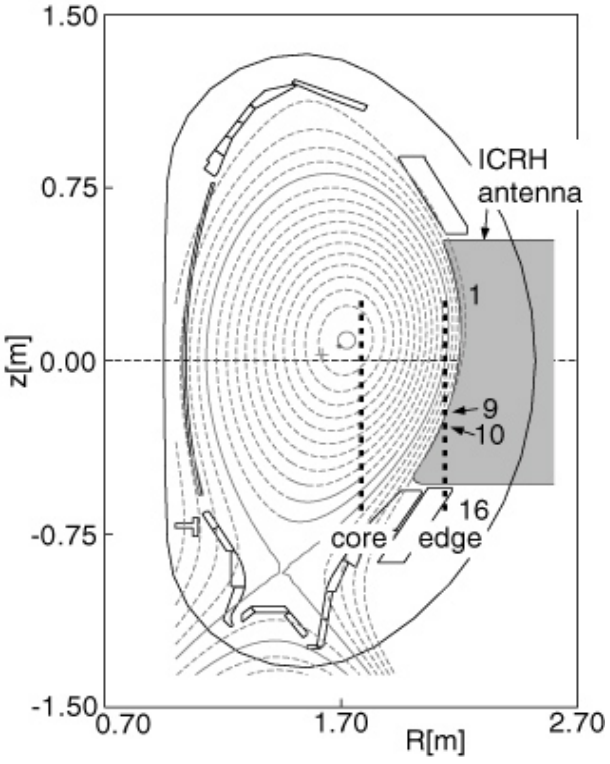

Figure 15: Position of TS scattering volumes at ASDEX Upgrade [47]

Figure 15 depicts the spatial locations of the scattering volumes 1-16. At ASDEX Upgrade, a minimum density of $n_e = 0.75 \cdot 10^{18}\ m^{-3}$ can be measured, using TS.

3.8.3 The Greenwald limit

The Greenwald density n_{Gw} has already been used in figure 3 and will often serve as a factor of density normalization within this thesis. The Greenwald density, generally

speaking, describes a density limit. Therefore, this subsection will given an outline, why there even is a density limit in a fusion plasma and how the Greenwald density n_{Gw} can be determined. For additional information, see [48].

A plasma cannot have a arbitrary high density, due to:

- losses at the plasma edge, e.g. convection and impurity radiation
- radiation from impurities in the plasma core
- degradation of plasma confinement in the core by too high densities
- insufficient fuelling methods

According to [48], a density limit is usually given in the form of a line averaged density, which can be calculated by:

$$\overline{n_e} = \kappa \cdot \langle \vec{j} \rangle \tag{23}$$

where κ is the plasma elongation and $\langle \vec{j} \rangle$ the averaged current density, which can be obtained, by dividing the total current by the respective cross-section area [48].

As described in [49], the Greenwald limit can be defined as a limit for the line-averaged density $\overline{n_e}$. If the Greenwald limit is exceeded, a higher frequency of discharge disruptions are engendered, due to a rise in magnetohydrodynamic (MHD) modes.

As worked out by Greenwald et. al in [48], this emprical limit can be described by:

$$n_{Gw} = \frac{I_p}{a^2 \pi} \tag{24}$$

where I_p is the total plasma current in MA, a the minor radius in m. As dimension for n_{Gw}, $10^{20}\ m^{-3}$ has to be chosen. Despite the limit, initially being developed for elliptic tokamaks, it can be applied to a wide range of machines (tokamaks).

4 Influence of the separatrix density on Confinement

The main incentive for observing the impact of the separatrix density $n_{e,sep}$ was initially given by figure 3, in which the confinement scaling H06(y,dd) [50] is depicted as a function of the line-averaged electron density $\overline{n_e}$, normalized to the Greenwald density n_{Gw}. As previously mentioned in the abstract, the data which has been used for this plot sprang from various plasma scenarios. While some of them had a technical focus (e.g. testing the pellet refuelling system), there were also discharges, which were conducted, using methods of confinement enhancement, e.g. Nitrogen Seeding or high plasma shaping. However, with the density exceeding the Greenwald density n_{Gw}, neither of these confinement enhancing methods provided further extra confinement, since the respected subsets converged to the trend of the technical discharges. This phenomenon can also be perceived, considering the H98(y,2) [51] confinement scaling instead. Figure 16 depicts the H98(y,2) scaling as a function of $\frac{\overline{n_e}}{n_{Gw}}$.

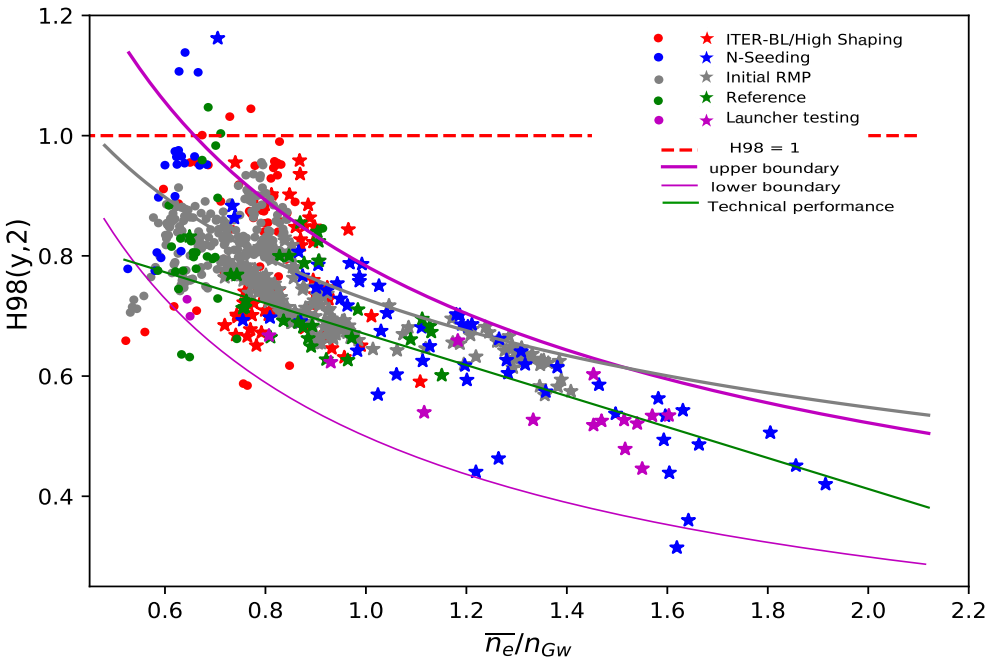

Figure 16: H98(y,2) scaling as a function of the normalized line averaged density

Figure 16 illustrates the unwanted phenomenon explained above. Beyond the Greenwald density n_{Gw}, there are no data points which would indicate extra confine-

ment enhancement. A potential factor of influence could be a rising separatrix density n_{sep}. Therefore, this chapter is dedicated to observe correlations between confinement and the separatrix density. Since the separatrix density is not effortlessly ascertainable, methods will be discussed, how n_{sep} can be determined.

4.1 Determining $n_{e,sep}$

As mentioned above, this analysis cannot be carried out, by simply accessing diagnostic data. This can be attributed to the fact that the exact position of the separatrix is unknown. If for instance, the separatrix position would be effortlessly available, the respective Thomson Scattering (TS) temperature profile could just be shifted so that the given separatrix temperature is at ρ_{pol} = 1. Next up, the TS density profile could be shifted by the same margin. Doing so, the separatrix density could therefore by defined as:

$$n_{e,sep} = n_e(\rho_{pol} = 1) \tag{25}$$

However, there are two aspects, which should be noted. Firstly, the separatrix temperature (position) would be required. For a 0th order analysis, it could be assumed that the separatrix temperature for H-mode dischrages is always T_{sep} = 100 eV [3]. However, as also described in reference [3], this value can vary up to $\pm$ 30 eV. With the gradient in temperature and density beeing rather steep at the edge, this would lead to a considerable uncertainty in n_{sep}.

Secondly, the method of shifting profile data can solely be applied to TS data. Therefore, only TS profiles could be used for this specific approach, despite profiles from Integrated data analysis (IDA) [52, 53] would be more precise, since IDA considers multiple diagnostics, such as TS, Interferometry and the Helium beam, to obtain improved profiles.

All things considered, another procedure would be desirable, which provides a

more precise value for the separatrix position. Therefore, section 4.2.1 will cover a possible approach, introducing a heuristic drift based model to determine the separatrix position.

4.2 Determining the separatrix Position

As brought up above, method will now be introduced, which aims to provide a more precise determination of the separatrix temperature.

4.2.1 Heuristic drift based model

Key literature for this subsection is ref. [4], providing a drift-based model for the power scrape-off width in low-gas-puff H-mode scenarios. Since the vast majority of the analysed discharges (within the high confinement pellet database) used pellet injection, this model seems to be appropriate for this analysis.

References [4] primary focus was to determine the width of the scrape off layer (SOL), by either using the balance of drifts into and out of the SOL, or the perpendicular thermal electron diffusivity as dominant heat flux. While the width of the SOL is an important parameter, e.g. for determining the effective ion charge number Z_{eff} at the plasma edge, for this analysis, the separatrix temperature is of main interest. As for that, reference [4] assumes a 2-point model [54, 55], which balances the input power into the SOL with thermal conduction losses towards the divertor. While the most relevant formulas for determining the separatrix temperature T_{sep} are given, reference [4] can be considered for additional information. Firstly, the width of the SOL can be computed, using one of the following equations.

$$\lambda = \frac{4a}{\bar{Z}eB_pR}\Big(\frac{\bar{A}m_pT_{sep}}{1+\bar{Z}}\Big)^{1/2} \tag{26}$$

$$\lambda = \frac{4a}{eB_pR}\Big(\frac{\bar{A}m_pT_{sep}}{1+\bar{Z}}\Big)^{1/2} \tag{27}$$

Whereas equation 26 uses ion drift and equation 27 electron drift. Furthermore, SI

units are used and the poloidal magnetic field B_p is given by $\frac{\mu_0 I_p}{\pi[2(\kappa^2+1]^{1/2}}$. Moreover, the parameters $\bar{Z}$ and $\bar{A}$ can be determined, using:

$$\bar{Z} = \frac{n_e}{\sum_i n_i} \tag{28}$$

$$\bar{A} = \frac{\sum_i A_i n_i}{\sum_i n_i} \tag{29}$$

By assuming the total particle flux crossing the separatrix to be solely induced by $\nabla \times \vec{B}$ and $\nabla \vec{B}$ drifts and that half of the flux returns to the plasma via Pfirsch–Schlüter flows, while the other half leaves the plasma through the divertor [4], a formula for the particle confinement time can be given by:

$$\tau_p = \frac{\pi B R a \kappa n_{core}}{2(T_{sep}/e) n_{sep}} \tag{30}$$

It should be noted, that T_{sep}/e is numerically equivalent to giving T_{sep} in electron volts.

Since Chapter 5 also focuses on determining particle confinement times τ_p, equation 30 will be further considered in the Appendix. For now, it should be mentioned that a relation between a particle confinement time τ_p and the separatrix temperature T_{sep} already indicates a correlation between confinement and the separatrix density n_{sep} (since in 0th approximation $P_{fus} = n \cdot \tau \cdot T$ and T_{sep} and n_{sep} are related).

By considering thermal electron diffusivity as main form of heat transport and by describing the particle fluxes, mentioned above, with electron heat [4], the separatrix temperature can be given using:

$$\frac{T_{sep}}{e} = 30.81 \cdot P_{SOL}^{1/4} \cdot \left[\frac{1+\bar{Z}}{2\bar{A}}\right]^{1/8} \cdot \frac{a^{1/4}(1+\kappa^2)^{1/4} B^{1/2}}{I_p^{1/4}} \cdot \left(\frac{Z_{eff}+4}{5}\right)^{1/4} \tag{31}$$

Here, P_{SOL} refers to the net power, being put into the SOL. Furthermore, I_p is the plasma current, B the magnetic field, a the small plasma radius and κ the plasma elongation. $\overline{Z}$ and $\overline{A}$ are defined in equations 28 and 29. Furthermore, Z_{eff} is the

effective ion charge number. Since Z_{eff}, $\overline{Z}$ and $\overline{A}$ are hard to obtain, the next subsection focuses on an approach of estimating them, in order to compute equation 31.

4.2.2 Estimation of Z_{eff}, $\overline{Z}$ and $\overline{A}$

To estimate $\overline{Z}$, the definition of thermal plasma energy W_{th} should be considered.

$$W_{th} = W_{mhd} - W_{fi} = \int_V n_e(\rho)T_e(\rho)dV + \int_V n_i(\rho)T_i(\rho)dV - W_{fi} \tag{32}$$

Since the ion density n_i is usually hard to obtain, the definition of $\overline{Z}$ (equation 28) can be used. Thereby, equation 32 can be written as:

$$\frac{1}{\overline{Z}} = \frac{W_{mhd} - W_{fi} - \int_V p_e(\rho)dV}{\int_V n_e(\rho)T_i(\rho)dV} \tag{33}$$

To determine $\overline{Z}$, volume integrals over the plasma volume have to be carried out. How numerical volume integrals can be computed, see Appendix. The effective ion charge Z_{eff} can be defined by:

$$Z_{eff} = \frac{\sum_i n_i Z_i^2}{\sum_i n_i Z_i} = \frac{\sum_i n_i Z_i^2}{n_e} \tag{34}$$

where n_e is the electron density, n_i the ion density of the species i and Z_i the respective charge number.

While $\overline{Z}$ is accessible by performing the respective volume integrals, Z_{eff} and $\bar{A}$ can now be estimated, if impurity concentrations of the respective species are known. In many cases, it can be assumed that, only one impurity species c_1 is dominant. Examples for such scenarios would be to only consider Boron, shortly after Boronization, or Nitrogren, when Nitrogen Seeding was applied. Using equations 28, 29 and the definition of Z_{eff}, as well as replacing the ion densties by the respective concentrations, Z_{eff} and $\bar{A}$ can be approximated by:

$$Z_{eff} \approx \frac{1 - c_1 + Z_1^2 \cdot c_1}{\bar{Z}} \tag{35}$$

and

$$\bar{A} \approx 1 - c_1 + c_1 \cdot A_1 \tag{36}$$

where c_1, Z_1 and A_1 refer to the concentration, charge number and atomic mass of the dominant impurity species. Equations 35 and 36 could be easily adjusted, if more than one impurity species have to be considered.

4.2.3 Results of the T_{sep} analysis

For this analysis, a total of 20 (out of 43) discharges of the high confinement database have been considered. Criteria for a discharge to be considered were:

- Reliable TS profiles for density and temperature
- The availability of either Z_{eff} or ion temperature profiles to determine $\overline{Z}$ (Z_{eff} and $\overline{Z}$ can be converted into each other by using equation 35)

Those conditions were met by 12 Nitrogen-Seeding discharges, four Reference (technical) discharges and 4 discharges, where High Shaping (ITER BL) has been applied.

To compute equations 35 and 36, Nitrogen has been considered as the dominating impurity species for Nitrogen seeded discharges. Furthermore, Boron has been assumed to be the primary impurity for High Shaping and the References discharges. While the Boron concentration was obtained from Charge Exchange Recombination Spectroscopy (CXRS), the Nitrogen concentration was obtained, using eq. (3) of reference [56]:

$$c_N^{flux} = \frac{\Gamma_N/7}{\Gamma_D + \Gamma_N/7} \tag{37}$$

With Z_{eff}, $\overline{Z}$ and $\overline{A}$ being determined, equation 31 could be computed. Figure 17 depicts the calculated separatrix temperatures, plotted in a histogram.

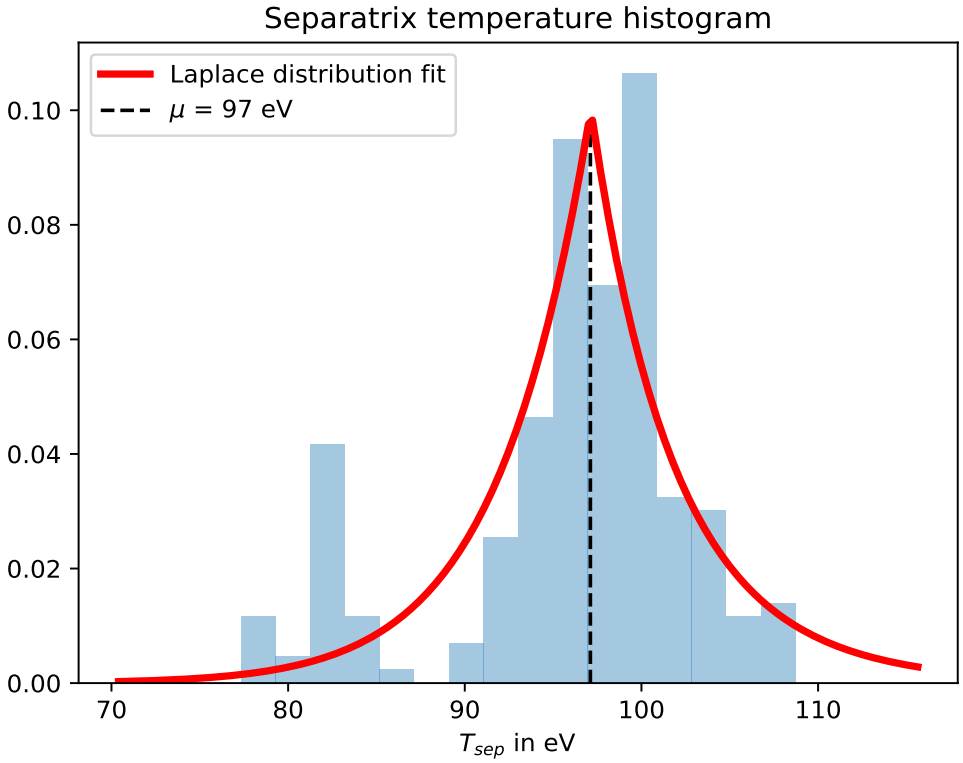

Figure 17: T_{sep}, plotted in a histogram, which has been complemented by a Laplace distribution and its expectancy value μ

The histogram im figure 17 has been complemented by a fitted Laplace distribution, whose expectancy value is equivalent to the median [57] (black dotted line). The median of the fitted distribution is given at ≈ 97 eV. Furthermore, a scattering of approximately $\pm$ 20 eV can be perceived.

With the separatrix temperature T_{sep} being available, the respective radius ρ_{sep} of the TS temperature profile could be determined. To eventually get the separatrix density $n_{e,sep}$, the TS density profile at ρ_{sep} had to be gathered.

4.2.4 Impact of $n_{e,sep}$ on confinement

When considering the impact of the separatrix density $n_{e,sep}$ on confinement, it is standing to reason to observe its impact on an H-factor. An H-factor normalizes the thermal energy confinement time τ_{th}, which can be obtained from experimental results, to an energy confinement time scaling $\tau_{e,pred_x}$ similar to equation 13:

$$H_x = \frac{\tau_{th}}{\tau_{e,pred_x}} \tag{38}$$

With the thermal energy confinement time being defined as:

$$\tau_{th} = \frac{W_{th}}{P_{net}} \tag{39}$$

where W_{th} is the kinetic energy content, obtainable by integrating ion- and electron pressure profiles (equation 32) and P_{net} the absorbed share of total heating Power P_{tot}.

Figure 3 and 16 depict two different confinement scalings, H98(y,2) and H06(y,dd). It should be discussed, which of those two scalings is more appropriate for this analysis.

The H98(y,2) scaling was developed for predicting the confinement performance of ITER. It has to be mentioned that the density operation of ITER is likely to be kept below $0.85 \cdot n_{Gw}$. This in itself could already be an indicator of H98(y,2) being inappropriate for describing confinement data in regimes of higher density than $0.85 \cdot n_{Gw}$. H98(y,2) can be defined as:

$$H98(y,2) = \frac{\tau_{th}}{\tau_{th}^{IPB(y,2)}} \tag{40}$$

Where $\tau_{th}^{IPB(y,2)}$ is the actual energy confinement time scaling which considers the following free parameters in a power law [1]:

$$\begin{aligned} \tau_{th}^{IPB(y,2)} =& 3.31 \cdot 10^{-11} \cdot 2^{0.19} \cdot I_p^{0.93} \cdot P_{net}^{-0.74} \cdot R^{1.39} \cdot a_0^{0.58} \cdot \kappa^{0.78} \\ & \cdot B_t^{0.51} \cdot \overline{n_e}^{0.41} \end{aligned} \tag{41}$$

The H06(y,dd) scaling was developed for the IAEA conference (Chengdu) in 2006. Moreover, it is a global scaling for non-spherical tokamaks which meet the requirement of having an aspect-ratio ($\frac{R}{a}$) between 2.8 and 5.0 [50]. H06(y,dd) was assembled by a total of 14 tokamak teams and can be defined by:

$$H06(y,dd) = \frac{\tau_{th}}{\tau_{th}^{H06(y,dd)}} \tag{42}$$

Here, the actual confinement time scaling is $\tau_{th}^{H06(y,dd)}$ which can be computed [1], using:

$$\begin{aligned}\tau_{th}^{H06(y,dd)} =& 0.95 \cdot 7.3098 \cdot 10^{-7} \cdot 2^{0.2} \cdot I_p^{1.3678} \cdot P_{net}^{-0.74} \cdot (\frac{R}{a_0})^{2.48205} \\ & \cdot (\frac{R}{a_0})^{-0.9ln(R/a_0)} \cdot R^{1.2345} \cdot \kappa_a^{0.38} \cdot B_t^{0.12} \cdot \overline{n_e}^{0.032236} \\ & \cdot f_{Gw}^{-0.22ln(f_{Gw})} \cdot (\frac{q_{95}}{q_{cyl.}})^{0.77}\end{aligned} \tag{43}$$

With $q_{95}/q_{cyl.}$, $\tau_{th}^{H06(y,dd)}$ contains an extra free parameter compared to H98(y,2) which also considers the spatial shaping of the confined plasma as $q_{cyl.}$ is related to the triangularity δ and can be defined by:

$$q_{cyl.} = 5 \cdot 10^{-6} \cdot \kappa \cdot \frac{B_t a_0^2}{I_p R} \tag{44}$$

It has to be noted that the main difference of equations 41 and 43 are their density dependencies. While the H98(y,2) contains a fixed $\propto \overline{n_e}^{0.41}$ dependency, H06(y,dd) has a $\propto (\overline{n_e}/n_{Gw})^{-0.22ln(\overline{n_e}/n_{Gw})}$ dependency, in which the exponent gets smaller with rising density. The decrease of the exponent in depicted in figure 18

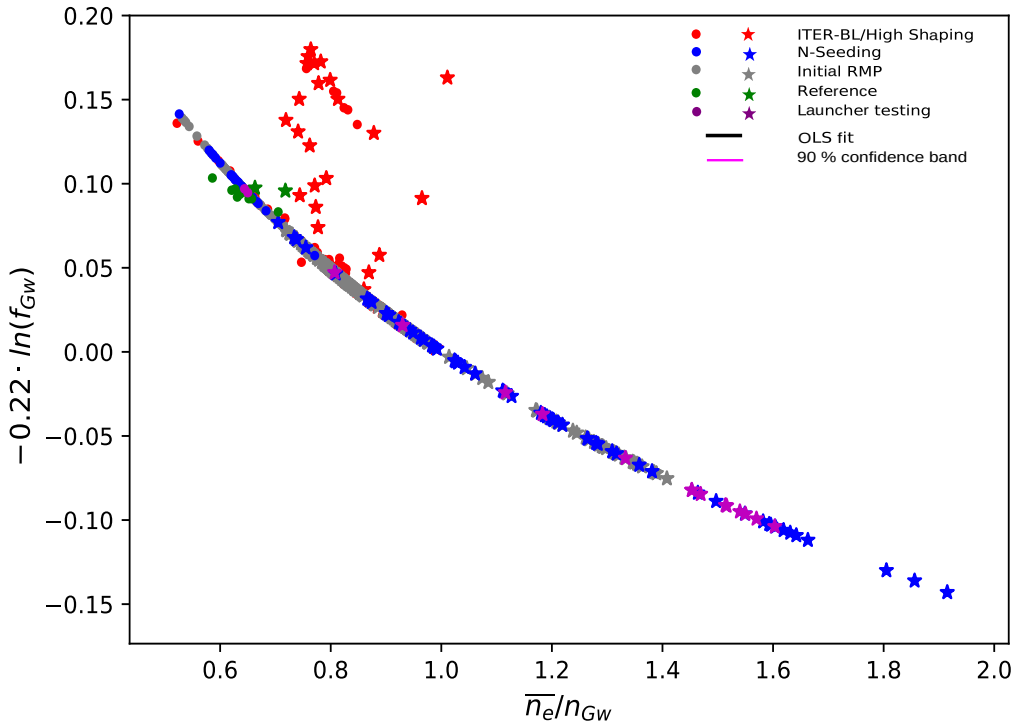

Figure 18: $-0.22 \cdot ln(\overline{n_e}/n_{Gw})$ as a function of $\overline{n_e}/n_{Gw}$ for several discharges of the pellet-fuelled high density database of AUG

Figure 18 shows the fashion, in which the exponent $-0.22 \cdot ln(\overline{n_e}/n_{Gw})$ declines with rising density.

All things considered, it becomes evident that solely H06(y,dd) should be further considered. This conclusion has also been drawn in reference [1].

Since the question, which confinement scaling is more appropriate to be analysed, has been clarified and the separatrix density has been determined, using the heuristic drift-based model [4], the correlation between H06(y,dd) and $n_{e,sep}$ can be observed. As for that, the discharges have been divided into three subsets. One subset contains several Nitrogen seeded discharges, the second subset was filled with High Shaping/ITER BL discharges and the last one with Technical/Reference discharges.

Possible correlations will be observed, using the correlation coefficient r. According to reference [58], the correlation coefficient can be computed by:

$$r_{xy} = \frac{s_{xy}}{s_x s_y} \tag{45}$$

where s_x and s_y are the standard deviations of the sample and s_{xy} the respective covariance.

Figure 19 depicts H06(y,dd) as a function of $n_{e,sep}$ for all three subsets.

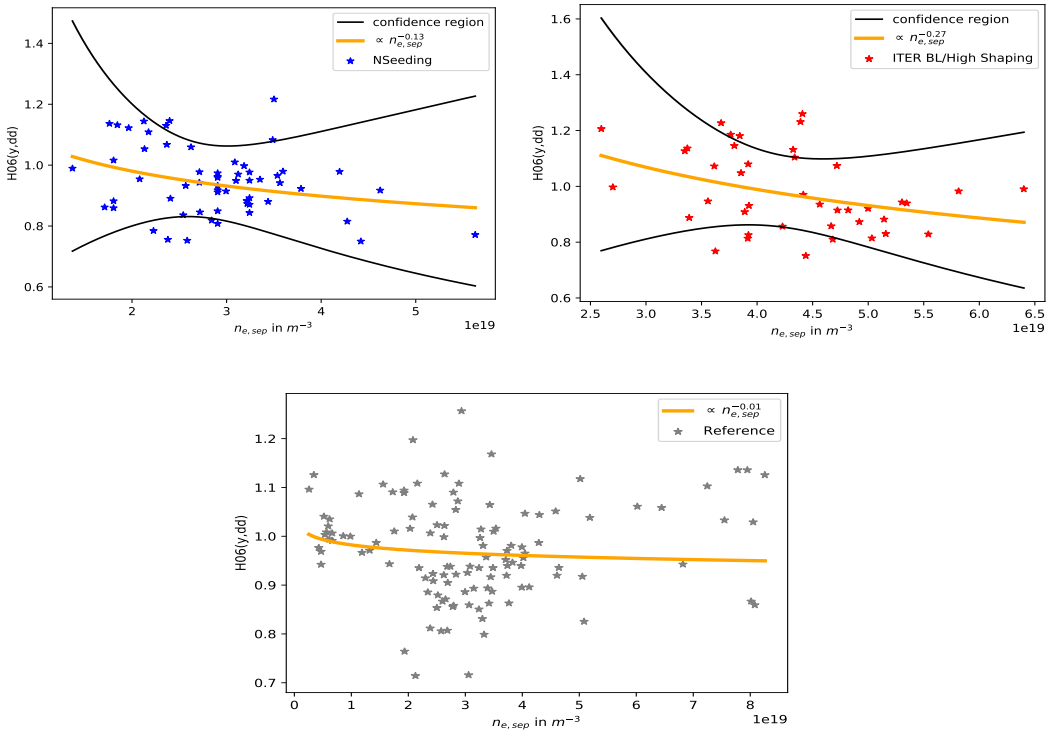

Figure 19: H06(y,dd) as a function of $n_{e,sep}$ for N-Seeding (blue), High Shaping/ ITER BL (red) and Reference discharges (grey)

The dependencies between H06(y,dd) and the separatrix density $n_{e,sep}$ for the three subsets are summarized in table 1.

Table 1: Resulting dependencies between H06(y,dd) and $n_{e,sep}$

Subset	H06(y,dd) $\propto$
N-Seeding	$n_{e,sep}^{-0.13}$
HS/ITER BL	$n_{e,sep}^{-0.27}$
Reference	$n_{e,sep}^{-0.01}$

While there are considerable negative correlations between H06(y,dd) and $n_{e,sep}$ for both confinement enhancing methods N-Seeding (r = -0.4) and High Shaping/ITER BL (r= -0.5), the correlation coefficient for the Technical shots, was analysed to be r = -0.02, which indicates that there is no correlation. This result might be a potential reason to explain the loss in extra confinement beyond the Greenwald density n_{Gw}. The dependencies within the legends of figure 19 have been obtained, performing a natural-logarithmic transformation (see Appendix).

However, as elaborated in reference [59], the Separatrix density is primarily dependent on the divertor neutral gas density n^0_{Div}. Therefore, a direct correlation between the Separatrix density $n_{e,sep}$ and the line-averaged density $\overline{n_e}$ seems unlikely.

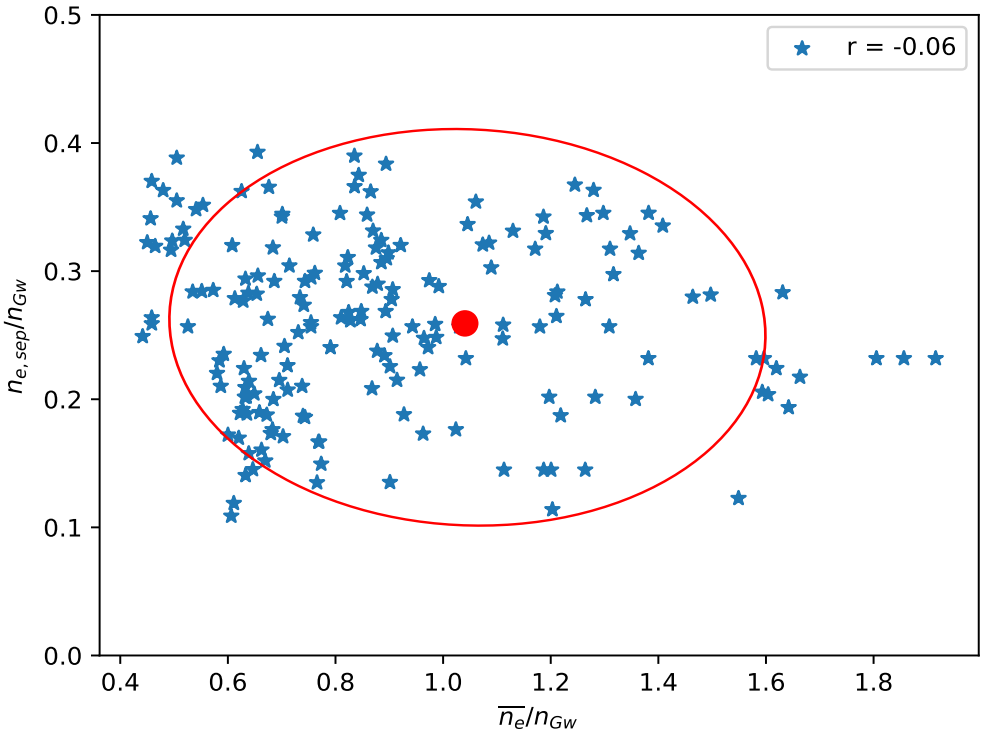

Figure 20: Separatrix density $n_{e,sep}$, normalized to n_{Gw} as a function of line-averaged density $\overline{n_e}$ also normalized to n_{Gw}

Figure 20 depicts the normalized separatrix density as a function of the normalized line-averaged density for the 20 discharges as one set. Even if the three subsets are considered separately, a similar trend and a similar correlation coefficient was found.

All things considered, a negative correlation between H06(y,dd) and $n_{e,sep}$ for N-Seeding and High Shaping/ITER BL scenarios has been found. Even though, no correlation between $n_{e,sep}$ and $\overline{n_e}$ seems likely, the Separtrix density in Figure 19 (a) and (b) was far away from being constant. As a consequence, there might be a (constant) loss in extra confinement independently of $\frac{\overline{n_e}}{n_{Gw}}$. Therefore, future observations on this topic, require a scenario, in which the separatrix (edge) density can be kept approximately constant. If a constant (low) separatrix density can be achieved throughout discharges, a vertical shift to higher values of certain data points in figure 3 might be the result.

4.3 Corelation between separatrix- and divertor density

As brought up above and discussed in [59], the divertor neutral gas density n_0^{Div}, seems to be the main influencing factor for the separatrix density n_{sep}. As elaborated in [59], a $n_{sep} \propto n_{0,Div}^{0.5}$ dependency has been predicted by the 2-point model. Experimentally, however, a weaker dependence of $\propto n_{0,Div}^{0.31}$ for N-Seeding discharges has been found. Therefore, this subsection focuses on observing this dependency for the given data-set of 20 discharges, by considering N-Seeding, High Shaping/ITER BL and Reference discharges separately. Moreover, further studies on this subject might lead to an empirical scaling law for n_{sep}, which makes this observation an important foundation. Since the separatrix density has been determined, using a 2-point model within reference [4], the focus will now be put on determining the divertor neutral gas density n_0^{Div}.

4.3.1 Measurement of the neutral gas density

One way of measuring the neutral flux are ionization gauges. As described in [60], the neutral flux is being measured by 20 gauges which are located at the upper and lower divertor, as well as around the main chamber. In ionization gauges, neutrals are entering the gauge and are getting ionized. The induced current is being measured, which leads to a maximum achievable resolution of one ms. However, a behaviour of saturation seems likely, if a certain value of neutral gas density is exceeded. The saturation

is further elaborated in ref. [61]. For a magnetic field of 6 T, the ionization gauges tend to saturate at approximately 15 Pa neutral gas pressure. For lower magnetic fields, the point of saturation tends to shift to higher pressures. Lastly it has to be mentioned, that the ionization gauges do not measure the neutral gas density, but the neutral gas flux density Γ_0. The conversion can be carried out, using $p_0 = n_0 \cdot T_0 \approx 1.6 \cdot 10^{23} \cdot \Gamma_0$ according to [61].

An alternative way of obtaining n_0^{Div} at ASDEX Upgrade (AUG), is a direct way of pressure measurement, carried out by baratrons, which have been installed since 2014 and are located below the inner and outer divertor [61]. The main advantage of baratrons is that there is no behaviour of saturation. As a consequence, the baratron data should be preferred for this analysis. However, since this set of data contains data up to 2011, the baratron data should be used for a calibration of the ionization gauge data.

4.3.2 Calibration of ionization gauges data

For this calibration, a total of 18 discharges (of the AUG high confinement pellet database) have been used, to compare the ionization gauge data with the baratron data. For this purpose, several subsets of plasma scenarios have been treated as one set of data. Figure 21 shows the baratron data (pressure) as a function of the ionization gauge data (density).

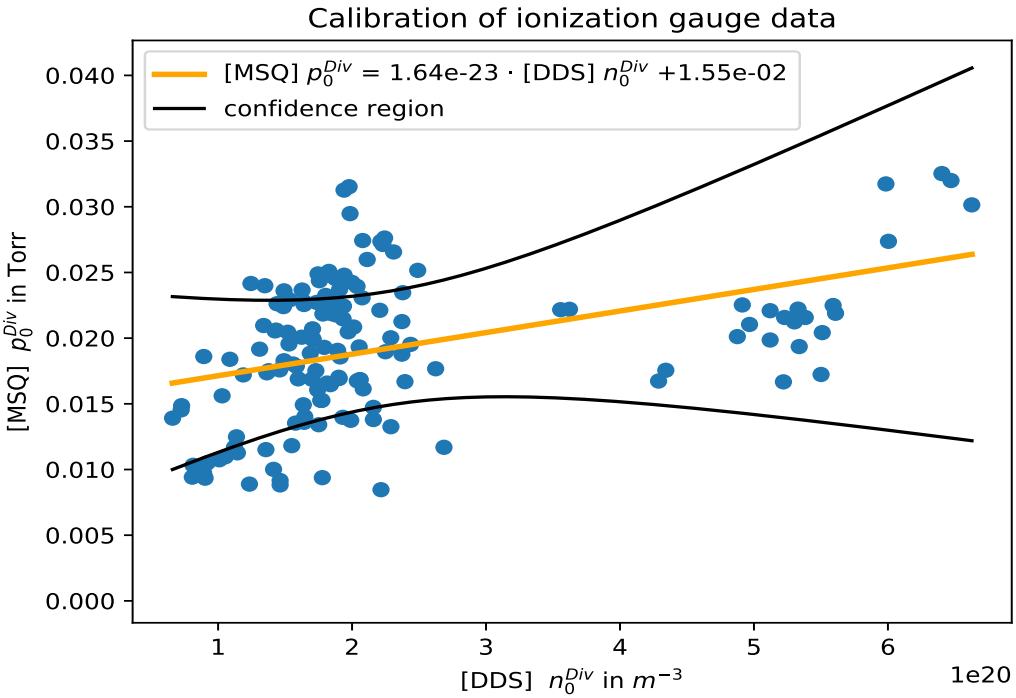

Figure 21: Baratron pressure values as a function of ionization density values

Figure 21 depicts the trend of baratron data, when being plotted against the data from ionization gauges. A typical saturation curve would be expected to trend linearly up to a certain point, beyond that point, a significantly steeper (non-linear) increase would be expected. Assuming that saturation of the ionization gauges starts at p_0 = 15 Pa (as mentioned above), this would be equivalent to a density of $n_0 \approx 3.6 \cdot 10^{21}\, m^{-3}$, which is significantly undershot in this specific case. Therefore, a linear fit has been chosen, for this margin of densities.

18 out of the 20 discharges, which have been used for the analysis of the separatrix density n_{sep}, have been conducted after 2014, thereby, baratron data is available for these discharges. The divertor neutral gas density for the remaining two discharges was calibrated, using figure 21. It should be noted, that the offset in the linear model of figure 21 is not meaningful from a physical point of view. However, since this calibration line should not get extrapolated anyways, the offset can be considered as a statistical tool to obtain a better fit. Lastly, the divertor gas pressure p_0 can be converted to a respective density, using $p_0 = n_0 \cdot T_0$.

4.3.3 Correlation analysis

Since both the separatrix density $n_{e,sep}$ and the divertor neutral gas density n_0^{Div} have been determined, analyses of their dependency for the three different subsets (N-Seeding, High Shaping/ITER BL and Reference) can be carried out. Figure 22 depicts the separatrix density as a function of the divertor neutral gas density for the three subsets.

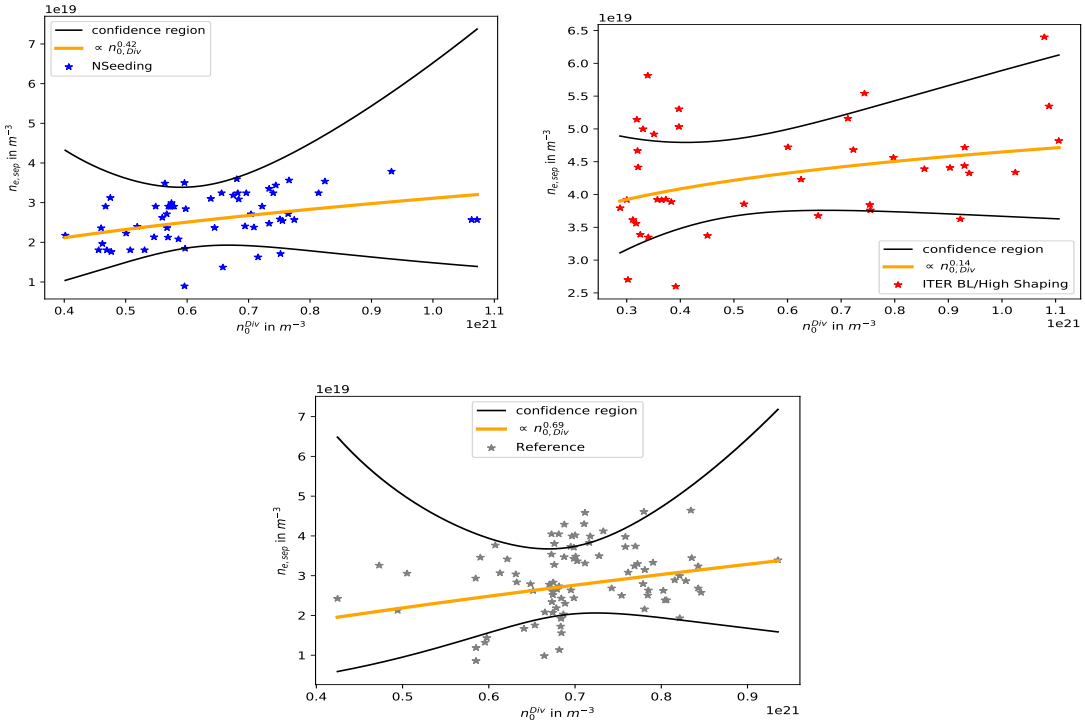

Figure 22: $n_{e,sep}$ as a function of n_0^{Div} for N-Seeding (blue), High Shaping/ ITER BL (red) and Reference discharges (grey)

When considering figure 22, a considerable positive correlation for all three subsets can be seen. The ascertained dependencies, depicted in the respective legends were obtained, by performing a natural-logarithmic transformation (Appendix). The dependencies of the three subsets are summarized in table 2.

Table 2: Resulting dependencies between $n_{e,sep}$ and n_0^{Div}

subset	$n_{e,sep} \propto$
N-Seeding	$n_{0,Div}^{0.42}$
HS/ITER BL	$n_{0,Div}^{0.14}$
Reference	$n_{0,Div}^{0.69}$

When comparing these results with the results of figure 19, it becomes evident, that the more $n_{e,sep}$ gets determined by the divertor neutral gas density n_0^{Div}, the less impact on confinement seems to be present. Furthermore, it can be inferred, that the loss in extra confinement is not arising from a variation in divertor neutral gas density.

All in all, this Chapter has shown, that a procedure to control the separatrix (edge) density is needed to conduct further analyses on this topic.

5 Efficient core fuelling by replacing gas-puff with pellets

As expounded in Chapter 5.5, an increase of the fusion triple product $n \cdot \tau \cdot T$ is equal to a rise in fusion power, which is the uppermost goal of nuclear fusion research. Since gradients in temperature and density are built up towards the plasma core, the region in close proximity to the plasma core is considered as the confinement region, where the vast majority of fusion reactions will take place (in future reactor concepts). Therefore, confining as many particles in the confinement region as possible is a pivotal goal. A parameter to quantify this process is the technical particle confinement time $\tau_{p,tech}$ which will be introduced in this section. While gas has the character of utilising as much space as possible, pellet fuelling is an essential method for sharpening the density profile locally, by depositing a substantial number of particles within the range of 10^{21} (one pellet). A particle confinement time τ_p, can be interpreted as a performance parameter like τ_e.

This section will give an overview of recent experiments, where gas-puff has been replaced by pellet fuelling, while keeping the total particle-influx virtually constant. This section covers the experimental set-up, results, possible models to interpret the results, as well as an outlook.

5.1 Experimental set up

During a recommissioning-phase of ASDEX Upgrade (AUG), technical discharges have been carried out, with the primary intention of testing the revised pellet refuelling system, by operating at every possible pellet frequency. Furthermore, the efficiency and reactor relevance of pellet fuelling was to be further observed. Since the discharges were conducted in a technical manner, the resulting plasma performances were rather moderate, as neither of the performance-related H-factors H_{98}(y,2) and H_{06}(y,dd) has been significantly exceeding H ≈ 1.

A total of ten H-mode discharges have been conducted and merged to one set of data. Within these experiments, the overall particle-influx Γ_{tot} has been held virtually

constant at $\Gamma_{tot} \approx 3.0 \cdot 10^{22} \frac{e}{s}$. Therefore, the first three seconds of each discharge started with solely gas-puff. Next up, the gas-puff has been partially exchanged by pellet fuelling, largely using interstages. After all available pellets have been injected, it was switched back to solely gas-puff for the remainder of the discharge. Other plasma-physical parameters have also been chosen to be equal for every discharge. For these scenarios a plasma current of I_p = 800 kA and toroidal magnetic field of B_t = 2.5 T was configured. Moreover, the heating power had been chosen to be the same for all discharges with $P_{heat} \approx$ 10 MW of NBI, ICRH, and ECRH. Several heating methods have been turned on, befor the fuelling exchange process began.

These specific scenarios also contained some technical and physical boundaries, which are also introduced in this subsection.

Firstly, the pellet system at ASDEX Upgrade has a maximum capacatiy of 96 Pellets. Therefore, arbitrary long pellet fuelling is not possible. Furthermore, the centrifuge of AUG has a maximum frequency of 140 Hz with only factors of 140 Hz being possible pellet frequencies f_p. The flux arising from pellet injection can be calculated by:

$$\Gamma_p = m_p \cdot f_p \tag{46}$$

where m_p is the pellet mass given in electrons per second. Due to the limitation in centrifuge frequencies, there is thereby also a limited spectrum of achievable pellet fluxes. However, variant pellet fluxes were desired which could not be configured. Therefore, a technical trick has been carried out. This trick involved switching between two frequencies, which led to timely averaged new frequencies and therefore new pellet fluxes. When it comes to operating the centrifuge, that for instance meant that pellets were injected after one or two idels of the centrifuge in alternation.

In order to for instance reach a pellet frequency 56 Hz, with a fixed centrifuge frequency of 140 Hz, a sequence of pellets and idels was needed, where one injected pellet, was followed by an idle and a new pellet. This results in a temporary frequency of 70 Hz. Next up, the second pellet was followed by two idels until the next pellet

was injected, resulting in a temporary frequency of 47 Hz. The total sequence therefore gets to pellet-idle-pellet-idle-idle. Due to the fixed centrifuge frequency one instance of this sequence lasts $\frac{1}{140}$ s. Therefore, the total time for one sequence is given by:

$$\bar{t} = 5 \cdot \frac{1}{140}\, s = \frac{1}{28}\, s \tag{47}$$

And the time averaged frequency $\overline{f}$ can therefore be calculated by dividing the number of pellets within the sequence by $\bar{t}$.

$$\overline{f} = \frac{n}{\bar{t}} = 56\, Hz \tag{48}$$

An illustration of this sequence can be found in Appendix.

With a total of 96 pellets, this would lead to an injection period of 1.7 s with a resulting pellet flux of $\Gamma_p \approx 2.0 \cdot 10^{22}$ e/s. When starting the discharge with a gas flux $\Gamma_{gas} = 3.0 \cdot 10^{22}$ e/s, this would mean that Γ_{gas} has to be reduced to $1.0 \cdot 10^{22}$ e/s in order to reach an approximately constant particle flux.

Figure 23 (bottom) depicts the adaptation of gas-puff after the injection period of pellets started. It should be noted, that the gas flux signal of figure 23 does not contain the total gas flux, since the gas was distributed on two chambers. Both chambers, however, have been adapted in the same manner perecentagewise.

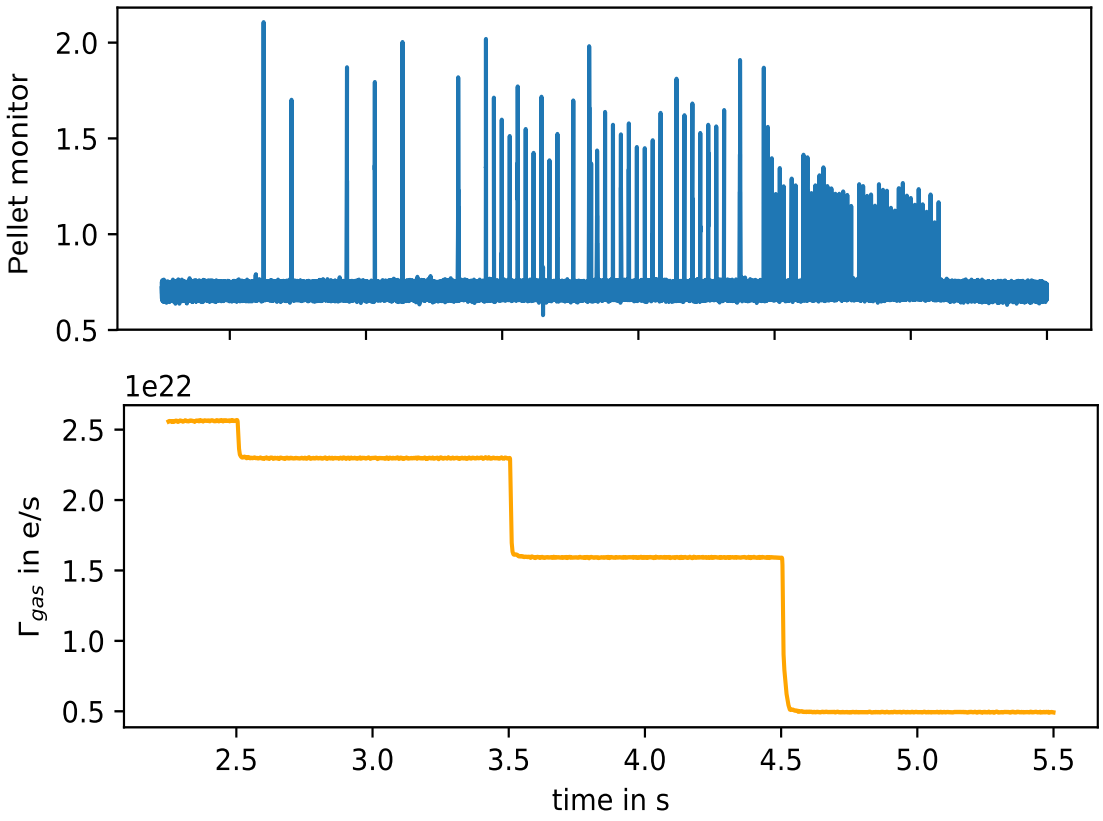

Figure 23: Adaptation of gas-puff of discharge #36992.

Another boundary was given by the fact, that the initial particle flux was chosen to be $\Gamma_{tot} = 3.0 \cdot 10^{22} \frac{e}{s}$. This means that even by choosing the maximum pellet frequency $f_p = 70$ Hz, only ≈ 85 % of the initial gas flux could be replaced.

5.2 Experimental results

The initial incentive behind the conducted discharges was to show that the edge density does not depend on the fuelling method, but on the total particle-influx (and therefore remains approximatley constant). This assumption can be substantiated considering the following model of particle conservation.

The purpose of this model is to section the plasma into different chambers, whereas each chamber contains a certain amount of particles. By describing all chambers with equations of particle-conservation, one can therefore keep track of the particle content within each chamber and can therefore make new findings on how to control refuelling

related plasma-physical parameters. In first approximation, the plasma is divided into three compartments: The core plasma, the scrape off layer (SOL) and the pellet. For this specific case, solely the particle conservation equations for the plasma core and the scrape off layer will be considered

$$\frac{\partial N_c}{\partial t} = \Gamma_{plt} - \frac{N_c}{\tau_c} \tag{49}$$

According to equation 49, a change in particle content of the core plasma, can be initiated by depositing pellets at a certain radial position ρ_{plt}. Independently of pellets being injected or not, several core plasma particles will leave the plasma core after a certain confinement time τ_c. The particle conservation equation for the SOL is given by:

$$\frac{\partial N_{SOL}}{\partial t} = \frac{N_c}{\tau_c} + \Gamma_{gas} - \Gamma_{pump} \tag{50}$$

In equation 50, a change in particle content is induced by the influx of particles coming from the main plasma, before getting recycled. Furthermore, there is the external gas-puff as a flux source and the pump as potential flux sink as it describes the particle recycling back into the plasma.

Now there are two conditions, which had to be achieved within this set of experiments. The first one was to maintain an approximately constant edge density. The second one was to, at the very least, not lose particle content within the core plasma (an increase is desired). Therefore the two conditions can be written, using equations 49 and 50;

$$0 \stackrel{!}{=} \Gamma_{plt} - \frac{N_c}{\tau_c} \tag{51}$$

$$0 \stackrel{!}{=} \frac{N_c}{\tau_c} + \Gamma_{gas} - \Gamma_{pump} \tag{52}$$

Combining equations 51 and 52 gives the final condition for this experimental set-up:

$$\Gamma_{pump} = \Gamma_{plt} + \Gamma_{gas} = \Gamma_{tot} \tag{53}$$

As a consequence, by keeping the sum of pellet and gas flux constant, one gets control over plasma particle recycling and thereby a constant edge density. Furthermore, as mentioned above, an increase in the plasma core particle content is desired. When considering equation 51, this would be equivalent to an increase in particle confinement time τ_c.

For future findings and experimental set-ups, the third plasma compartment (pellets) should be taken into consideration. Furthermore, since all plasma compartments are connected and therefore interact with each other, a linear system of differential equations would be the result. The differential equation system for this specific case (by also taking experimental results into consideration) can be found in Appendix.

The blue markers of figure 24 depict the electron edge density (obtained from Thomson Scattering) as a function of the normalized pellet flux $\frac{\Gamma_{plt}}{\Gamma_{tot}}$.

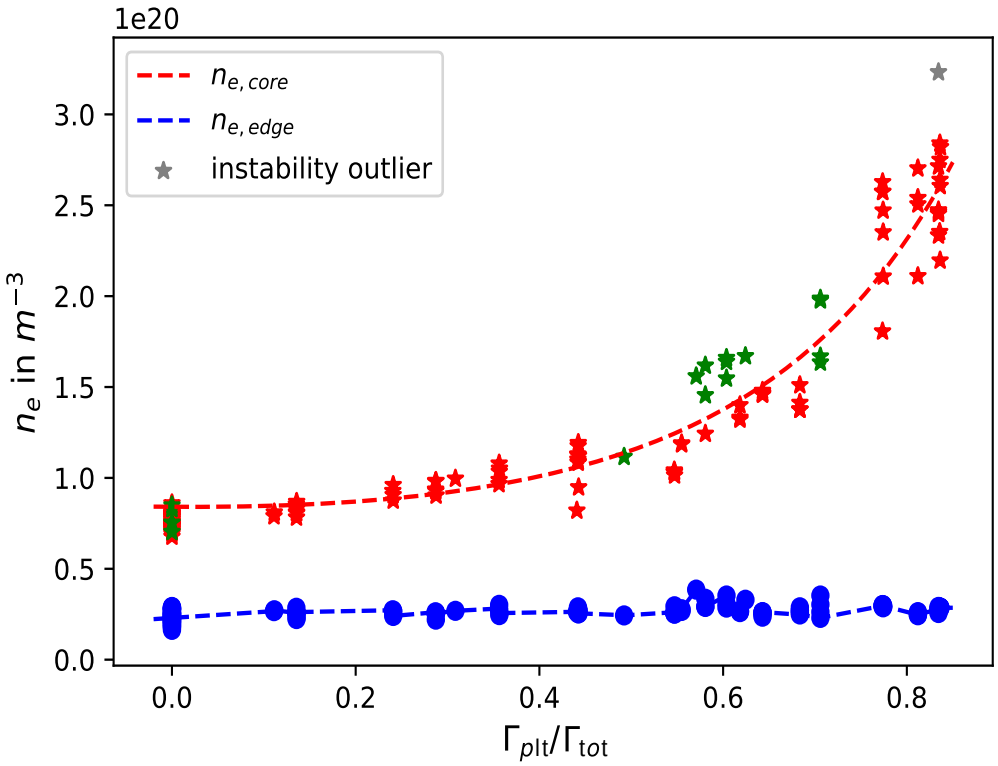

Figure 24: Electron- core density and edge density as a function of the normalized pellet flux

The resulting trend (dotted blue line) of figure 24 indicates that the edge density stayed virtually constant throughout all discharges.

While the main expectation of the planning phase has been met, figure 24 also depicts another pivotal result of this series of experiments, since the electron core density $n_{e,core}$ (red and green stars) rose in a supra-linear fashion when $\frac{\Gamma_{plt}}{\Gamma_{tot}}$ had been increased. Several density values of figure 24 were acquired from core- and edge Thomson scattering data. The green stars were obtained, by switching between two pellet frequencies as described in Chapter 5.1. The grey star is considered as an outlier due to heavy MHD mode activity during the pellet phase of discharge 37011. Possible models to describe the non-linear increase in $n_{e,core}$ can be found in Chapter 5.3.

5.2.1 Total plasma energy W_{mhd}

Since there is a supra-linear increase in core density, and thermal plasma energy being defined as $W_{th} = \int_V p(\rho)\, dV = \int_V n(\rho) \cdot T(\rho)\, dV$, an increase in W_{mhd} seems to be likely, if the share in pellet flux is raised. In first approximation, the other pressure defining parameter $T_{e,core}$ can be observed. If the core electron temperature $T_{e,core}$ also decreases in a similar fashion as the electron core density $n_{e,core}$ increases, then a constant core pressure would indicate the thermal energy W_{th} and thereby W_{mhd} to remain constant. Figure 25 shows the core electron temperature, obtained from Thomson Scattering as a function of the normalized pellet flux $\frac{\Gamma_{plt}}{\Gamma_{tot}}$.

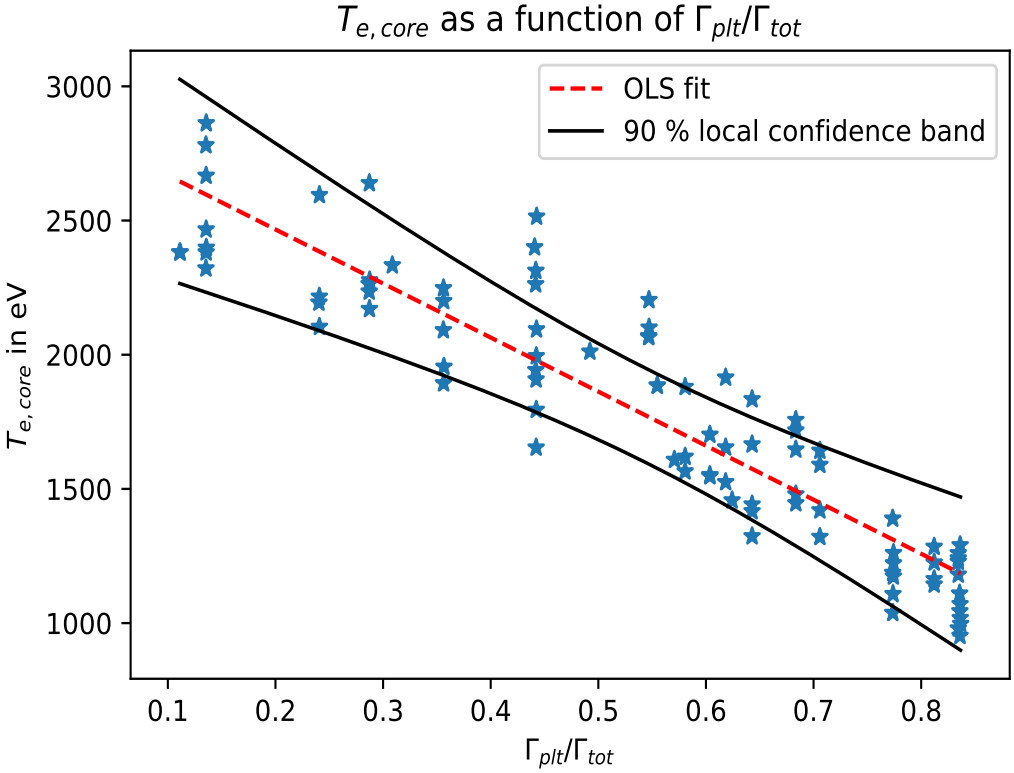

Figure 25: Electron- core temperature as a function of the normalized pellet flux. A 90 % local confidence band for predicting a single observation [62], is included

As depicted in figure 25, the electron core temperature decreases in an approximately linear fashion when the the share in pellet flux is increased. This can be attributed to the fact that pellets have an approximate temperature of $T_{plt} \approx 13$K [63]. As a result, a sharpening of the pressure profile within the confinement region and

therefore a higher plasma energy is expected.

Figure 26 illustrates how W_{mhd} varies with rising $\frac{\Gamma_{plt}}{\Gamma_{tot}}$.

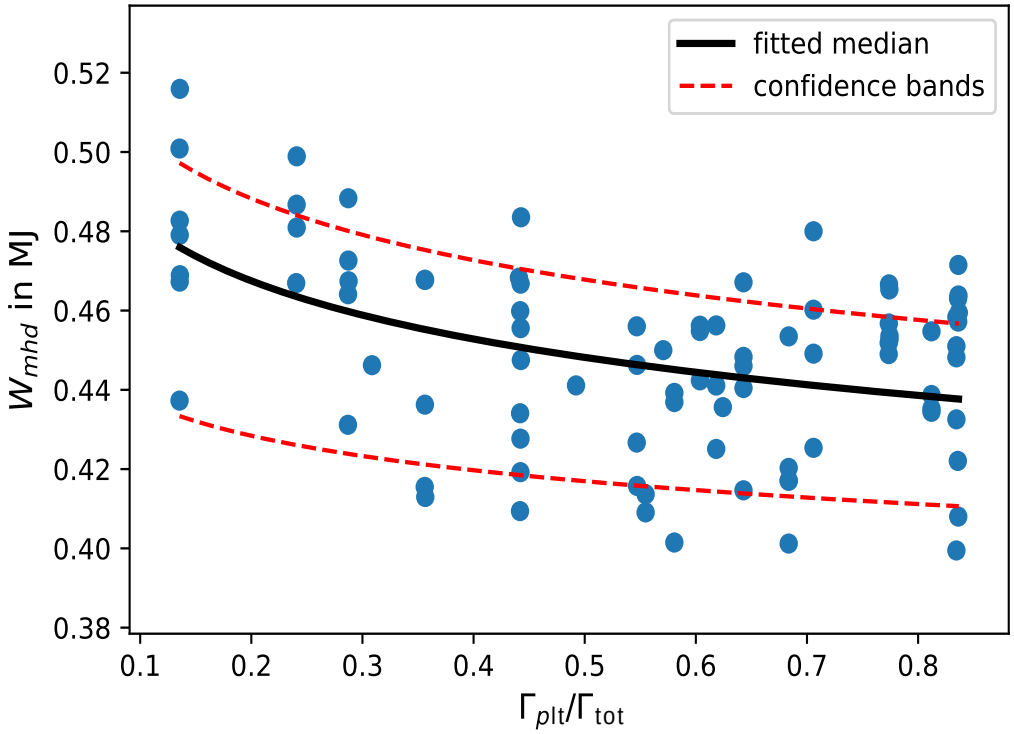

Figure 26: W_{mhd} as a function of the normalized pellet flux

Figure 26 depicts the total plasma energy W_{mhd} as a function of $\frac{\Gamma_{plt}}{\Gamma_{tot}}$. Contrary to expectations, the fitted median of W_{mhd} decreases by $\approx$ 8 %, when pellet fuelling aggregates 85 % of the total particle flux, compared to gas-puff only. An analysis of this phenomenon is provided in Chapter 5.3.4.

5.2.2 Technical particle confinement time $\tau_{p,tech}$

As elaborated in Chapter 5.2, a rise in the particle content of the core plasma (while the share in pellet flux rises), implies an increase in the particle confinement time of the confinement region τ_c. Since this value is hard to obtain, the technical particle confinement time $\tau_{p,tech}$ will be further considered. The technical particle confinement time can be defined as:

$$\tau_{p,tech} = \frac{N_e}{\Gamma_{tot}} = \frac{\int_V n_e(\rho)\, dV}{\Gamma_{tot}} \tag{54}$$

where N_e is the electron inventory within the last close flux surface (LCFS). In order to obtain N_e, a volume integral over the electron density profile is required. For how the volume integrals have been performed, see Appendix.

By assuming that the change in $\tau_{p,tech}$ is dominated by the change in τ_c, it holds up that $\partial\tau_{p,tech} \approx \partial\tau_c$. Hence, $\tau_c \approx \tau_{p,tech}$ + const., which means that the technical particle confinement time is representative for τ_c.
Figure 27 depicts the technical particle confinement time as a function of the normalized pellet flux.

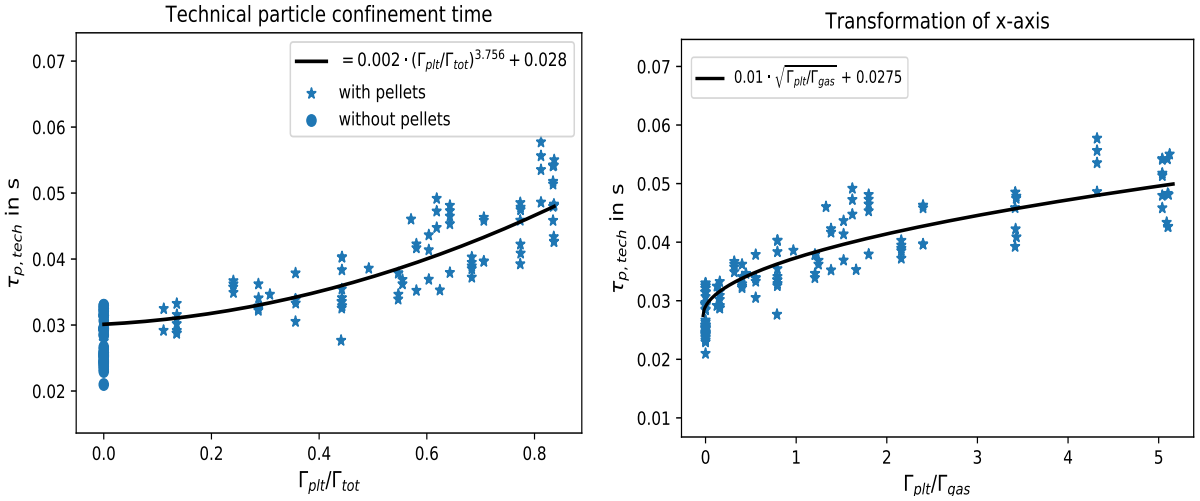

Figure 27: $\tau_{p,tech}$ as a function of $\Gamma_{plt}/\Gamma_{tot}$ (left) and $\Gamma_{plt}/\Gamma_{gas}$ (right)

As expected, figure 27 (left) depicts a rising trend of $\tau_{p,tech}$. Since the total particle flux Γ_{tot} was kept virtually constant, this is equivalent to an increase in the plasma electron content N_e. Furthermore, a rise in $\tau_{p,tech}$ is desirable, since it diminishes the demand in tritium in future fusion reactors. The fit in figure 27 (left) was obtained by performing and ordinary least square fit, since an odds transformation (right) did not result in a linear model. For additional information on odds transformations, see Appendix.

Lastly, some emphasis should be put on the reactor relevance of the particle con-

finement time $\tau_{p,tech}$. As for that, it is important to note that, keeping the tritium inventory as low as achievable possible will be one of the key tasks in a future reactor. One of two needed quantities will therefore be a particle confinement time which makes up the balance between stored particles (electrons) in the plasma N_e and the overall particle-influx Γ_{tot}, as defined in equation 54. The second required quantity will be a burnup-fraction which makes up the balance between the particles which burn in the core plasma and the particles which are recycled back into the plasma.

5.3 Explanatory- and modeling approaches

While this chapter mainly focuses on providing possible models for the supra-linear increase in core density $n_{e,core}$, it also makes findings on the slight decrease in W_{mhd} when the share in pellet flux is increased.

5.3.1 Linear model

In first approximation, a linear diffusive model could be considered [64], where the core density n_{core} is simply the sum of contributions from gas-puff and pellet fuelling. Furthermore, a particle density can be rewritten as $n = \frac{N}{V} = \Gamma \cdot \frac{\tau}{V}$.

$$n_{core} = n_{plt,core} + n_{gas,core} = \Gamma_{plt}\frac{\tau_{plt}}{V_{plt}} + \Gamma_{gas}\frac{\tau_{gas}}{V_{gas}} \tag{55}$$

Here, Γ is the particle flux, τ the particle confinement time and V the deposition profile of the two particle sources respectively. It is assumed, that the quotients $\frac{\tau_{plt}}{V_{plt}}$ and $\frac{\tau_{gas}}{V_{gas}}$ only depend on the spatial distribution of diffusiveness, but not on the magnitude of the respective source. Thereby, the quotients are assumed to be constants. With the introduction of the peak density $f_p = \frac{\Gamma_{plt}}{\Gamma_{tot}}$, equation 55 can be rewritten as:

$$n_{core} = (\Gamma_{plt} + \Gamma_{gas}) \cdot \frac{\tau_{gas}}{V_{gas}} \cdot \left(1 + f_p \cdot \left(\frac{\tau_{plt}/V_{gas}}{\tau_{gas}/V_{plt}} - 1\right)\right) \tag{56}$$

When considering equation 56, the core density n_{core} would be expected to increase in a linear fashion. Since the experimental results deviate significantly from this trend, it is indicated that a model which only considers diffusion might be insufficient. Fur-

thermore, the quotients, which have been assumed to be constants, might also not remain constants, when the peak density f_p is varied. The quotients $\frac{\tau_{plt}}{V_{plt}}$ and $\frac{\tau_{gas}}{V_{gas}}$ not being constants would be equivalent to a change in transport properties.

5.3.2 Pellet penetration depth model

Next up, an extension to the linear diffusive model is being made. As for that, the pellet deposition depth has to be considered [64]. The higher the share in pellet flux gets, the more the plasma is being cooled down (figure 25) to due pellets having a temperature of $\approx$ 12 K [65]. Therefore, the pellets can penetrate deeper since their ablation is delayed. Hence, is is observed, whether the deeper pellet penetration is responsible for the non-linear increase in core density $n_{e,core}$.

Here, also a pure diffusive model is being assumed for radii smaller than the radius of the pedestal top. Moreover, it is assumed that a pellet can be assumed as a delta function (with a finite peak), which is completely deposited at a radius ρ_{plt}. This means that the density profile builds up from the pedestal top to the radius of pellet deposition. By then performing an integration over a cylindrical geometry, the core density is given by:

$$n_{core} = n_{pedestal} \cdot \left(1 + \alpha \cdot f_p \cdot ln\left(\frac{\rho_{pedestal}}{\rho_{plt}}\right)\right) \tag{57}$$

where α can either be fitted to the experimental set or given in a model of two diffusion coefficients as:

$$\alpha = \frac{D_{edge}}{D_{core}} \frac{a}{d_{gas}} \left(1 - \frac{n_{seperatrix} \cdot D_{edge}}{\Gamma_p + \Gamma_g}\right) \tag{58}$$

Here, D refers to a diffusion coefficient, d_{gas} to the deposition depth of the gas-puff, a the small plasma radius and $n_{separatrix}$ the density at ρ_{pol} = 1. Since several parameters are expected to be constant, α has been fitted to the underlying dataset. The results predicted by equation 57 are shown in figure 28.

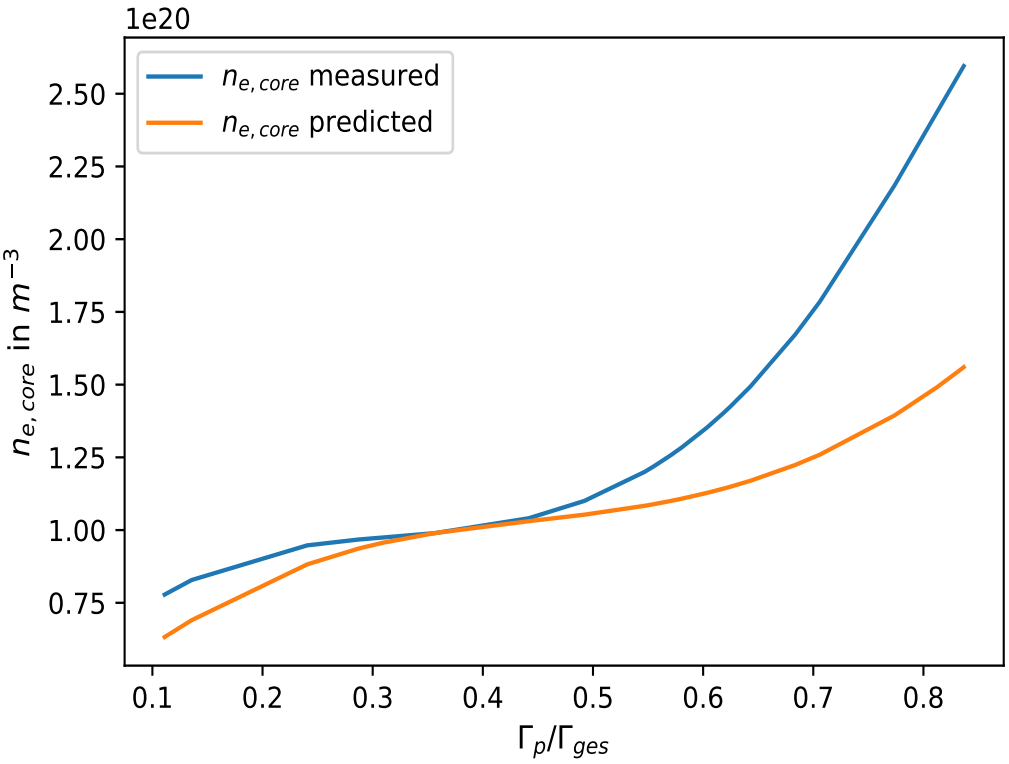

Figure 28: Comparison of predicted values and measured values for n_{core}

Up to a peak density of $f_p \approx 0.6$, the measured values (blue solid line) are represented by equation 57 (orange solid line) quite well. However, beyond this value, equation 57 underestimates the increase in core density which indicates that α cannot be treated as a constant. This in turn implies that certain terms in equation 58 might not be constant. Therefore, if α is treated as a function of the peak density f_p, like:

$$\alpha = b \cdot f_p^{0.725} \tag{59}$$

with b being a constant that can be fitted to the dataset. For this specific statistical approach, equation 57 can be rewritten as:

$$n_{core} = n_{pedestal} \cdot \left(1 + b \cdot f_p^{1.725} \cdot ln\left(\frac{\rho_{pedestal}}{\rho_{plt}}\right)\right) \tag{60}$$

The values predicted by equation 60 (orange), compared to the measured values (blue) are shown in figure 29.

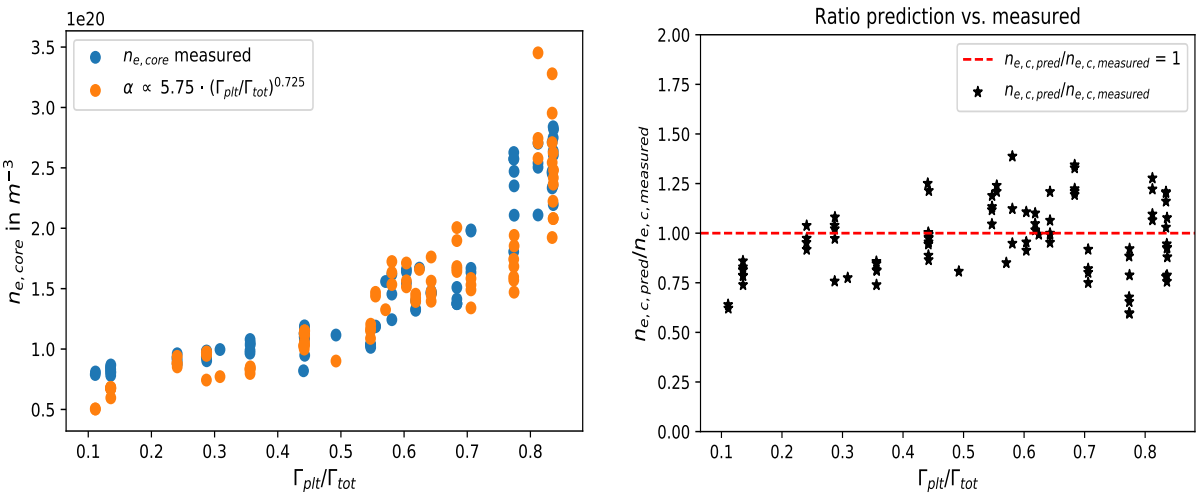

Figure 29: Comparison of predicted values and measured values for n_0, treating α as a function of f_p

Figure 29 (left) depicts that with α being a function of the peak density f_p, the dataset can be fitted. Furthermore, figure 29 (right) illustrates, that the ratio of predicted and measured values for $n_{e,core}$, scatters approximately constant around one, when the peak density is being varied. However, treating α as a function of f_p is a solely statistical approach and signals that a change in transport properties (parameters of α) seems likely.

5.3.3 Collisionality dominated diffusive peaking model

When reconsidering equation 58, it seems likely, that the diffusion coefficient D_{core} is not constant, due to high collisionality in the pellet fuelled plasma. Therefore, a very simple model is derived which parametrizes the peaking of the electron density profile as a function of the particle source produced by pellets, the corresponding radial position of the particle deposition, and the (turbulent) electron diffusion coefficient, in combination with the electron density at the pedestal top [66]. It is assumed that, given the high collisionality of the pellet fuelled plasmas, particle transport is characterized by diffusion only, without any convection. The Ware pinch [67] is also neglected. Thereby, it is assumed that in the absence of a particle source, that is with particle flux equal to zero, the density profile is flat. For simplicity, the density peaking is described as the ratio of the central density to the density at a peripheral position,

that shall be considered to simply be the pedestal top, at radius ρ_{ped} . The location of the pellet deposition is ρ_{plt} , where ρ is a flux surface minor radius in meters (can be considered as the toroidal minor radius). A condition is considered, in which the pellet repetition period (time between two consecutive pellet injections) is short compared to the density profile relaxation time. In this specific case, the electron density profile can build up as a consequence of the localized particle source provided by the train of pellet injections, and the effect of the pellet source can be considered to be given by a time-averaged amount of particles per second Γ_{plt}, in electrons per second, where Γ_{plt} = $\int S_{plt}\, dV$, with S_{plt} being the particle source density, which, in a first approximation, can be considered to be a delta function at the ρ_{plt} radial position. When a stationary condition is reached, in which the density profile builds up a density gradient in the region where a particle flux produced by the pellet source is present, the continuity (particle balance) equation reads as:

$$S_{plt} = -\frac{1}{V'}\frac{\partial}{\partial\rho}V'(\rho)\cdot D\frac{\partial n}{\partial r} \tag{61}$$

Here, V' is the radial derivative of the Volume and D is an electron diffusion coefficient which is assumed is assumed to be constant within $0 < \rho < \rho_{ped}$. By performing a volume integral on both sides of equation 61 and separating the radial domains inside ($\rho < \rho_{plt}$) and outside ($\rho \geq \rho_{plt}$) the pellet location ρ_{plt}, leads to:

$$-V'(\rho)\cdot D\frac{\partial n}{\partial r} = 0 \quad \text{for} \quad 0 < \rho < \rho_{plt} \tag{62}$$

and

$$-V'(\rho)\cdot D\frac{\partial n}{\partial r} = \Gamma_{plt} \quad \text{for} \quad \rho_{plt} < \rho < \rho_{ped} \tag{63}$$

The solution of equation 62 is simply $\frac{\partial n_e}{\partial \rho}$ = 0. Therefore integrating with assuming continuity at the boundary delivers:

$$n_e(\rho = [0\ \rho_{plt}]) = n_e(\rho_{plt}) \tag{64}$$

which,in particular, directly provides the value of the central density as equal to that of the density at the pellet deposition location ρ_{plt}. The density at the pellet deposition location can be obtained by the solution of equation 63, which is

$$n_e(\rho = [\rho_{plt} : \rho_{ped}]) = -\int_{\rho_{ped}}^{\rho} \frac{\Gamma_{plt}}{V'(\rho) \cdot D} d\rho \tag{65}$$

which can be easily integrated using a constant diffusion coefficient (or more precisely a constant $V' \langle(\nabla\rho)^2\rangle \mathcal{D}$), delivering a linear density profile

$$n_e\left(\rho = [\rho_{\mathrm{plt}}\rho_{\mathrm{ped}}]\right) = \frac{\Gamma_{\mathrm{plt}}}{2\pi^2 R\mathcal{D}} \frac{\rho_{\mathrm{ped}} - \rho}{\rho_{\mathrm{ped}} + \rho_{\mathrm{plt}}} + n_e(\rho_{ped}) \tag{66}$$

Here, a simplified description of the geometry is assumed. Furthermore, taking the surface geometrical factor $V' \langle(\nabla\rho)^2\rangle$ as equal to $4\pi^2 R\rho$, with R being the major radius, and considering the value of ρ at the middle of the integration box, which is $\rho = \left(\rho_{\mathrm{plt}} + \rho_{\mathrm{ped}}\right)/2$. Then, the electron density peaking factor is simply given by:

$$\frac{n_{e,core}}{n_{e,ped}} = 1 + \frac{\Gamma_{plt}}{2\pi^2 R D n_{e,ped}} \frac{\rho_{ped} - \rho_{plt}}{\rho_{ped} + \rho_{plt}} \tag{67}$$

The resulting density profile inside and outside the pellet deposition radius ρ_{plt} of equations 64 and 66 is shown in figure 30.

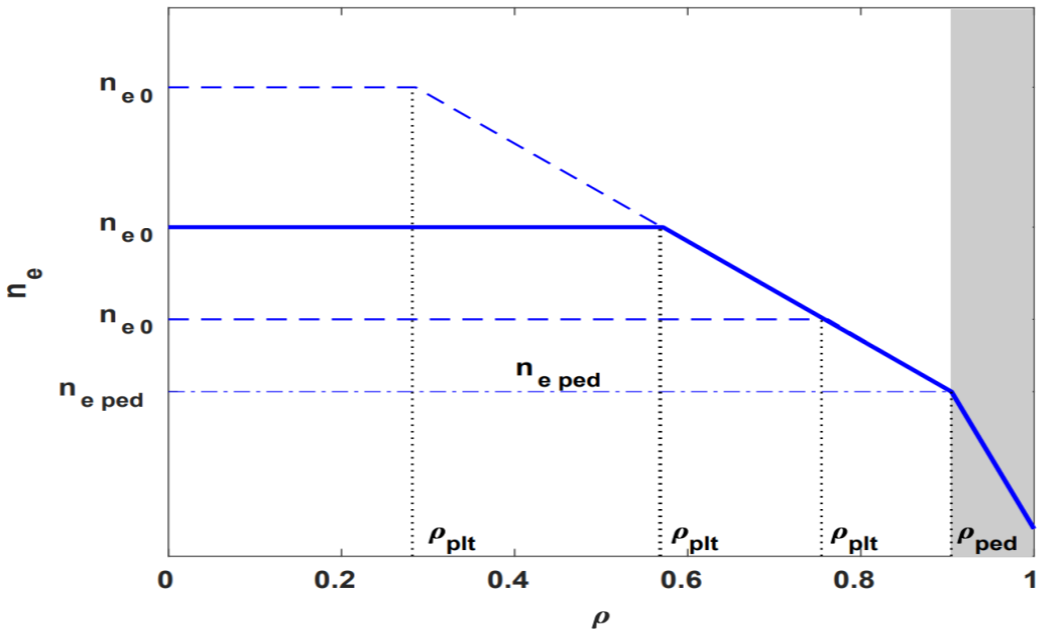

Figure 30: Construction of the density profile, using a diffusion only transport model [66]

Figure 30 depicts that deeper pellet penetration leads to a higher core density (equation 64), since the same amount of particles are deposited at a radius whose volume element is smaller. Figure 31 portrays the change in pellet penetration depth as a function of the peak density $f_p = \frac{\Gamma_{plt}}{\Gamma_{tot}}$.

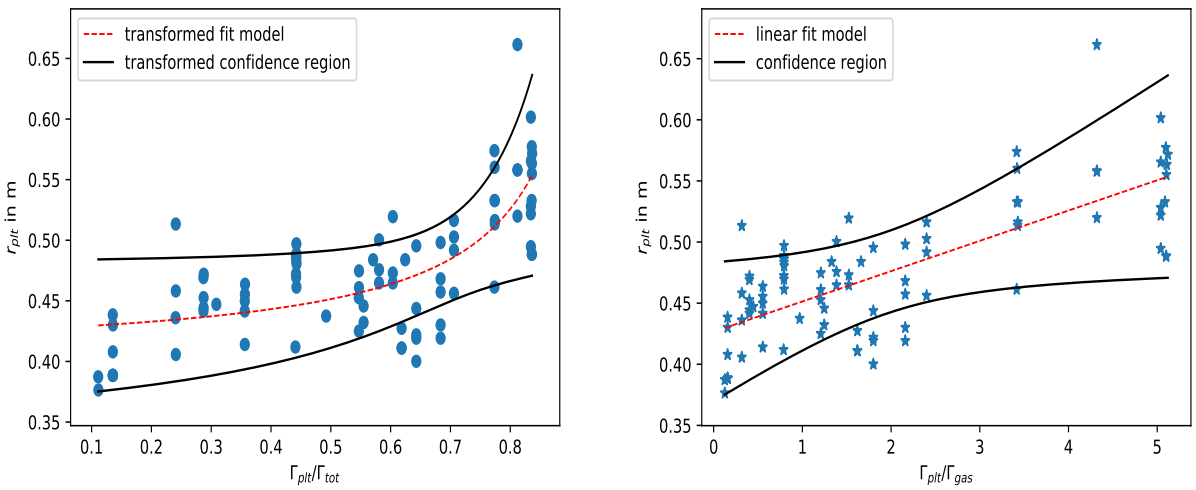

Figure 31: Pellet penetration depth as a function of $\Gamma_{plt}/\Gamma_{gas}$ (left) and $\Gamma_{plt}/\Gamma_{tot}$ (right)

Figure 31 (left) represents the variation in pellet penetration depth as a function of f_p. The OLS fit, as well as the 90 % local confidence band were obtained by performing an odds-transformation of $\Gamma_{plt}/\Gamma_{tot}$ which led to a linear model.

So far, equation 67 and 57 are equivalent diffusive models with constant diffusion coefficients. However, in the presence of a centrally peaked density profile (negative $\frac{\partial n_e}{\partial \rho}$) at high collisionality ,the turbulent diffusion coefficient is expected to decrease with rising collisionality [5]. Therefore, also including a Bohm or gyro-Bohm scaling [68], a simple parametrization of $\mathcal{D}$ is expected in the form of $\mathcal{D} \propto T_e^{\beta} \nu_e^{-\alpha}$, with both α and β being positive exponents. By assuming constant pressure ($T_e \propto n_e^{-1}$). The electron collisionality should be expressed like $\nu_e \propto Z_{eff} \cdot R \cdot n_e^3$. However, since Z_{eff} is close to one and R is also approximately constant only n_e^3 is further considered. The exponent β is chosen between 1 (Bohm) and $\frac{3}{2}$ (Gyro Bohm) which leads to a parametrization of $\mathcal{D}$:

$$\mathcal{D} = D \left(\frac{\bar{n}_e}{n_{\text{eped}}} \right)^{-1.(5)-3\alpha} \tag{68}$$

Consistent with the approach of replacing ρ by $\frac{\rho_{plt}+\rho_{ped}}{2}$, $\overline{n_e}$ is also chosen to be in the middle of the integration box and can therefore be replaced by:

$$\overline{n_e} = n_{e,ped} + \frac{n_{e,ped} + n_{e,core}}{2} \tag{69}$$

Combining equations 67, 68 and 69 leads to the sought final result which can be directly compared with the experimental data in order to obtain values of D and α which best fit the experimental behaviour.

$$\frac{n_{e,c}}{n_{e,ped}} = 1 + \frac{[(1 + n_{e,core}/n_{e,ped})/2]^{3\alpha+1.(5)}}{D} \frac{\Gamma_{plt}}{2\pi^2 R n_{e,ped}} \frac{\rho_{ped} - \rho_{plt}}{\rho_{ped} + \rho_{plt}} \tag{70}$$

Equation 70 introduces a clear non-linearity in the dependence of the peaking factor on the pellet fuelling rate Γ_{plt}, which can be solved iteratively. In a first attempt, one can remove the dependence on $n_{e,core}$ on the right hand side (equivalent to 3α + 1.(5) = 0), and check whether there is a value of D which allows one to fit all of the experimental data. It is noticed, that also in this case, equation 70 does not provide an exactly linear dependence of the density peaking as a function of Γ_{plt}, because with increasing Γ_{plt}, and thereby increasing density and decreasing temperature, also ρ_{plt} is

reduced (the penetration depth increases), which by itself leads to an increase of the central density. However, theoretical arguments would lead to the expectation that the limit of a constant D should not allow to perfectly fit the data. It is expected that the reduction of the diffusion coefficient produced by reduced temperature and increased collisionality with increasing density leads to a progressively increasing density peaking, stronger than the one which is only provided by the reduction of ρ_{plt} . An example of the results that can be obtained is presented in 32, by noticing that the ratio $\Gamma_{\rm plt}/(DRn_{\rm eped})$ is dimensionless.

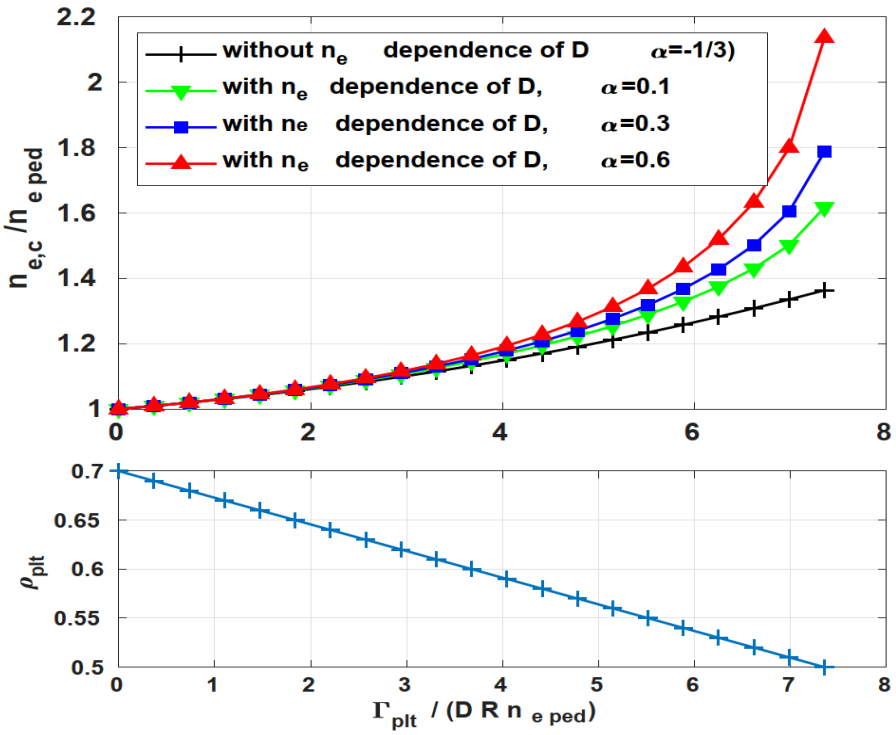

Figure 32: Predictions of the density peaking given by the model as a function of the dimensionless factor $\Gamma_{\rm plt}/(DRn_{\rm eped})$ (top), with and without the inclusion of the density dependence in the diffusion coefficient (and assuming Bohm transport, β = 1), for different values of α = 0.1, 0.3, 0.6, and considering ρ_{ped} = 0.9 and ρ_{plt} as plotted in the bottom plot [66].

After equation 70 had been solved iteratively, a multivariate regression analysis was carried out, using α and D as independent input variables for the cases of $\beta = 1$ (Bohm transport) and $\beta = 1.5$ (gyro-Bohm transport). The results are depicted in 3:

Table 3: Resluts for α and D'

β	α	D′
1.0	-0.04497	3.9872
1.5	-0.21163	3.9872

The best fit is given for a negative α which is contradictory to the expectation of figure 32. Before discussing possible reasons for that, it should be noted that by using equation 70, the measured results for $n_{e,core}$ can now be fitted as depicted in figure 33.

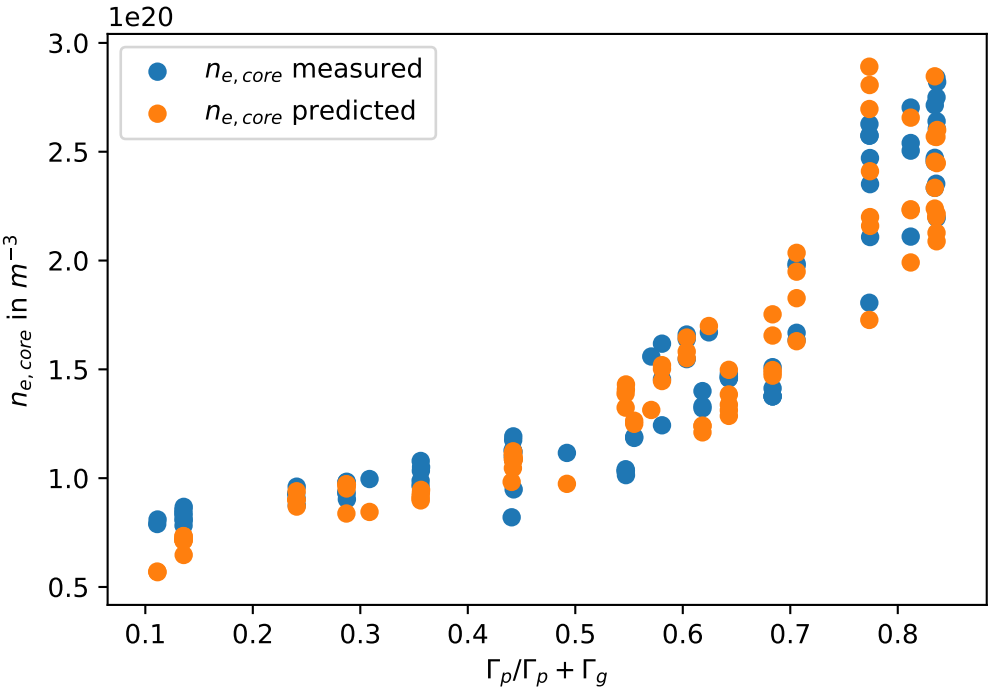

Figure 33: Comparison of measured data (blue) and predicted data (orange) by eq. (68) for core electron densities

Figure 33 shows that by including a Bohm transport scaling to a diffusive model, the experimental data can be fitted perfectly. To observe why α has been chosen negatively, fixed values for the diffusion coefficient D can be selected, as illustrated in figure 34.

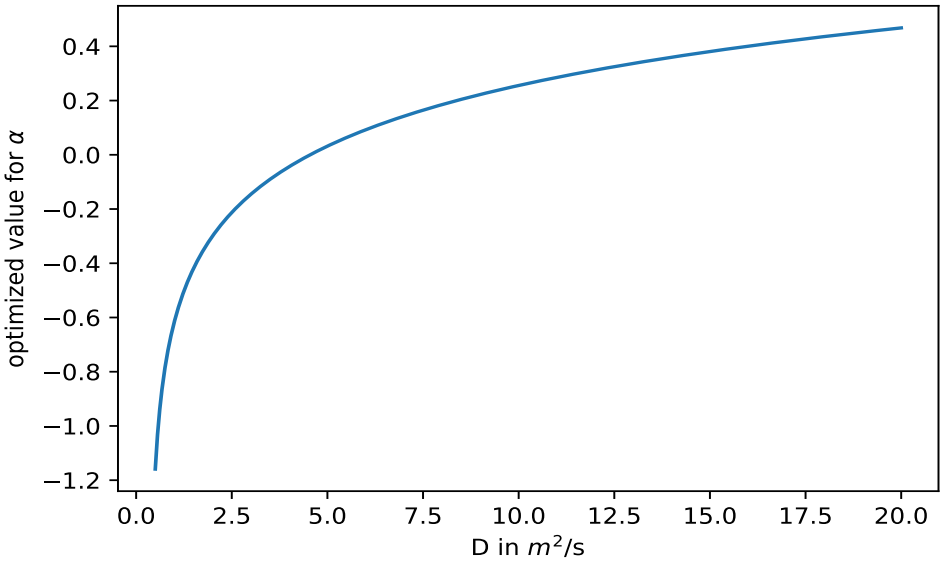

Figure 34: Response of α when varying D

Figure 34 clearly shows that positive values for α can be achieved if the diffusion coefficient is increased. However this means that the error for the estimation of α increases. Therefore the error of α is observed as a function of the diffusion coefficient, using the data from the covariance matrix of α.

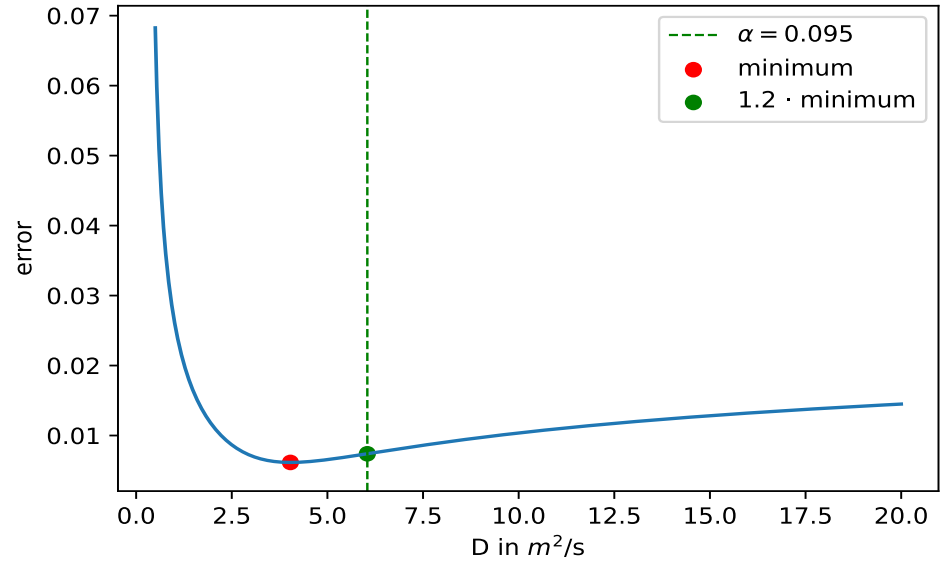

Figure 35: Error of α when varying D

Figure 35 depicts that when accepting an error of 20 %, α would reach a value of $\approx$

0.1, which does make this statistical approach for increasing α not suitable.

Therefore, figure 32 (bottom) has to be reconsidered, where a linear decrease in ρ_{plt} and therefore a linear increase in pellet deposition depth is assumed for the prediction. However, when considering figure 31 a clear supar-linear increase is shown which explains the fact that a smaller α is needed to fit the data.

5.3.4 Decrease in W_{mhd}

The primary incentive for this subsection has been the results of figures 24, 25 and 26. Despite the core pressure rising, a decrease of ≈ 8 % in W_{mhd} has been perceived when raising the share in pellet flux from 0 % to 85 %. To further iterate, profiles for pressure, density and temperature should be considered.

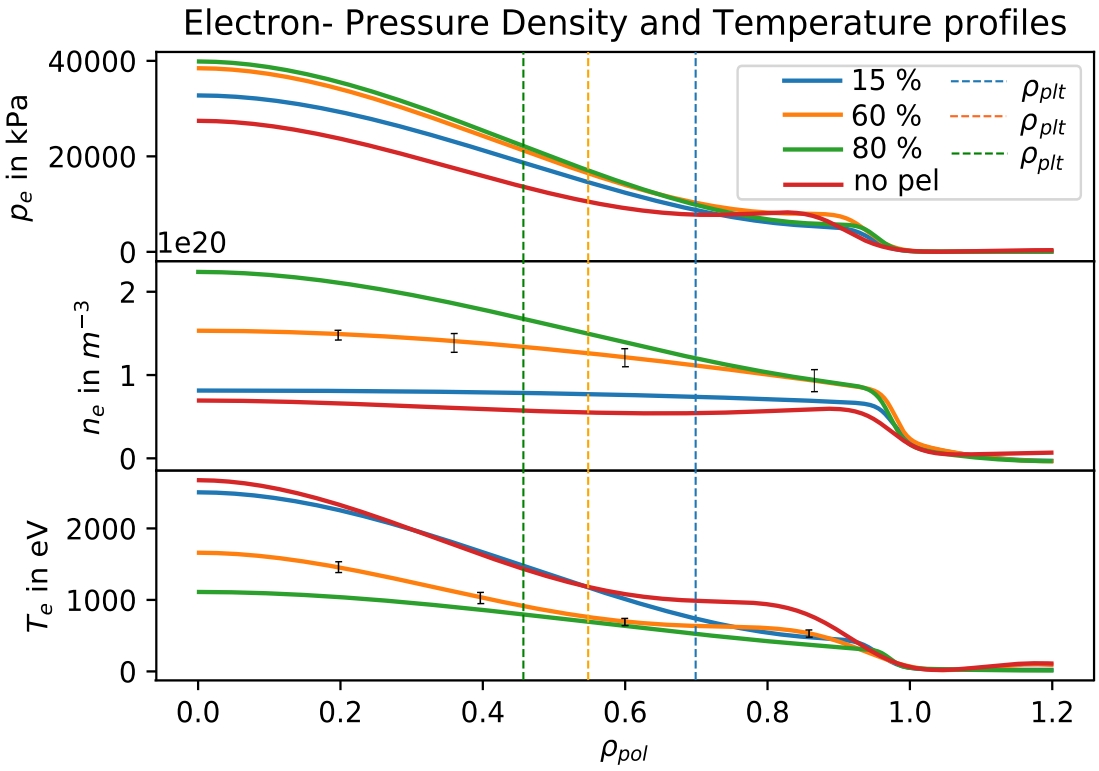

Figure 36: Electron pressure-, density- and temperature- profiles

Figure 36 depicts electron pressure-, density- and temperature profiles, obtained from Thomson Scattering for different shares in pellet flux. Furthermore, the dotted

lines represent the position of pellet deposition ρ_{plt}. As expected and previously observed in ref. [69], a clear peaking of the pressure profiles towards the core with rising share in pellet flux is perceived. Therefore, W_{mhd} decreasing is unanticipated.

To observe this phenomenom, it should be considered what terms W_{mhd} is made up of:

$$W_{mhd} = W_{th,e} + W_{th,i} + W_{fi} \tag{71}$$

Here, W_{th} refers to the kinetic plasma energy and W_{fi} represents the energy of fast particles. Equation 71 can be rewritten as:

$$W_{mhd} = \int_V n_e(\rho) \cdot T_e(\rho)\, dV + \int_V n_i(\rho) \cdot T_i(\rho)\, dV + W_{fi} \tag{72}$$

Since the ion density n_i is hard to obtain, n_i can be expressed, using $\bar{Z}$ from equation 28:

$$W_{mhd} = \int_V n_e(\rho) \cdot T_e(\rho)\, dV + \frac{1}{\bar{Z}} \int_V n_e(\rho) \cdot T_i(\rho)\, dV + W_{fi} \tag{73}$$

Assuming impurities to be negligible, equation 34 can be used, to rewrite equation 73 as:

$$W_{mhd} = \int_V n_e(\rho) \cdot T_e(\rho)\, dV + \int_V n_e(\rho) \cdot Z_{eff}(\rho) \cdot T_i(\rho)\, dV + W_{fi} \tag{74}$$

When considering equation 74 there are two scenarios which could explain the slight decrease in W_{mhd} with rising share in pellet flux. Firstly, the decrease might arise from W_{th} decreasing due to the plasma edge being weighted higher in the volume integration. Secondly, the the decline in W_{mhd} could also issue from the fast particles being slowed down due to a higher density in a pellet fuelled plasma [1]. While W_{fi} is hard to obtain during pellet injection phases, W_{fi} contributes to approximately 20 % of W_{mhd} before pellet injection. Therefore, if it is shown that W_{th} rises when $\frac{\Gamma_{plt}}{\Gamma_{tot}}$ is increased, it would be an indirect proof that the decrease in W_{mhd} is caused by a loss

in fast particle energy W_{fi}.

When considering equation 74, it is evident that two volume integrations are required, in order to determine the kinetic plasma energy W_{th}. For how the integrations have been carried out, see Appendix. For the n_e-, T_e- and Z_{eff}- profiles, data from Integrated data analysis (IDA) has been used. As for the ion temperature profiles, Charge exchange recombination spectroscopy (CXRS) and lithium beam (edge) data has been used to fit profiles with a -tanh fit. Figure 37 shows the results of this analysis.

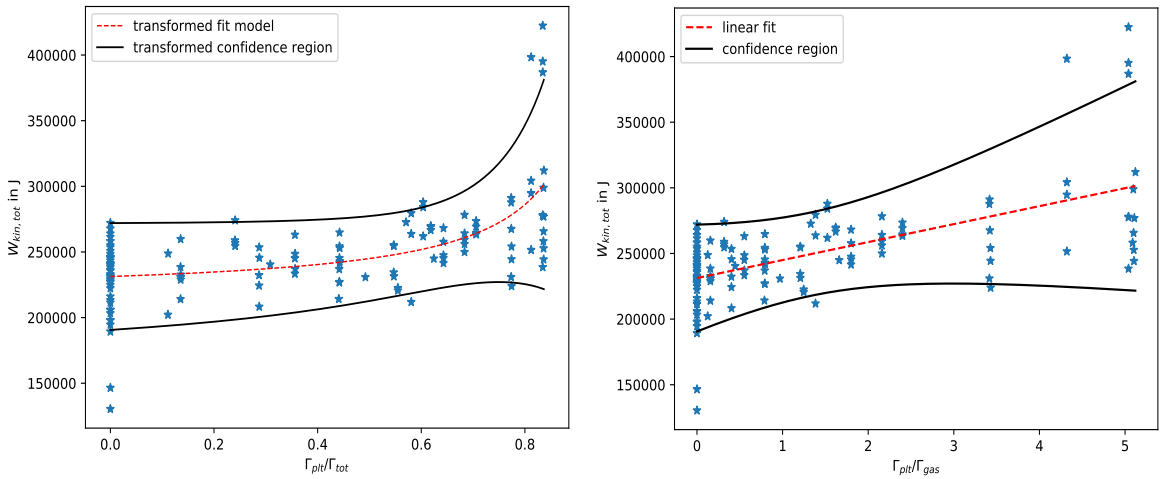

Figure 37: Total kinetic energy W_{th} as a function of $\frac{\Gamma_{plt}}{\Gamma_{tot}}$ (left) and an odds transformation leading to a linear model (right)

Figure 37 (left) shows a non-linear rising trend for W_{th} as a function of $\frac{\Gamma_{plt}}{\Gamma_{tot}}$. When increasing the share in pellet flux from 0 % to 85 %, the fit model expects an increase of $\approx$ 12 % in W_{th}. This result is congruent with the assumption of the fast particles being approximately slowed down entirely. If 20 % of W_{mhd} gets lost due to a deceleration of fast particles, then an increase of 12 % in W_{th} explains the remaining 8 % loss in W_{mhd} (figure 26).

It should be noted, that by solely considering the thermal energy of the electrons $W_{th,e}$, the fit model predicts and increase of approximately 18 %, when the share in pellet flux is increased from 0 % to 85 %. Since for the analysis of figure 37, data from different diagnostics has been mingled and no impurities were assumed, the value of 12 % should be considered as a lower boundary, which might rise to approximately 20

%.

As an overview, a plot is given in figure 38, depicting the trends of W_{mhd} (blue), W_{th} (orange) and their difference W_{fast} (which is a measure for W_{fi} (red)).

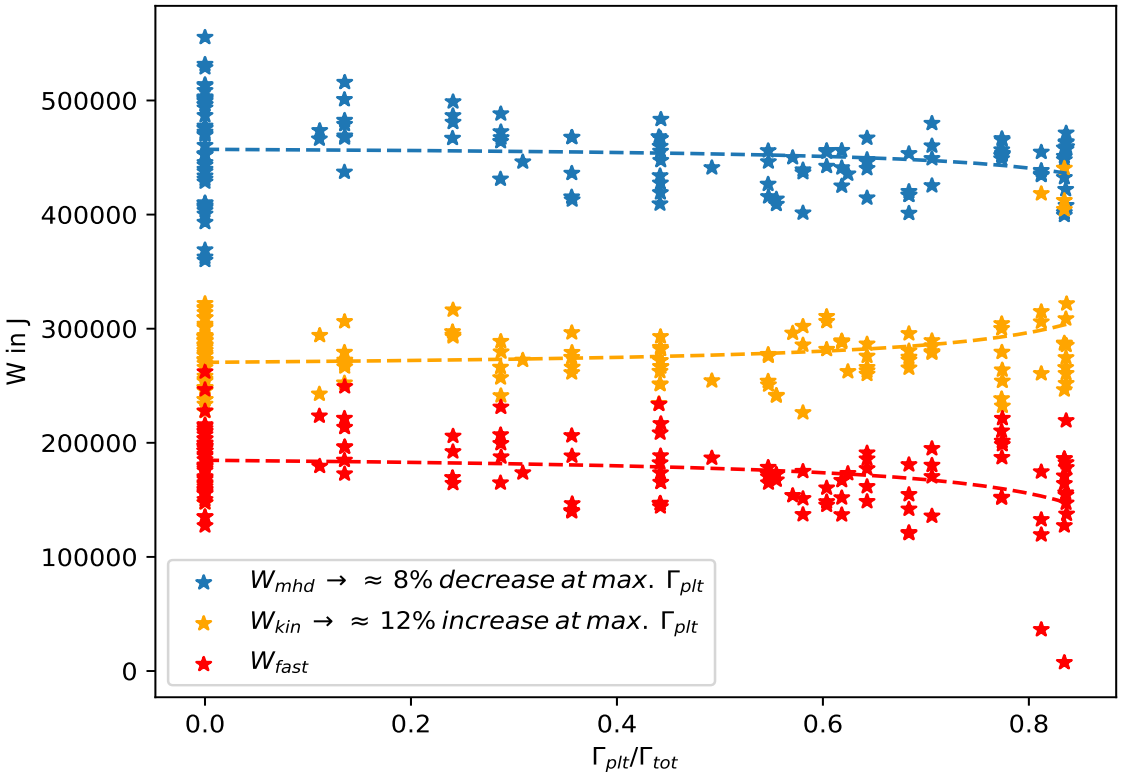

Figure 38: W_{mhd}, W_{th} and $W_{fast} = W_{mhd} - W_{th}$ as a function of $\frac{\Gamma_{plt}}{\Gamma_{tot}}$

Overall, this trend is desirable for fusion reactor concepts, since the energy of fast particles W_{fi} will not be contributing to the neutron flux in a reactor [70].

Lastly, it should be observed, how $W_{fast} = W_{mhd} - W_{th}$, which is solely a measure for W_{fi} (since the exact values for W_{fi} are not available) decreases as a function of volume-averaged density $n_{e,vav}$, which can be defined as

$$n_{e,vav} = \frac{N_e}{V} = \frac{\int_V n_e(\rho)\, dV}{V} \tag{75}$$

where N_e is the electron inventory of the plasma (requires a volume integration over the density profile) and V the plasma volume. Figure 39 depicts W_{fast} as a function of the volume-averaged electron density.

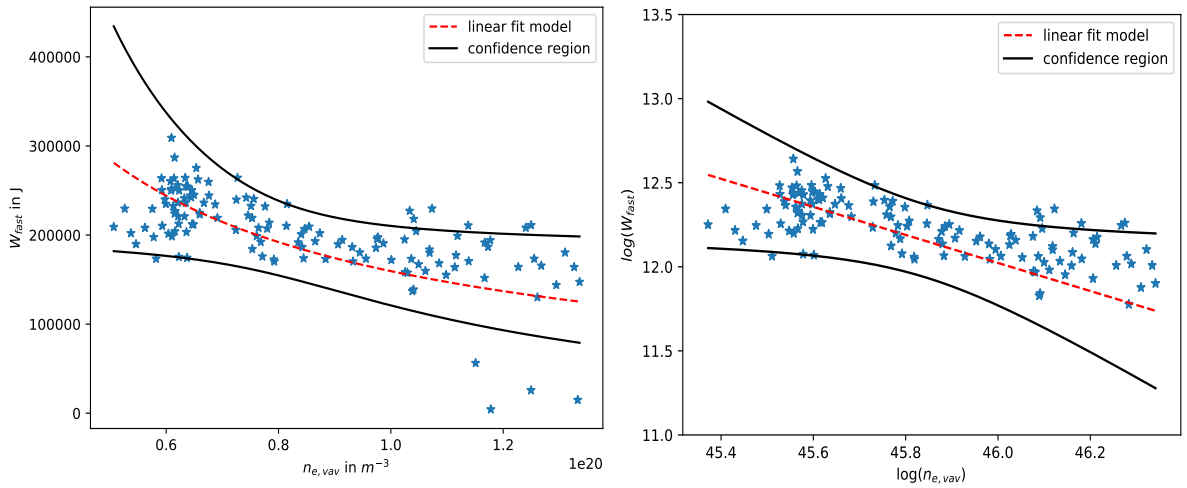

Figure 39: W_{fast} as a function of $n_{e,vav}$ (left) and logarithmic transformation (right)

The fit in figure 39 (left) was obtained by performing a logarithmic transforming both, the x- and y- axis, which led to a an approximately linear model (right). On logarithmic axes, a linear regression, as well as a local confidence region has been obtained. By transforming a linear model $f_{log-fit}(x)$ back to linear axes, the fit gets to:

$$f_{lin-fit}(x) = \exp\left(t_{log}\right) \cdot x^{m_{log}} \tag{76}$$

where m_{log} and t_{log} are coefficients of the linear regression on logarithmic axes. For the case of figure 39, a $W_{fast} \propto n_{e,vav}^{-0.85}$ dependency has been found. When considering figures 38 and 39 a stronger decrease in the energy of fast particles should be expected, since the slowing time τ_s of fast particles decreases like $\propto \frac{T_e^{3/2}}{n_e}$, assuming constant pressure this gets to $\tau_s \propto n_e^{-5/2}$ [71]. The deviation to this trend, is likely to be attributed to the assumptions, which have been made for the calculation of the thermal plasma energy of the ions $W_{th,i}$, as well as the merge of diagnostics for $W_{th,i}$. Furthermore, it was assumed that the energy of fast particles makes up approximately 20 % before of W_{mhd} before pellet injection. The value of 20 % however, solely considers fast particles from NBI, while fast particle energy from other heating methods is not taken into account. As a consequence, W_{fast} has to be considered as a measure for W_{fi}.

All things considered, the decrease in W_{mhd} can be attributed to the decrease in fast particle energy W_{fi} dominating the rise in thermal energy content W_{th}. The increase in W_{th} can be estimated to be 10-20 %.

5.4 Diffusion coefficients

In previous subsections, several formulas to predict the non-linear core density peaking, contained a diffusion coefficient D, e.g. equation 58 and 70. Equation 58 assumed constant diffusivity, while equation 70 treated the diffusion coefficient as a function of the temperature T and the collsionality ν. In both cases, however, the diffusion coefficient has been treated as a parameter which was either assumed to be constant, or fitted to the data set. Therefore, this section will focus on introducing two ways to define and determine diffusion coefficient, with the intention of further expanding the theory elaborated in the previous sections.

5.4.1 Effective diffusion coefficient D_{eff}

In an ideal gas, according to reference [18], a diffusion coefficient D can be defined using the mean free path L:

$$D = \frac{\tau_c v_{th}^2}{2} = \frac{L^2}{2\tau_c} \tag{77}$$

with v_{th} being the thermal velocity and τ_c the time between two collisions. However, this random walk expression is not suitable for describing hot plasma since it assumes classical transport. Therefore, instead of using the mean free path L and the collision time τ_c, other characteristic diffusion parameters can be chosen. As for that, the minor plasma radius **a** can be chosen as the diffusion length. Along with that, the techincal particle confinement time $\tau_{p,tech}$, defined in equation 54 can be selected, leading to an averaged diffusion coefficient D_{eff}. In other words, D_{eff} is a measure for how long particles are confined along a path which is the minor plasma radius. The effective diffusion coefficient is thereby given as:

$$D_{eff} = \frac{a^2}{2 \cdot \tau_{p,tech}} \tag{78}$$

Figure 40 depicts the values for D_{eff}, using equation 78 as a function fo the peak density $f_p = \frac{\Gamma_{plt}}{\Gamma_{tot}}$.

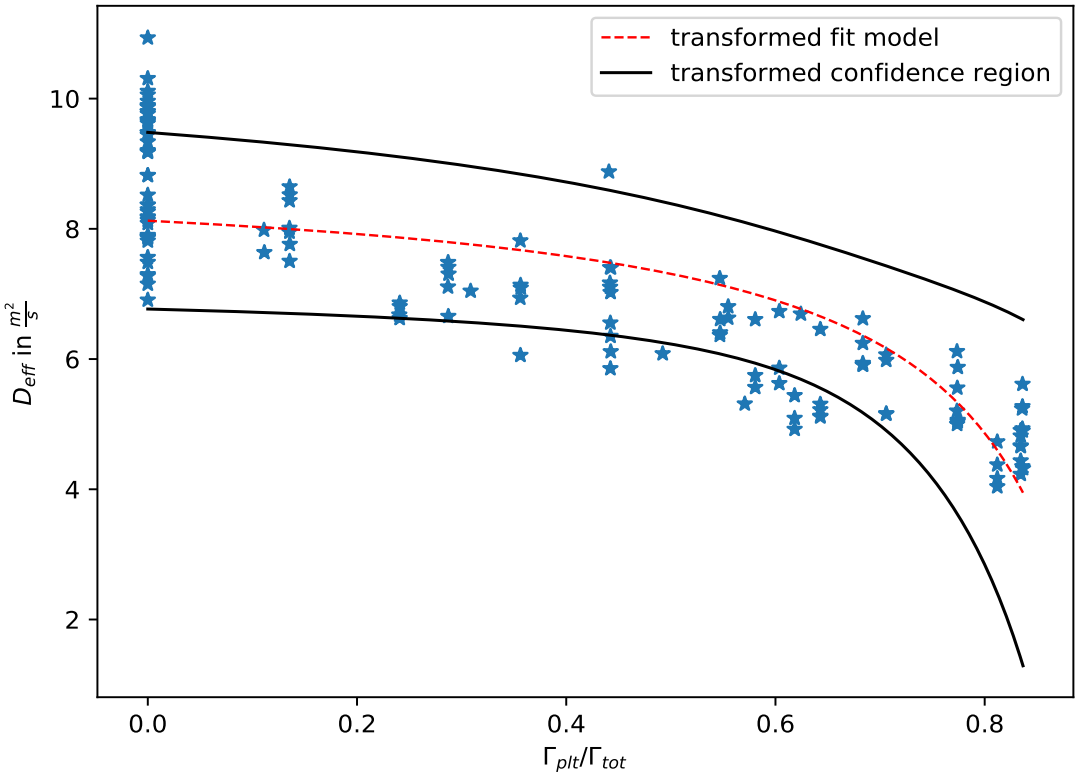

Figure 40: D_{eff} as a function of $\frac{\Gamma_{plt}}{\Gamma_{tot}}$. The fit (red dotted line) was obtained, performing an odds-transformation ($\frac{\Gamma_{plt}}{\Gamma_{tot}} \rightarrow \frac{\Gamma_{plt}}{\Gamma_{gas}}$) which led to a linear model for D_{eff}

When considering figure 27, an increase in $\tau_{p,tech}$ with rising f_p was shown. As a result, figure 40 shows a clear non-linear decrease in D_{eff} with rising pellet flux.

Within the collisionality dominated model to explain the density peaking of $n_{e,core}$, the diffusion coefficient has been expressed as a decreasing function of T and ν (equation 68). This means that, **D** within the equations 68 and 70 has to be considered as the diffusion coefficient at $\frac{\Gamma_{plt}}{\Gamma_{tot}} = 0$, since at this value, the the diffusion coefficient is the highest. Therefore, considering figure 40, D is approximately D $\approx$ 8.1. Treating this values as a constraint, and considering equation 70 and figure 34, a respective α can be

chosen. In this specific case, $\alpha \approx 0.2$ would be the result. This value for α is consistent with the initial expectation of α being a positive constant (compared to table 3, where alpha was chosen to be negative by the fit algorithm).

Lastly, an alternative to choosing the minor plasma radius as the diffusion length in equation 78 is outlined. As for that, the particle density n, given in particles per unit volume should be considered. By taking the densities inverse, one receives the volume per particle. If then, the third root of this value is taken, it can be considered as a measure for the mean free path. Since the density is given as a profile and equation 78 contains an averaged value ($\tau_{p,tech}$), the mean free path $L_{p,vav}$ has to be given as a volume-averaged value:

$$L_{p,vav} = \frac{\int\limits_V n_e(\rho)^{-1/3}\, dV}{\int\limits_V dV} \tag{79}$$

Using $L_{p,vav}$ as the diffusion length, equation 78 can be rewritten:

$$D_{eff,alt.} = \frac{L_{p,vav}^2}{2 \cdot \tau_{p,tech}} \tag{80}$$

Figure 41 depicts the results for equation 80 as a function of f_p.

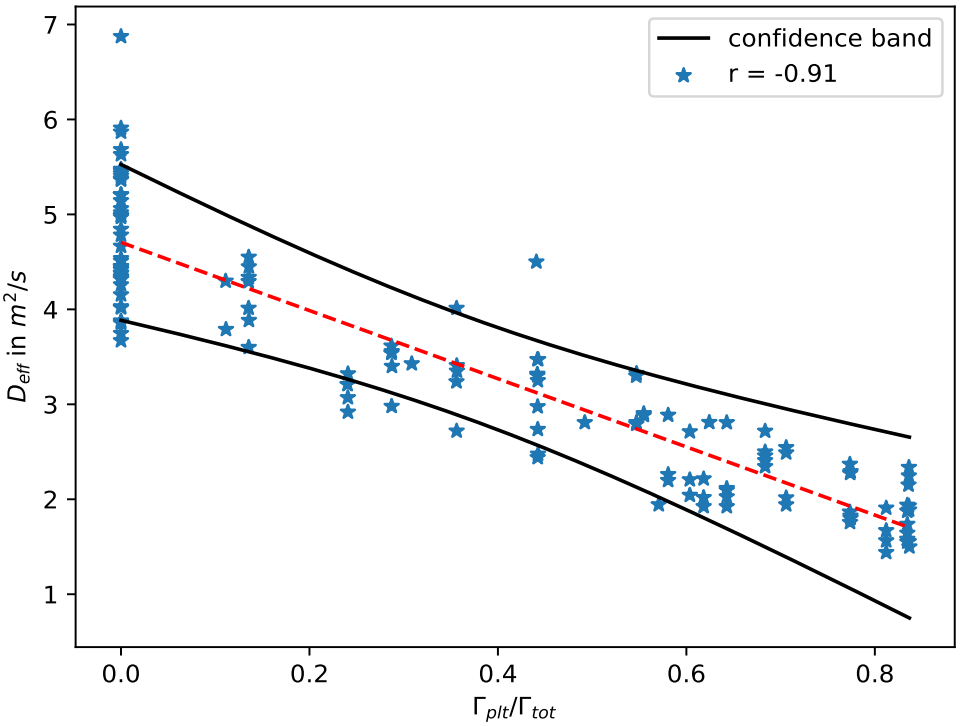

Figure 41: D_{eff} as a function of $\frac{\Gamma_{plt}}{\Gamma_{tot}}$

Comparing the trend of figure 40 to the one of figure 41, it can be seen that in figure 41, D_{eff} decreases in an approximately linear fashion. The trend in figure 40 shows a clear non-linearity which arises from the non-linear behaviour of $\tau_{p,tech}$ (sine **a** is a constant). The fact that D_{eff}, using the alternative definition (equation 80) only decreases linearly can be explained by the mean free path $L_{p,vav}$ decreasing with with rising pellet flux, since the overall plasma content builds up.

5.4.2 Local diffusion coefficient at pellet deposition

While the previous subsection was determined to introducing a method to defining an averaged plasma diffusion coefficient, this subsection will do contrary, since a method will be outlined, how a local diffusion coefficient can be defined. As for that, the behaviour of a (fringe-jump corrected) line-averaged density, whose sightline intersects the pellet penetration path, should be studied.

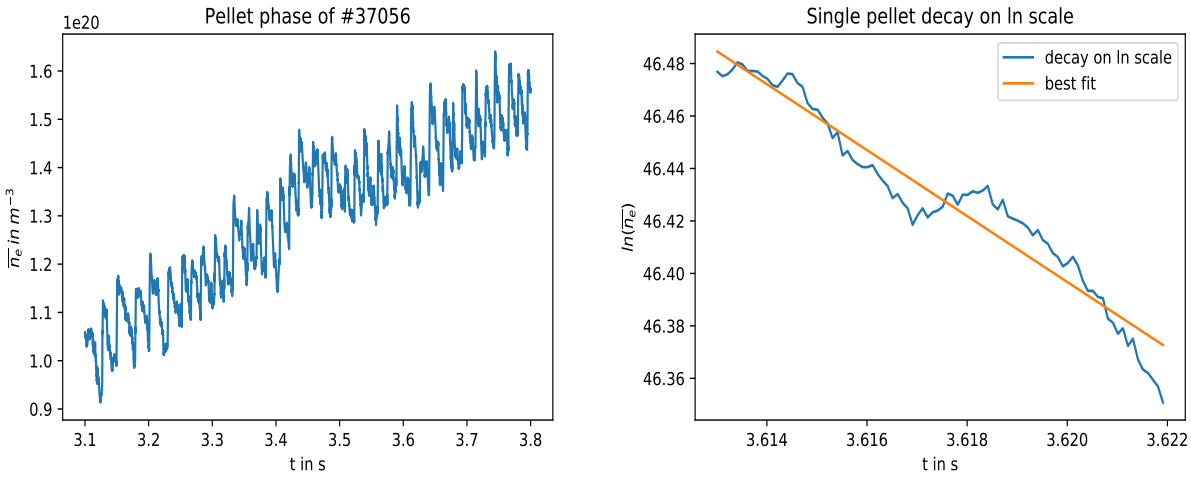

Figure 42: Density build up through pellets (left) and linear decay on ln scale of a single pellet (right)

Figure 42 depicts how a series of pellets can be perceived in the line averaged density $\overline{n_e}$ (obtained from DCN interferometry). Firstly, the increase in $\overline{n_e}$ by a pellet can be perceived as a Dirac delta function. Inducing a local density gradient, the pellet then starts to distribute which can also perceived in figure 42 (left). The decay can, in first approximation, be described by an exponential decay. The decay in density is then being interrupted by a new pellet being injected. Therefore, a series of pellets leads to the density building up. Figure 42 (right) shows the decay in density after a pellet got injected. It should be noted, that the y-axis has been transformed logarithmically, which led to an approximately linear decrease. By observing the decay behaviour of the pellet, one can therefore derive information regarding the transport within a local range of pellet deposition ρ_{plt}.

To quantify this behaviour, the disturbed particle confinement time $\tau_{p,dist}$ (disturbed due to pellet injection) will be introduced. Considering a single pellet within a series of pellet injections, the net gain in density by this pellet is $\Delta\overline{n_e}$ = $\overline{n_e}(t_{post,plt})$ - $\overline{n_{e0}}$, describing the difference in density before the next pellet gets injected and the density during gas-puff only. Assuming an exponential decay of this pellet, this leads to:

$$\Delta\overline{n_e} = \overline{n_e}(t_{plt}) \cdot e^{-\frac{t_{post,plt}-t_{plt}}{\tau_{p,dist}}} \tag{81}$$

where t_{plt} describes the time-stamp, at which $\overline{n_e}$ shows a transient due to the injected pellet. The time-stamp $t_{post,plt}$ refers to the time-stamp, immediate before the next pellet gets injected. The disturbed particle confinement time $\tau_{p,dist}$ can be perceived as the inverse slope of the straight line in figure 42 (right). To obtain $\tau_{p,dist}$, equation 81 can be rewritten as:

$$\tau_{p,dist} = \frac{t_{plt} - t_{post,plt}}{\ln\left(\frac{\overline{n_e}(t_{post,plt}) - \overline{n_{e,0}}}{\overline{n_e}(t_{plt})}\right)} \tag{82}$$

Analogous to equation 78, the disturbed particle confinement time $\tau_{p,dist}$ can now be used to define a diffusion coefficient. In this specific case, however, it should be noted that the resulting diffusion coefficient $D(\rho_{plt})$ is a local quantity, which therefore also requires a local diffusion length L_{dif}. In the strict sense, a pellet is neither a Delta dirac function, nor is it deposited solely at a radial position ρ_{plt}. Therefore, pellet deposition density profiles should be considered. Figure 43 shows a typical pellet deposition profile.

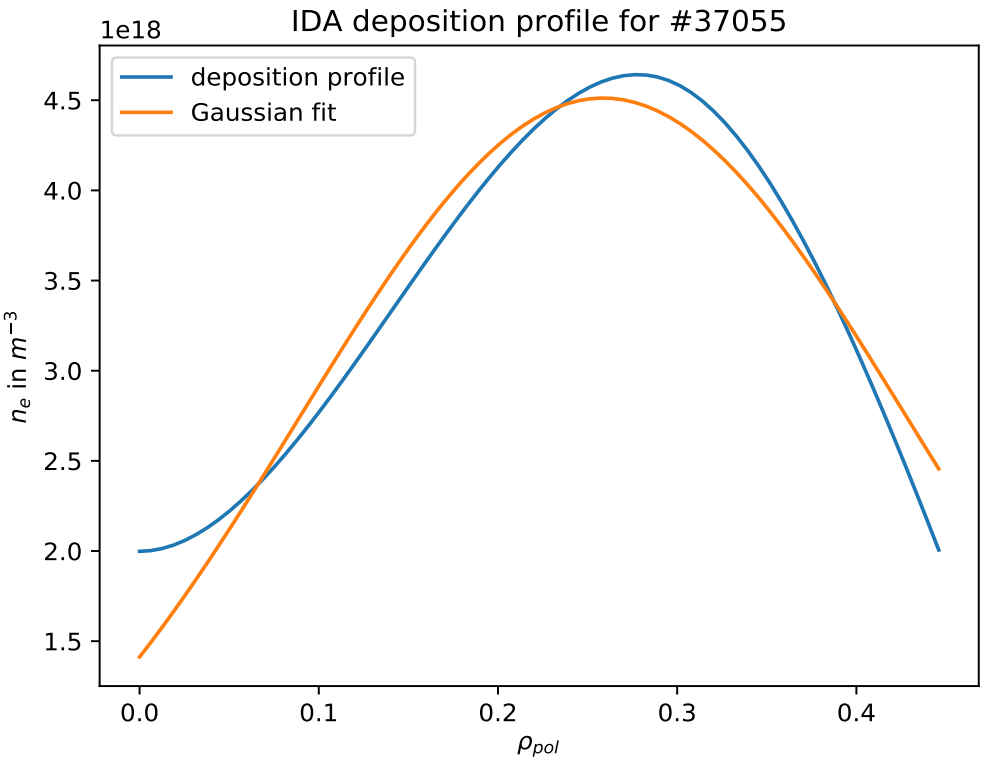

Figure 43: Deposition profile for a single pellet, fitted by a gaussian function

The blue line in figure 43 shows a typical deposition profile of a pellet, which was obtained by subtracting the IDA density profile before a pellet from the density profile after the respective pellet. The orange line in figure 43 depicts a Gaussian fit, which can be parameterised, using:

$$f(\rho) = a \cdot \exp\left(-\frac{(\rho - b)^2}{2c^2}\right) \tag{83}$$

with the constants a,b and c, which can be fitted to the respective profile. The constant c is analogous to the standard deviation of a normal distribution and is therefore a measure for the deposition width of the deposition profile $f(\rho)$. Since $\tau_{p,dist}$ is a measure for the local transport, the constant c can be used as a diffusion length. It should be noted, that c is given as a $\Delta\rho$ value. Thereby, $L_{dif} = a_{minor} \cdot c$, with a_{minor} being the minor plasma radius. The resulting diffusion coefficient $D(\rho_{plt})$ therefore reads:

$$D(\rho_{plt}) = \frac{(a_{minor} \cdot c)^2}{\tau_{p,dist}} \tag{84}$$

Figure 44 shows the values for $D(\rho_{plt})$ as a function of the peak density $f_p = \frac{\Gamma_{plt}}{\Gamma_{tot}}$.

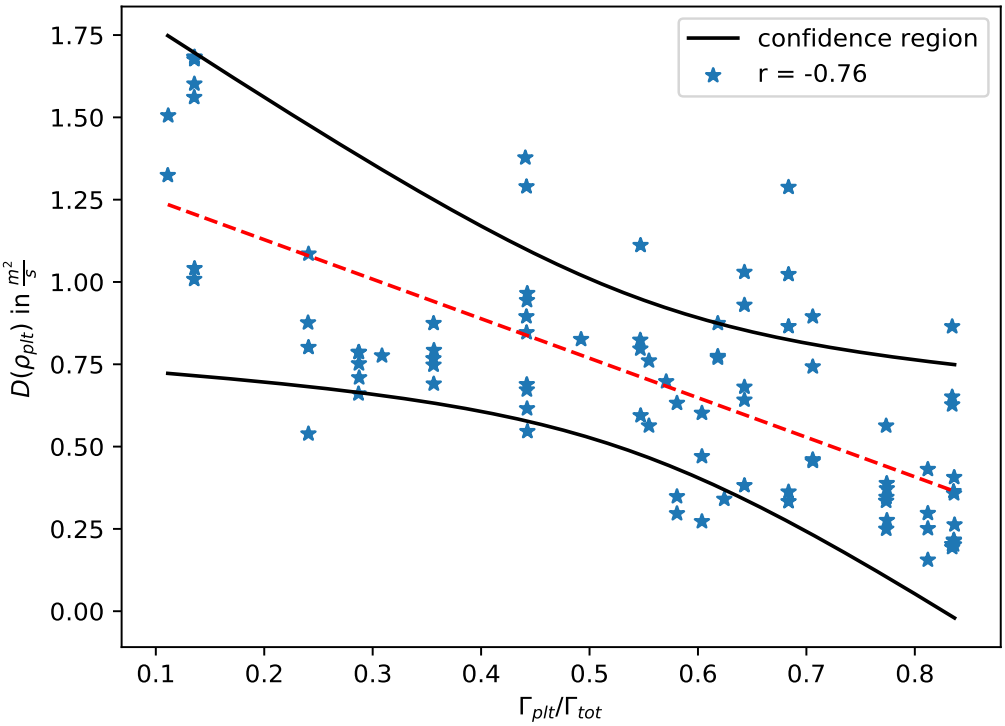

Figure 44: $D(\rho_{plt})$ as a function of f_p.

Similar to figure 41, $D(\rho_{plt})$ decreases linearly as a function of f_p. The fact that figure 43 also shows a linear trend, makes the alternative definition for D_{eff} (equation 80) more likely. Even though, D_{eff} is an averaged diffusion coefficient and $D(\rho_{plt})$ a local diffusion coefficient, the change in D_{eff} should be dominated by the change in diffusivity for radii smaller than the pedestal top $\rho_{ped,top}$. Since ρ_{plt} is located within this area, $\partial Deff \approx \partial D(\rho_{plt})$ should be a valid approximation, making equation 80 seem more sophisticated.

5.5 Impurites

As mentioned in Chapter 5.1, there might be a boundary in terms of a maximum achievable pellet flux share. This subsection is dedicated to observing whether this boundary could arise from a rising concentration of impurities.

Peaked density profiles and a reduction of gas-puff as depicted in figure 36, are of-

ten accompanied by an increase in impurities [72]. While low-Z impurities like carbon are less crucial, high Z-impurity concentrations of elements like tungsten could lead to a disruption of the plasma discharge. Therefore, considering the tungsten concentrations of the performed discharges is important to ensure a stable conduction of further reactor relevant discharges.

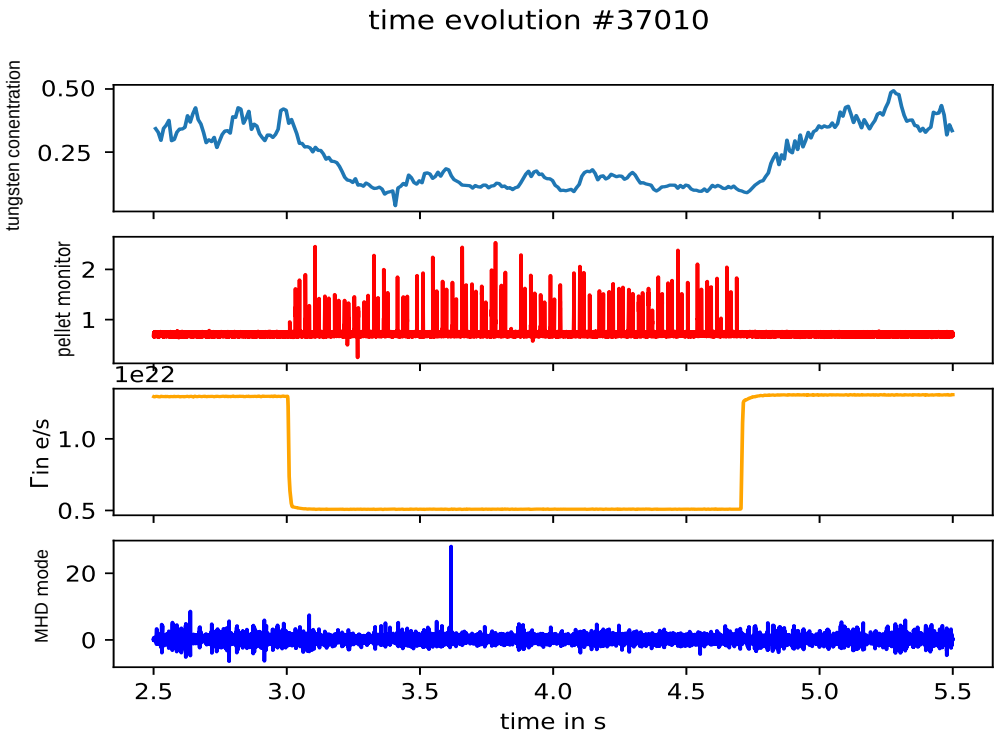

Figure 45: Time evolution of different signals of # 37010.

Figure 45 depicts different signals of discharge 37010. At the top, the Grazing incidence [73] (GIZ) signal for the tungsten concentration is shown. During the exchange of gas by pellets, the concentration of tungsten seems to decrease significantly. At the bottom of figure 40, the MHD activity is also depicted which remains virtually unaffected during the discharge. Thus, MHD modes are unlikely to be the reason for this behaviour.

However, figure 45 cannot be used to draw the conclusion that pellets curb tungsten impurities since:

- The GIZ signal measures the concentration of a certain ionization level of tungsten. By injecting pellets, the temperature is decreasing (figure 25) and therefore

the position of measurement also shifts towards hotter plasma regions ($\rho_{measured}$ is shifting towards the core).

- Due to the significant density increase induced by pellets, the tungsten concentration decreases, even if the absolute tungsten content stays the same. Therefore, considering the tungsten density n_W is more appropriate to analyse further, since it is independent of n_e.

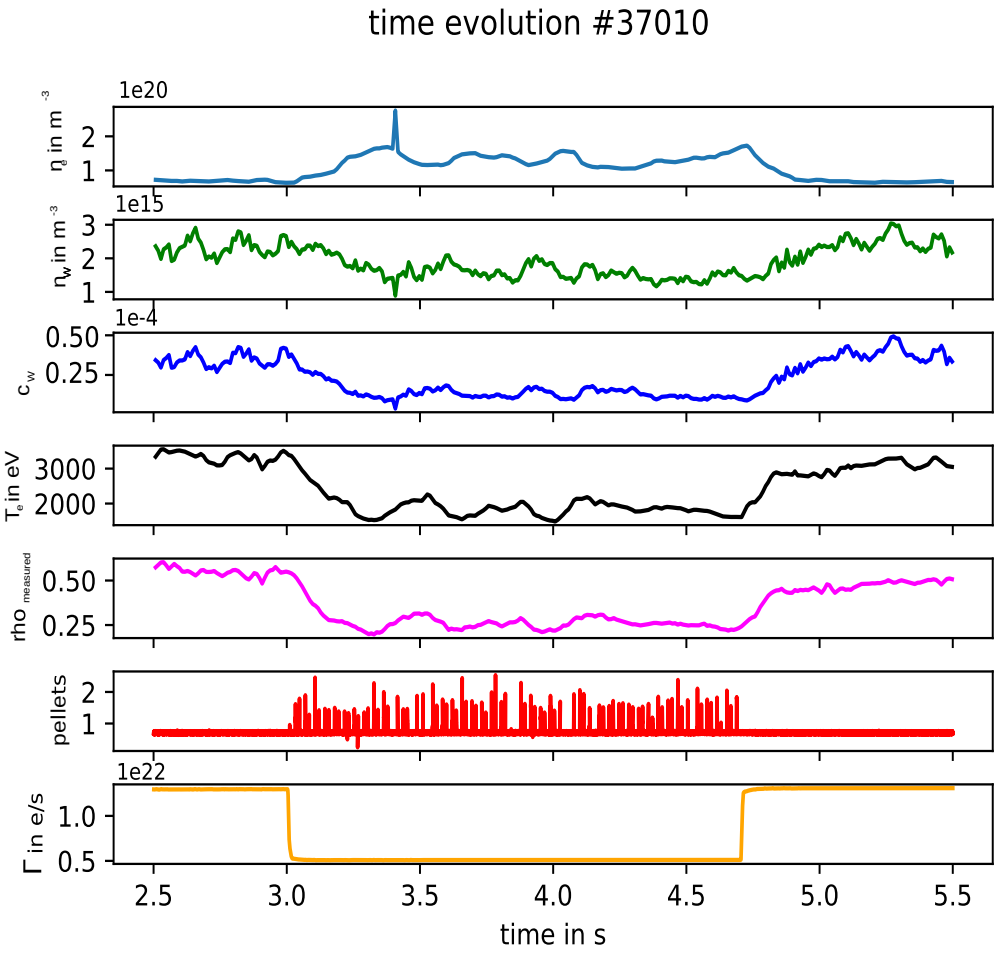

Figure 46: Time evolution of different signals of # 37010

Figure 46 now contains additional signals. When considering the second (n_W) and third (c_W) subplot, it is evident that the decrease in tungsten density is less significant than the decrease in concentration. However, when contemplating subplot four and five, it can be seen, that the measured ρ-value decreases in a similar fashion to the electron temperature T_e.

Therefore, the only valid comparison can be made, using the tungsten particle density n_W before and after the pellet injection, when an approximately similar $\rho_{measured}$ is given. Here, some cases indicate that the overall tungsten content even increases increases, as shown in figure 47, depicting the tungsten density of discharge 37012:

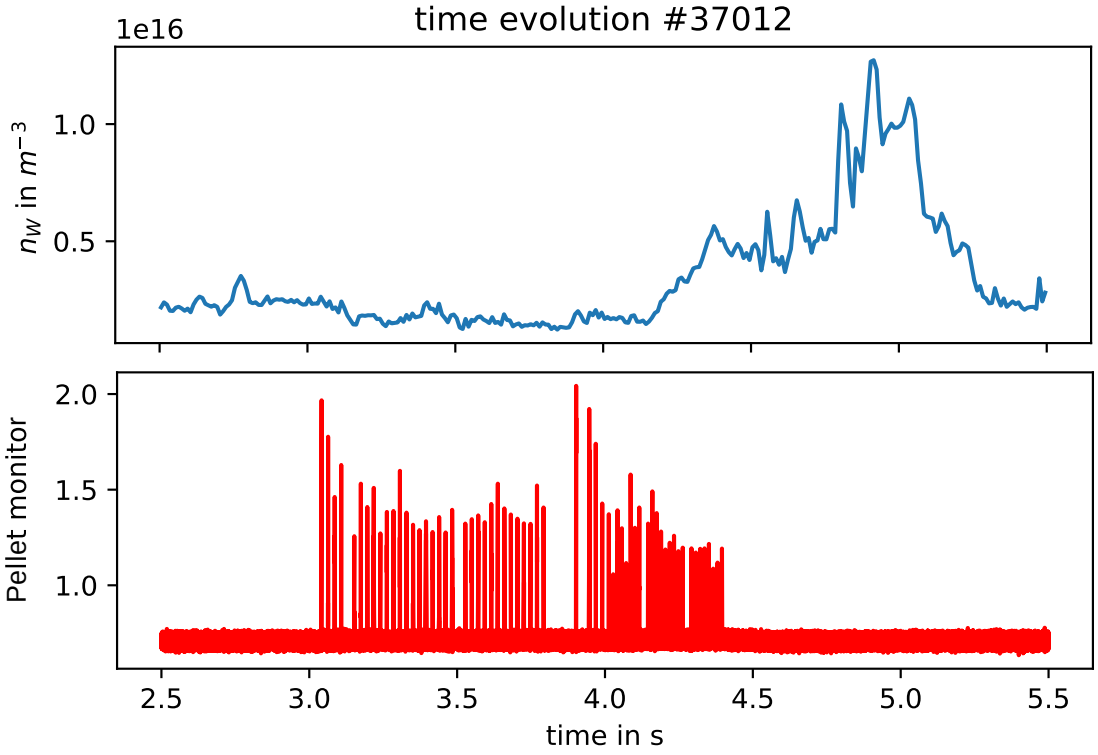

Figure 47: Tungsten density n_W for discharge # 37012

In this specific case, the tungsten density is significantly less before the pellet injection phase, compared to after the injection phase ended. However, after some time, the tungsten density relaxed back to a similar value, compared to the values, before the pellet injection phase, showing a clear inertia of the tungsten density [74], compared to the electron density. An illustration for the tungsten density of further discharges, can be seen in Appendix.

All things considered, pellet usage seems to barely affect the overall tungsten content. Moreover, during the experimental phase, there were barely any instabilities and signs of a plasma disruption even when the pellet-flux fraction was raised to over 80 %.

Instead of further analysing each impurity species, the effective ion charge number Z_{eff}, which is a measure for impurities, can also be considered. For seven out of the ten discharges, Z_{eff} profiles (IDZ) had been available. By using these profiles as input for equation 90 (Appendix) and dividing by the volume, a volume-averaged Z_{eff} value can be calculated.

$$Z_{eff,vav} = \frac{\int_V Z_{eff}(\rho)\, dV}{\int_V dV} \tag{85}$$

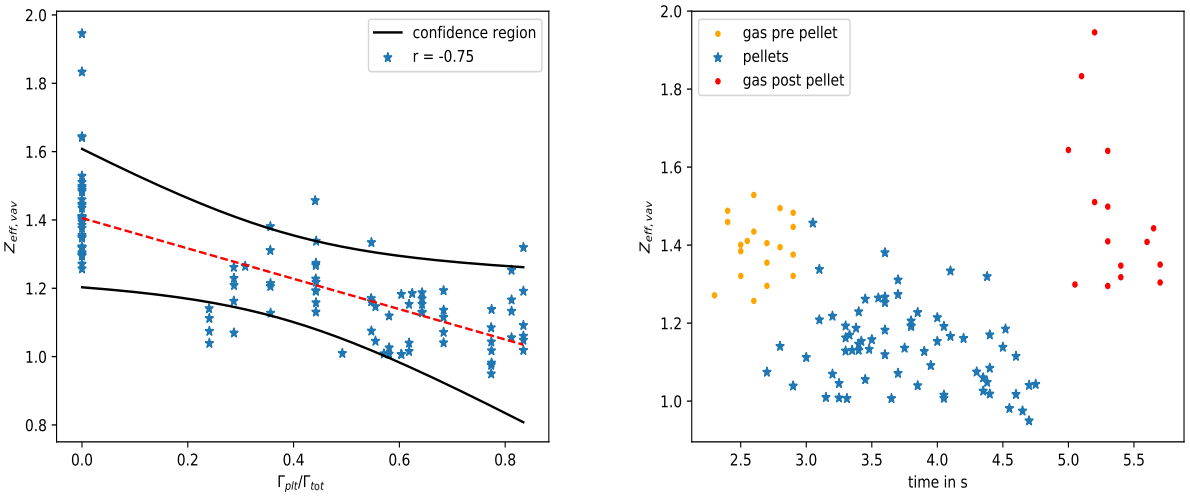

Figure 48: $Z_{eff,vav}$ as a function of $\frac{\Gamma_{plt}}{\Gamma_{tot}}$ (left) and $Z_{eff,vav}$ as a function of time (right). The orange markers indicate valuse before-, the blue ones during- and the red ones post pellet injection.

Figure 48 (left) depicts the volume-averaged effective ion charge number as a function of the peak density $\frac{\Gamma_{plt}}{\Gamma_{tot}}$. The decreasing trend in Z_{eff}, has been previously observed in pellet-fuelled discharges [75, 76] and is likely to be attributed to a significant increase in (core-) density with rising share in pellet flux. Therefore, the impurity concentration decreases. However, the overall impurity content is virtually unaffected, as shown in figure 48 (right). As for that, the orange and red dots have to be considered, as they describe Z_{eff} data before and after pellet injection phases respectively. It can be seen, that after pellet injection stops and the density decreases, Z_{eff} values approximately return to the initial value. However, the red dots contain some outliers, which might indicate that pellets increase the overall impurity content slightly. All things

considered, pellet usage leads to a reduction of Z_{eff} during the injection phase, which is desirable for future reactor concepts, since the bremsstrahlung, which counts as a power loss also decreases with Z_{eff} decreasing (equation 9).

6 Summary and outlook

In this section, summaries of the main chapters 4 and 5 will be given. Furthermore, an outlook on future experiments and analyses is provided.

6.1 Summary of chapter 4

Analysis in Chapter 4 has shown, that the H06 (y,dd) confinement scaling is more appropriate for describing data beyond the Greenwald density n_{Gw} in the high density regime, compared to the H98(y,2) confinement scaling. The improvement of H06(y,dd) can be attributed to:

- A contribution of two more tokamak teams compared to H98(y,2)
- A $\propto f_{Gw}^{-0.22 \cdot \ln(f_{Gw})}$ density dependency
- An additional $\propto q_{95}/q_{cyl.}$ dependency which is closely related to plasma shaping

For contemplating the influence of the separatrix density $n_{e,sep}$ on confinement, the H06(y,dd) has been considered, due to the reasons elaborated above. The results of the analyses are summarized below.

- The median separatrix temperature $T_{e,sep}$ for this dataset (containing N-Seeding, High Shaping (HS) and Reference discharges) was analysed to be $T_{e,sep}$ = 97 eV, using a 2-point model. However, deviations of $\pm$ 20 eV were found. Therefore, an assumption of $T_{e,sep}$ = 100 eV would have led to considerable deviations in $n_{e,sep}$
- For N-Seeding , a H06(y,dd) $\propto n_{e,sep}^{-0.13}$ dependency was found
- For HS/ITER BL , a H06(y,dd) $\propto n_{e,sep}^{-0.27}$ dependency was observed
- For Reference discharges, no correlation between H06(y,dd) and $n_{e,sep}$ was detected

- No correlation between the separatrix density $n_{e,sep}$ and the line-averaged density $\overline{n_e}$ was found. Therefore, a scenario which would lead to $n_{e,sep}$ being approximately constant (at a low value) might lead to an increase in H06(y,dd) independently of the line-averaged density

As previously done in [59], the correlation between the separatrix density $n_{e,sep}$ and the divertor neutral gas density n_0^{Div} has been observed. It was found that:

- The divertor neutral gas density n_0^{Div} should be obtained, solely using data from baratrons, since the ionization gauges tend to saturate at a certain density value
- For N-Seeding, a $n_{e,sep} \propto n_{0,Div}^{0.42}$ dependency (similar to ref. [59])) was observed
- For HS/ITER BL, a $n_{e,sep} \propto n_{0,Div}^{0.14}$ dependency was noted
- For Reference discharges, a $n_{e,sep} \propto n_{0,Div}^{0.69}$ dependency was found
- The more the separatrix density depends on the divertor neutral gas density, the less the H06(y,dd) seems to be affected by $n_{e,sep}$

6.2 Summary of chapter 5

The experiments, carried out, as described in chapter 5 were closely related to Chapter 4, since they aimed to maintain a constant edge (separatrix) density $n_{e,edge}$. The results of chapter 5 are summarized below:

- By choosing the total particle-influx Γ_{tot} to be constant, an approximately constant edge density $n_{e,edge}$ can be achieved, since control over the particle refuelling from the scrape-off-layer into the main plasma is obtained
- During the discharges, the initial gas-puff was gradually replaced by pellets, keeping a constant pellet mass m_p
- With a total particle flux of $\Gamma_{tot} = 3.0 \cdot 10^{22}$, $\frac{e}{s}$ and a maximum pellet frequency of 70 Hz, 85 % of the gas-puff could be replaced by pellets

- While the edge density remained virtually unaffected, the core density increased in a supra-linear fashion as a function of $f_p = \frac{\Gamma_{plt}}{\Gamma_{tot}}$, reaching values up to three times the Greenwald density n_{Gw}
- Despite the core density rising in a supra-linear fashion and the core temperature only decreasing linearly, a dip in W_{mhd} of approximately 8 %, when increasing f_p from zero to 0.85, was observed
- A non-linear increase in technical particle confinement time $\tau_{p,tech} = \frac{N_e}{\Gamma_{tot}}$ as a function of f_p was perceived, which is equivalent to a rise in particle content
- A rise in pellet flux led to a reduction in impurity concentrations, since Z_{eff} decreased from 1.4 (f_p = 0) to 1.0 (f_p = 0.85). The overall impurity content, however, seems to be slightly higher after the pellet injection phase, compared to before the pellet injection phase

For several results, modeling- and explanatory approaches have been made. In the following, the outcome of these analyses is summarized:

- Due to intensified cooling, pellets penetrate deeper into the plasma. This effect however, was insufficient to explaining the supra-linear increase in core density. When including a Bohm (Gyro Bohm) scaling, as well as collsionality dominated diffusion, however, the rise in $n_{e,core}$ could be explained
- The slight decrease in W_{mhd} as a function of f_p can be attributed to an inhibition of fast particles and therefore a decrease in W_{fi}. This decrease, however, is partially compensated by an increase in thermal energy W_{th} (due to a shaping in the core pressure profile). The rise in W_{th} can be estimated to be 10-20 %. This shift in energy is desirable, since fast particles will not contribute to the neutron flux in a reactor [70]
- The technical particle confinement time $\tau_{p,tech}$, as well as the disturbed particle confinement time $\tau_{p,dist}$ could be converted into diffusion coefficients. Both diffusion coefficient decreased as a function of f_p

All things considered, a scenario has been developed, which can not only be used, to obtain control over the plasma particle refuelling, but which has also shown that replacing gas-puff with pellets leads to an increase in particle content and thermal plasma energy, while simultaneously reducing Z_{eff}. Therefore, the reactor-relevance of pellets should be, once more, emphasised.

6.3 Outlook

When combining the results of sections 4 and 5, it is standing to reason, to conduct experiments, where confinement enhancing methods like either Nitrogen-Seeding or High Shaping/ITER BL is applied, while simultaneously keeping the overall particle-influx approximately constant at a relatively low value. According to figure 19, this might then lead to a gain in extra confinement, independently of the line-averaged density $\overline{n_e}$. To implement that experimentally, a lower total particle-influx than $\Gamma_{tot} = 3.0 \cdot 10^{22} \frac{e}{s}$ has to be chosen. The reasons for that are observations of peak densities $f_p = \frac{\Gamma_{plt}}{\Gamma_{tot}}$ higher than 0.85, as well as a regulation of a lower edge (separatrix) density.

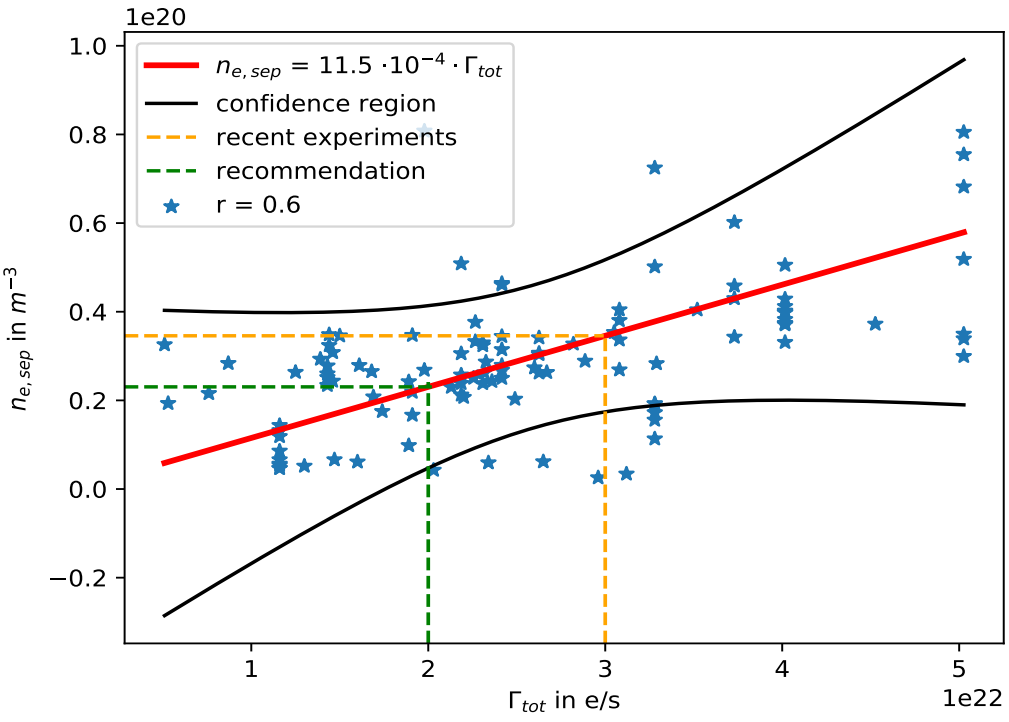

Figure 49: Separatrix density $n_{e,sep}$ as a function of total particle-influx Γ_{tot}

As shown in figure 49, an overall lower total particle flux has to be chosen, in order to decrease $n_{e,sep}$, which then might lead to an increase in H06(y,dd). A potential particle flux to observe this phenomenon would be $\Gamma_{tot} = 2.0 \cdot 10^{22}\ \frac{e}{s}$, as depicted by the green dotted lines in figure 49. With that scenario, the dependence of the separatrix density on confinement, as well as the impact of higher peak densities than 0.85 on plasma physical paraterms and stability can be observed.

7 Summary and outlook in German

Dieses Kapitel dient der Zusammenfassung der Hauptkapitel 4 und 5. Darüberhinaus, wird es durch Ausblicke auf zukünftige Experimente und Analysen abgerundet.

7.1 Zusammenfassung Kapitel 4

Analysen des Kaptitels 4 haben gezeigt, dass die Skalierung H06(y,dd) wesentlich besser ist als H98(y,2), wenn es darum geht, Energieeinschluss im Hochdichtebereich, also für linien-gemittelte Dichten größer als die Greenwalddichte n_{Gw}, zu beschreiben. Die Vorteile von H06(y,dd) lassen sich zurückführen auf:

- Zwei mehr Tokamak Teams, welche mit Daten zur Erstellung von H06(y,dd) beigetragen haben
- Einer $\propto f_{Gw}^{-0.22\cdot\ln(f_{Gw})}$ Dichteabhängigkeit
- Einen zusätzlichen freien Paramter $\propto q_{95}/q_{cyl.}$, welcher die Formung des Plasmas beschreibt

Um die Abhängigkeit des Energieeinschlusses von der Separatrixdichte zu prüfen, wurde folglich ausschließlich die H06(y,dd) Skalierung betrachtet. Die Ergebnisse der Analyse werden im Folgenden zusammengefasst:

- Der Median der berechneten Sepatrixtemperaturen $T_{e,sep}$ für das Datenset aus Stickstoff-Seeding, High Shaping (HS) und Refenz Entladungen, beträgt $T_{e,sep}$ = 97 eV. Jedoch gab es hierbei Schwankungen von ungefähr $\pm$ 20 eV, was die Annahme von $T_{e,sep}$ = 100 eV im Anbetracht der Gradienten der Profile im Bereich des Randes, unbrauchbar macht
- Für N-Seeding wurde eine H06(y,dd) $\propto n_{e,sep}^{-0,13}$ Abhängigkeit gefunden
- Für HS/ITER BL ergab die Analyse eine H06(y,dd) $\propto n_{e,sep}^{-0,27}$ Abhängigkeit
- Für die Referenzentladungen wurde keine Korrelation zwischen H06(y,dd) und $n_{e,sep}$ gefunden

- Auch zwischen der Seperatrixdichte und der liniengemittelten Dichte $\overline{n_e}$ wurde keine nennenswerte Korrelation gefunden. Daher könnte durch eine niedrige, konstante Separatrixdichte eine Erhöhung des Energieeinschlusses herbeigeführt werden, welcher unabhängig von $\overline{n_e}$ ist

Ähnlich zu Referenz [59] wurde zudem eine Korrelationsanalyse zwischen der Separatrixdichte $n_{e,sep}$ und der Divertor-Neutralsgasdichte n_0^{Div} für die drei Kategorien N-Seeding, HS und Referenz duchgeführt. Die Analysen ergaben:

- Dass n_0^{Div} anhand von Baratron-Daten ausgewertet werden sollte, da die Ionisationmessgeräte ab einer bestimmten Flussdichte sättigen
- Eine $n_{e,sep} \propto n_{0,Div}^{0,42}$ Abhängigkeit für N-Seeding, ähnlich zu den Abhängigkeiten aus Ref. [59]
- Eine $n_{e,sep} \propto n_{0,Div}^{0,14}$ Abhängigkeit für die Kateogrie HS/ITER BL
- Eine $n_{e,sep} \propto n_{0,Div}^{0,69}$ Abhängigkeit für die Referenzentladungen
- Es wird deutlich, dass die Separatrixdichte umso mehr Einfluss auf den Energieeinschluss hat, je weniger sie von der Divertorneutralgasdichte abhängt

7.2 Zusammenfassung Kapitel 5

Die Experimente welche für Kapitel 5 durchgeführt wurden, beruhten zudem auf den Resultaten von Kapitel 4, da es unter Anderem das Ziel war, eine konstante Rand-, bzw. Separatrixdichte zu erzielen. Die Ergebnisse der Experimente werden im Folgenden aufgelistet:

- Indem der Gesamtfluss an Teilchen Γ_{tot} annäherungsweise konstant gehalten wurde, stellte sich auch eine nahezu konstante Randdichte ein. Dies lässt sich darauf zurückführen, dass Kontrolle über das Recycling von Partikeln in das Plasma erlangt wurde
- Während der Entladungen wurde der usprüngliche Gasfluss schrittweise durch Pelletfluss substituiert, wobei eine konstante Pelletmasse m_p beibehalten wurde

- Bei einem Gesamtteilchenfluss von Γ_{tot} = 3,0 $\cdot 10^{22}$, $\frac{e}{s}$ und einer maximalen Pelletrepetitionsrate von 70 Hz, konnten 85 % des ursprünglichen Gasflusses ausgetauscht werden

- Während die Randdichte in guter Näherung konstant blieb, stieg die Zentraldichte, als Funktion der Spitzendichte $f_p = \frac{\Gamma_{plt}}{\Gamma_{tot}}$, mit einem nicht-linearen Verlauf an und erreichte Werte bis zu dreimal n_{Gw}

- Trotz des nicht-linearen Anstiegs der Zentraldichte und einem linearen Abfall der Zentraltemperatur $T_{e,core}$, konnte ein leichter Abfall von ungefähr 8 % der Gesamtenergie W_{mhd} festgestellt werden, wenn die Spitzendichte von f_p = 0 zu f_p = 0,85 erhöht wurde

- Eine nicht-linearer Anstieg der technischen Teilcheneinschlusszeit $\tau_{p,tech} = \frac{N_e}{\Gamma_{tot}}$ wurde ersichtlich, was bei den experimentellen Randbedingungen, gleichbedeutend mit einem Anstieg des Teilcheninventars im Plasma ist

- Eine Erhöhung des Pelletflusses von f_p = 0, zu f_p = 0,85, sorgte während der Phase der Pelletinjektion, zu einer Erniedrigung der effektiven Plasmaladungszahl Z_{eff}, von 1,4 zu 1,0. Es sei jedoch zu erwähnen, dass dies nur einem Rückgang in den Konzentrationen entspricht. Die Dichte an Vernunreinigungen scheint nahezu konstant zu bleiben (oder sogar leicht zu steigen)

Für einige der Resultate, wurden Modellansätze, sowie Erklärungsansätze in Form von Analysen geprüft. Die Resultate jener ergaben:

- Durch den Trivialeffekt der tieferen Pelleteindringung durch Kühlung des Plasmas, wird der nicht-lineare Anstieg der Zentraldichte $n_{e,core}$ noch unterschätzt. Erst durch das Einführen einer Bohm (Gyro Bohm) Skalierung, sowie von Diffusion, dominiert durch erhöhte Kollisionalität, konnten die Messdaten beschrieben werden

- Die geringfügige Abnahme von W_{mhd} in Abhängigkeit der Spitzendichte, lässt sich darauf zurückführen, dass eine Abbremsung der schnellen Teilchen und

daher eine Senkung in W_{fi} einhergeht. Die Absenkung von W_{fi} wird jedoch teilweise durch einen Anstieg des kinetischen Energieinhaltes kompensiert, welcher ungefähr 10-20 % ansteigt. Diese Umlagerung der Energie ist für einen zukünftigen Reaktor von Vorteil, da schnelle Teilchen nicht zum Neutronenfluss im Reaktor beitragen werden [70]

- Die technische Teilcheneinfschlusszeit $\tau_{p,tech}$, sowie die (durch Pellets) gestörte Teilcheneinschlusszeit $\tau_{p,dist}$ konnten zu Diffusionskoeffizienten überführt werden. Beide zeigten einen abfallenden (linearen) Trend als Funktion der Spitzendichte f_p

Zusammenfassend lässt sich sagen, dass ein Szenario entwickelt wurde, mit dem nicht nur Kontrolle über das Recycling von Plasma erlangt wurde, sondern welches auch zeigte, dass das Ersetzen von Gas- durch Pelletlfuss zu einem Anstieg in Teilcheninventar und thermischen Energieinhalt, sowie einer Absenkung von Z_{eff} führte. All diese Aspekte weisen auf, dass Pellets für einen zukünftigen Reaktorbetrieb unerlässlich sind.

7.3 Ausblicke

Durch Kombination der Analysen aus den Kapiteln 4 und 5 liegt es nahe, Experimente durchzuführen, bei welchen die Methoden N-Seeding oder High Shaping/ITER BL angewandt werden und zudem die Randdichte durch einen konstanten Gesamtteilchenfluss kontrolliert wird. Wird zudem ein niedriger Wert für die Randdichte gewählt, so sollte nach Abbildung 19 eine Verbesserung des Energieeinschlusses, unabhägig zur linien-gemittelten Dichte $\overline{n_e}$ einhergehen. Jedoch sei darauf zu achten, einen geringeren Gesamtteilchenfluss als $\Gamma_{tot} = 3,0 \cdot 10^{22}\ \frac{e}{s}$ zu wählen. Gründe hierfür sind, dass bei einem geringerem Gesamtteilchenfluss, höhere Spitzendichten als f_p = 0,85 untersucht werden können. Des Weiteren sollte sich bei geringerem Γ_{tot} eine niedrigere Rand-, bzw. Separatrixdichte einstellen.

Unter Betrachtung von Abbildung 49, muss ein niedrigerer Gesamtfluss gewählt

werden, um die Separatrixdichte $n_{e,sep}$ zu verringern, was nach Abbildung 19 zu einer Erhöhung von H06(y,dd) führen könnte. Eine Empfehlung für einen neuen Gesamtteilchenfluss wäre $\Gamma_{tot} = 2,0 \cdot 10^{22}\ \frac{e}{s}$, wie in grünen, gestrichelten Linien in Abbildung 49 dargestellt. Bei diesem Gesamtfluss könnte der Einfluss der Separatrixdichte auf H06(y,dd) näher untersucht werden und zudem können die Einflüsse von Spitzendichten größer als $f_p = 0{,}85$ auf Plasmastabilität und andere plasma-physikalische Parameter geprüft werden.

References

[1] Peter Thomas Lang et. al. H-mode confinement in the pellet-enforced high-density regime of the all-metal-wall tokamak ASDEX Upgrade. *Nuclear Fusion*, 2020.

[2] P.T. Lang, T.C. Blanken, M. Dunne, R.M. McDermott, E. Wolfrum, V. Bobkov, F. Felici, R. Fischer, F. Janky, A. Kallenbach, O. Kardaun, O. Kudlacek, V. Mertens, A. Mlynek, B. Ploeckl, J.K. Stober, W. Treutterer, and H. Zohm and. Feedback controlled, reactor relevant, high-density, high-confinement scenarios at asdex upgrade. *Nuclear Fusion*, 58(3):036001, 2018.

[3] H. J. Sun, E. Wolfrum, B. Kurzan, T. Eich, K. Lackner, A. Scarabosio, I. Paradela Pérez, O. Kardaun, M. Faitsch, S. Potzel, U. Stroth, and the ASDEX Upgrade Team. Study of near sol decay lengths in asdex upgrade under attached and detached divertor conditions. *Plasma Physics and Controlled Fusion*, 59(10):105010, 2017.

[4] R.J. Goldston. Heuristic drift-based model of the power scrape-off width in low-gas-puff h-mode tokamaks. *Nuclear Fusion*, 52(1):013009, 2011.

[5] C. Angioni et. al. A comparison of the impact of central ECRH and central ICRH on the tungsten behaviour in ASDEX Upgrade H-mode plasmas. *Nuclear Fusion*, 57(5):056015, 2017.

[6] F. Wagner. Is fusion still needed ? ipp summer university 2019.

[7] Roselyne Joyeux and Ronald D. Ripple. Household energy consumption versus income and relative standard of living: A panel approach. *Energy Policy*, 35(1):50–60, 2007.

[8] Max-Planck-Institut für Plasmaphysik. Tritium.

[9] K. Philberth. Future regard to the atomic waste disposal problem. *Journal of Glaciology*, 16(74):277–278, 1976.

[10] A. M. Bradshaw, T. Hamacher, and U. Fischer. Is nuclear fusion a sustainable energy form? *Fusion Engineering and Design*, 86(9):2770–2773, 2011.

[11] Philip A. Davis and Dan C. Galeriu. Tritium tritium in the environment tritium in the environment. In Robert A. Meyers, editor, *Encyclopedia of sustainability science and technology*, Springer reference, pages 10997–11025. Springer, New York, NY, 2012.

[12] Michael I. Ojovan, W. E. Lee, and Stepan N. Kalmykov, editors. *An introduction to nuclear waste immobilisation*. Elsevier, Amsterdam, Netherlands, third edition edition, 2019.

[13] Michael Kaufmann. *Plasmaphysik und Fusionsforschung*. Springer Fachmedien Wiesbaden, Wiesbaden and s.l., 2., überarb. aufl. 2013 edition, 2013.

[14] Bernard Bigot. Iter: A unique international collaboration to harness the power of the stars. *Comptes Rendus Physique*, 18(7):367–371, 2017.

[15] Satoshi Konishi, Satoshi Nishio, and Kenji Tobita. Demo plant design beyond iter. *Fusion Engineering and Design*, 63-64:11–17, 2002.

[16] S. Dingwall, C. E. Mills, N. Phan, K. Taylor, and D. R. Boreham. Human health and the biological effects of tritium in drinking water: Prudent policy through science – addressing the odwac new recommendation. *Dose-Response*, 9(1):6–31, 2011.

[17] ITER-Advantages of fusion. Advantages of fusion, 2020-11-23T17:10:12.000Z.

[18] Andreas Dinklage, Thomas Klinger, Gerrit Marx, and Lutz Schweikhard. *Plasma Physics: Confinement, Transport and Collective Effects*, volume 670 of *Lecture Notes in Physics*. Springer-Verlag GmbH, Berlin Heidelberg, 2005.

[19] M. Apostol and L. C. Cune. On the stability of a classical plasma. *Physics Letters A*, 383(16):1831–1835, 2019.

[20] Tianbai Xiao, Martin Frank. A stochastic kinetic scheme for multi-scale flow transport with uncertainty quantification. *Preprint*, 2020.

[21] Yongsheng Huang, Naiyan Wang, Xiuzhang Tang, and Yijin Shi. Relativistic plasma expansion with maxwell-jüttner distribution. *Physics of Plasmas*, 20(11):113108, 2013.

[22] Wolfram MathWorld. Bessel function of the second kind, 02.01.2020.

[23] Boris N. Breizman, Pavel Aleynikov, Eric M. Hollmann, and Michael Lehnen. Physics of runaway electrons in tokamaks. *Nuclear Fusion*, 59(8):083001, 2019.

[24] O. Embréus. Kinetic modelling of runaways in plasmas. *undefined*, 2019.

[25] https://www.ipp.mpg.de/9018/iter, iter-teilnahme, Access: 2020.

[26] https://www.ipp.mpg.de/9031/demo, demonstrationskraftwerk demo, Access: 2020.

[27] H. Vernickel, M. Blaumoser, K. Ennen, J. Gruber, O. Gruber, O. Jandl, M. Kaufmann, H. Kollotzek, W. Köppendörfer, H. Kotzlowski, E. Lackner, K. Lackner, J. Neuhauser, J.-M. Noterdaeme, M. Pillsticker, R. Pöhlchen, H. Preis, K.-G. Rauh, H. Röhr, H. Schneider, W. Schneider, U. Seidel, B. Sombach, B. Streibl, G. Venus, F. Wesner, and A. Wieczorek. Asdex upgrade: A poloidal divertor tokamak adapted to reactor requirements. *Journal of Nuclear Materials*, 128-129:71–77, 1984.

[28] https://www.ipp.mpg.de/1471827/asdex_upgrade, Access: 2020.

[29] https://www.ipp.mpg.de/83834/stellarator, stellarator, Access: 2020.

[30] V. Mukhovatov et. al. Overview of physics basis for ITER. *Plasma Physics and Controlled Fusion*, 45(12A):A235, 2003.

[31] Josef Neuhauser, Hans-Stephan Bosch, David Coster, Albrecht Herrmann, and Arne Kallenbach. Chapter 8: Edge and divertor physics in asdex upgrade. *Fusion Science and Technology*, 44(3):659–681, 2003.

[32] D. D. Ryutov, P. N. Yushmanov, D. C. Barnes, and S. V. Putvinski. Divertor for a linear fusion device. AIP Conference Proceedings, page 060003. AIP Publishing LLC, 2016.

[33] A. Herrmann, H. Greuner, N. Jaksic, M. Balden, A. Kallenbach, K. Krieger, P. de Marné, V. Rohde, A. Scarabosio, and G. Schall. Solid tungsten divertor-iii for asdex upgrade and contributions to iter. *Nuclear Fusion*, 55(6):063015, 2015.

[34] Alinka Lépine-Szily and Pierre Descouvemont. Nuclear astrophysics: nucleosynthesis in the universe. *International Journal of Astrobiology*, 11(4):243–250, 2012.

[35] G. Khatri. Toroidal equilibrium feedback control at extrap t2r. *thesis*, 2010.

[36] Mainak Bandyopadhyay. Studies of an inductively coupled negative hydrogen ion radio frequency source through simulations and experiments. *Ipp Report*, page 4/284, 09 2004.

[37] John Wesson. *Tokamaks*, volume 48 of *Oxford science publications*. Clarendon Press, Oxford, 2. ed. edition, 1997.

[38] David Reinberger, Amela Ajanovic, and Reinhard Haas. The technological development of different generations and reactor concepts. In Reinhard Haas, Lutz Mez, and Amela Ajanovic, editors, *The technological and economic future of nuclear power*, Energiepolitik und Klimaschutz, pages 243–258. Springer Fachmedien Wiesbaden, Wiesbaden, 2019.

[39] https://physics.stackexchange.com/users/59863/alf. How to calculate the bremsstrahlung limit in the fusion triple product diagram, 2017.

[40] EUROfusion. Discovery of the high confinement mode, 2005.

[41] H. Zohm. Dynamic behavior of the l-h transition. *Physical Review Letters*, 72(2):222, 1994.

[42] P.T. Lang. Private communication.

[43] E. Stefanikova, M. Peterka, P. Bohm, P. Bilkova, M. Aftanas, M. Sos, J. Urban, M. Hron, and R. Panek. Fitting of the thomson scattering density and temperature profiles on the compass tokamak. *Review of Scientific Instruments*, 87(11):11E536, 2016.

[44] Chundong et. al. Hu. Design of neutral beam-line of east. *Plasma Science and Technology*, 13(5):541–545, 2011.

[45] A. Mlynek, M. Reich, L. Giannone, W. Treutterer, K. Behler, H. Blank, A. Buhler, R. Cole, H. Eixenberger, R. Fischer, A. Lohs, K. Lüddecke, R. Merkel, G. Neu, F. Ryter, D. Zasche, and the ASDEX Upgrade Team. Real-time feedback control of the plasma density profile on asdex upgrade. *Nuclear Fusion*, 51(4):043002, 2011.

[46] N. Rubab and G. Murtaza. Debye length in non-maxwellian plasmas. *Physica Scripta*, 74(2):145, 2006.

[47] B Kurzan, M Jakobi, H Murmann, and ASDEX Upgrade Team. Signal processing of thomson scattering data in a noisy environment in ASDEX upgrade. *Plasma Physics and Controlled Fusion*, 46(1):299–317, dec 2003.

[48] M. Greenwald, J. L. Terry, S. M. Wolfe, S. Ejima, M. G. Bell, S. M. Kaye, and G. H. Neilson. A new look at density limits in tokamaks. *Nuclear Fusion*, 28(12):2199, 1981.

[49] X. Q. Xu, W. M. Nevins, T. D. Rognlien, R. H. Bulmer, M. Greenwald, A. Mahdavi, L. D. Pearlstein, and P. Snyder. Transitions of turbulence in plasma density limits. *Physics of Plasmas*, 10(5):1773, 2003.

[50] Jean Johner. Helios: A zero-dimensional tool for next step and reactor studies. *Fusion Science and Technology*, 59(2):308–349, 2011.

[51] ITER Physics expert group on confinement, ITER Physics expert group on confinement modelling transport database, and ITER Physics basis editors. Chapter 2: Plasma confinement and transport. *Nuclear Fusion*, 39(12):2175, 1999.

[52] R. Fischer and Andreas Dinklage. The concept of integrated data analysis of complementary experiments. *Computer Science*, 2007.

[53] A. Dinklage et. al. Integrated data analysis for fusion: A bayesian tutorial for fusion diagnosticians. *AIP Conference Proceedings*, 988(1):471, 2008.

[54] Peter C. Stangeby. *The plasma boundary of magnetic fusion devices*. Plasma physics series. Institute of Physics Publ, Bristol, 2000.

[55] T. Eich, R.J. Goldston, A. Kallenbach, B. Sieglin, H.J. Sun, ASDEX Upgrade Team, and JET Contributors. Correlation of the tokamak h-mode density limit with ballooning stability at the separatrix. *Nuclear Fusion*, 58(3):034001, 2018.

[56] S. S. Henderson, M. Bernert, S. Brezinsek, M. Carr, M. Cavedon, R. Dux, D. S. Gahle, J. Harrison, A. Kallenbach, B. Lipschultz, B. Lomanowski, A. Meigs, M. O'Mullane, F. Reimold, M. L. Reinke, and S. Wiesen. An assessment of nitrogen concentrations from spectroscopic measurements in the jet and asdex upgrade divertor. *Nuclear Materials and Energy*, 18:147–152, 2019.

[57] Wikipedia, laplace-verteilung, 2018.

[58] Statistics How To. Correlation coefficient: Simple definition, formula, easy steps.

[59] A. Kallenbach, H. J. Sun, T. Eich, D. Carralero, J. Hobirk, A. Scarabosio, M. Siccinio, ASDEX Upgrade team, and EUROfusion MST1 team. Parameter dependences of the separatrix density in nitrogen seeded asdex upgrade h-mode discharges. *Plasma Physics and Controlled Fusion*, 60(4):045006, 2018.

[60] A. Scarabosio, G. Haas, H. W. Müller, R. Pugno, and M. Wischmeier. Measurements of neutral gas fluxes under different plasma and divertor regimes in asdex upgrade. *Journal of Nuclear Materials*, 390-391:494–497, 2009.

[61] F. Reimold, M. Wischmeier, M. Bernert, S. Potzel, D. Coster, X. Bonnin, D. Reiter, G. Meisl, A. Kallenbach, L. Aho-Mantila, and U. Stroth. Experimental studies and modeling of complete h-mode divertor detachment in asdex upgrade. *Journal of Nuclear Materials*, 463:128–134, 2015.

[62] Otto J. W. F. Kardaun. *Classical methods of statistics*. Springer, [Place of publication not identified], 2014.

[63] C.Andelfinger et. al. A new centrifuge pellet injector for fusion experiments. *Review of Scientific Instruments*, 64(4):983, 1998.

[64] K. Lackner. Private communication.

[65] https://www.ipp.mpg.de/1124504/pellets, pellets, Access: 2020.

[66] C. Angioni. Private communication.

[67] C. Angioni et. al. Density peaking, anomalous pinch, and collisionality in tokamak plasmas. *Physical Review Letters*, 90(20):205003, 2003.

[68] M. Erba, T. Aniel, V. Basiuk, A. Becoulet, and X. Litaudon. Validation of a new mixed bohm/gyro-bohm model for electron and ion heat transport against the iter, tore supra and start database discharges. *Nuclear Fusion*, 38(7):1013, 2002.

[69] Livia Casali. Experimental studies and modelling of high radiation and high density plasmas in the asdex upgrade tokamak. *phd thesis*, November 2015.

[70] A. Fasoli et. al. Chapter 5: Physics of energetic ions. *Nuclear Fusion*, 47(6):S264, 2007.

[71] W. Ott et. al. Slowing-down of fast ions in a plasma: Energy transfer, charge exchange losses and wall sputtering. *IPP Report*, 4/161, 1979.

[72] Ralph Dux. Chapter 11: Impurity transport in asdex upgrade. *Fusion Science and Technology*, 44(3):708–715, 2003.

[73] K. Asmussen, K.B Fournier, J.M Laming, R. Neu, J.F Seely, R. Dux, W. Engelhardt, J.C Fuchs, and ASDEX Upgrade Team. Spectroscopic investigations of tungsten in the euv region and the determination of its concentration in tokamaks. *Nuclear Fusion*, 38(7):967–986, 1998.

[74] T. Pütterich. Control and diagnostic of high-z impurities in fusion plasmas. *Ludwig-Maximilians-Universität München, München*, 2014.

[75] Yu Yang, Yi Bao, Jiangang Li, Xuemao Gu, and Yexi He. Pellet injection research on the ht-6m and ht-7 tokamaks. *Nuclear Fusion*, 39(11Y):1871–1874, 1999.

[76] P. T. Lang et. al. High density operation at jet by pellet refuelling*. *Plasma Physics and Controlled Fusion*, 44(9):1919–1928, 2002.

[77] A. Mlynek et. al. Fringe jump analysis and implementation of polarimetry on the asdex upgrade dcn interferometer. *The Review of scientific instruments*, 85(11):11D408, 2014.

[78] Prof. Sharyn O'Halloran. Sustainable development u9611 econometrics ii lecture 9: Logit/probit, 2020.

[79] Lueders. Volumen des torus: Vorlesung informatik.

[80] https://www.easyclass.at/wp-content/uploads/2018/12/ue10bsp76-1.pdf, mathematik-kurse tu wien, differentialgleichungssysteme, Access: 2020.

[81] Prof. Dr. Michael Geisler. Vorlesungsskript mathematische methoden der physik: Fakultät angewandte naturwissenschaften, Access: 2020.

8 Appendix

Within the Appendix, additional information, figures and analyses are shown. Furthermore, tools which have been regularly used for this thesis, are further elaborated

8.1 AUG cross-section and measurement locations

Even though figure 14 and 15 already provide an overview, where the DCN- sightlines, as well as the Thomson Scattering detectors are located, an extra overview figure is now given, which contains the most pivotal diagnostics for this thesis, as well as the injection path of the pellet (orange arrow).

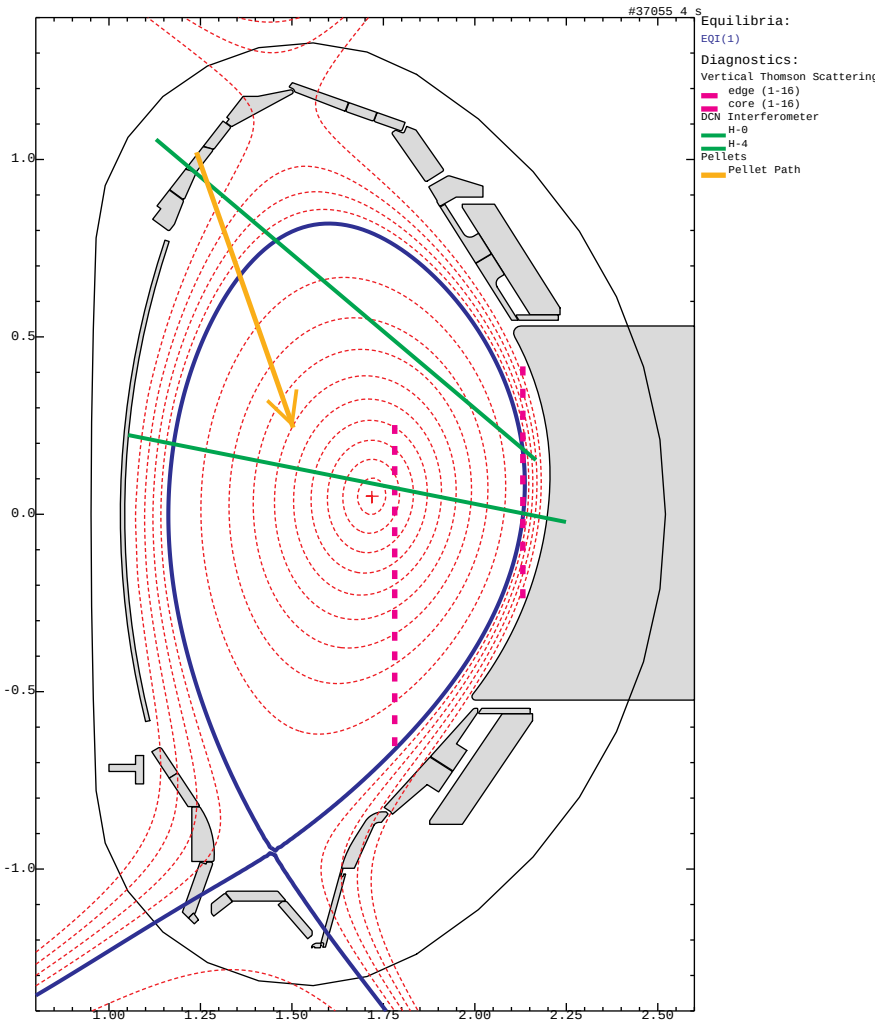

Figure 50: Cross-section and Equilibrium of AUG during #37055

In figure 50, the blue solid line illustrates the position of the separatrix ($\rho = 1$), which is (usually) the last closed magnetic flux surface. The magenta dotted lines indicate core- and edge Thomson scattering detectors (16 each). The green lines illustrate the sightlines H-0 and H-4 of the DCN laser. The H-0 signal was usually used for the line-averaged density $\overline{n_e}$, since it intersects with the pellet path, after a fringe-jump [77] correction (due to the pellets) had been carried out.

8.2 Statistical transformations

Especially in Chapters 4 and 5, statistical transformations have been conducted, with the main intention of transforming a non-linear to a linear trend, where a linear regression and confidence region considerations can be carried out relatively effortlessly.

8.2.1 Natural-logarithmic transformation

This transformation is usually applied to either, solely the y-axis, or both, the x- and y-axis. If solely the y-axis is transformed - using the natural logarithm - and the resulting trend is fitted by a linear model f(x) = $m\cdot$ x + t, a transformation back to a linear y-axis will give:

$$f_{lin}(x) = \mathrm{C} \cdot \exp\left(m \cdot x\right) \tag{86}$$

Alternatively, both axes can be transformed. Here, the resulting fit model on linear axes would be:

$$f_{lin}(x) = \mathrm{C} \cdot x^{m} \tag{87}$$

An application of equation 87 is illustrated in figure 51.

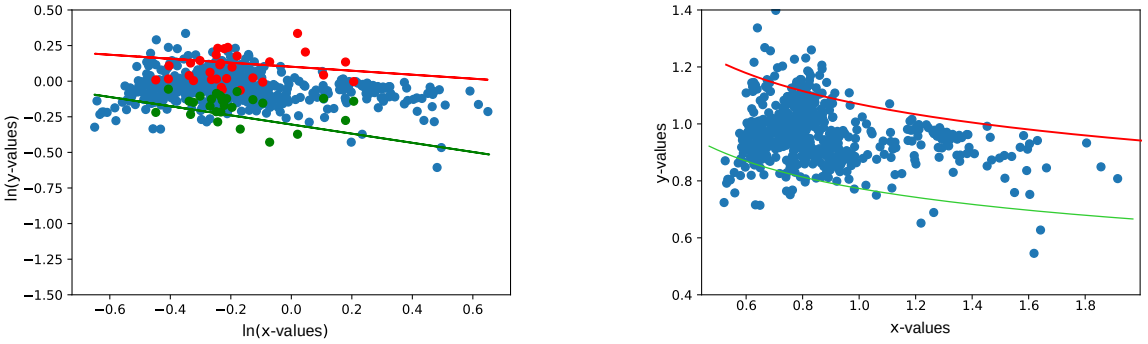

(a) (b)

Figure 51: This example depicts how the upper- and lower boundary of figure 3 have been determined. In (a), the natural logarithm of both, the y- and x- axis has been taken and a linear model has been fitted. In (b) a transformation back to linear axes has been carried out.

Figure 51 (b) shows a model which follows equation 86.

8.2.2 Odds transformation

The Odds transformation is a modification to the logit-transformation, described in [78]. The logit-transformation transforms values x from $(0, 1)$ to $(-\infty, +\infty)$, by calculating $x_{new} = \log\left(\frac{x}{1-x}\right)$. Therefore, it is usually applicable, when either the x- or the y- axis are normalized or given as a probability. The odds transformation, however, transforms the values x to $x_{new} = \frac{x}{1-x}$, thereby from $(0, 1)$ to $(0, +\infty)$.

This concept is especially applicable for Chapter 5. In this Chapter various plasma-physical parameters are plotted against the peak density $f_p = \frac{\Gamma_{plt}}{\Gamma_{plt}+\Gamma_{gas}}$. By performing the Odds transformation, $x_{new} = \frac{\Gamma_{plt}}{\Gamma_{gas}}$ is obtained. An example for the application of this concept is shown in figure 24, where the non-linear fit for the core density has been obtained by an Odds transformation, as depicted in figure 52.

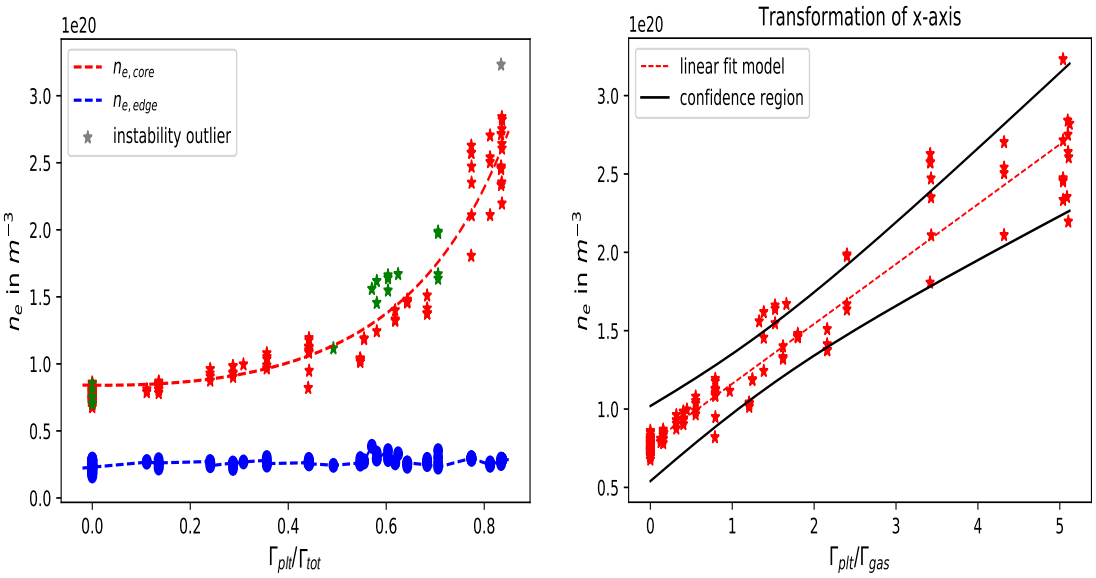

Figure 52: Figure 24 (left) and the Odds transformation of the x-axis (right), leading to a linear model for $n_{e,core}$.

Moreover figure 52 (right) was complemented by a 90 % confidence band for predicting a single observation. Its determination also relied on a linear model. The formula for determining a hyperbolic confidence band can be found in [62].

8.3 Switch in pellet repetition rate

Figure 53 represents the sequence in which the centrifuge frequency was switched, in order to reach a new, time-averaged frequency. This specific sequence refers to example presented in equations 47 and 48.

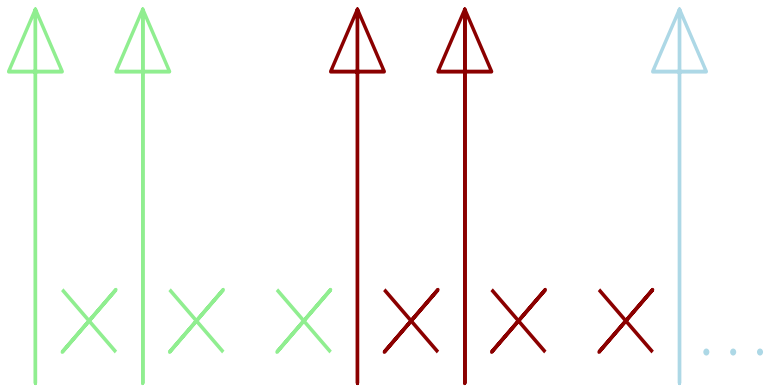

Figure 53: Switching between two centrifuge frequencies to reach time-averaged new frequencies

A new color in figure 53 indicates the start of a new iteration of the sequence.

8.4 Numeric volume integration

In Chapter 4 and 5, for plenty of analyses, numeric volume integrals had to be performed. This subsection will cover the difficulties when performing integrals over the plasma volume of ASDEX Upgrade. Furthermore, it is described, how an algorithm for numeric volume integration has been derived. Lastly, the accuracy of the algorithm will be depicted.

Firstly, it should be elaborated, why an analytic volume integral cannot be performed. For that, figure 50 should be considered. The red dotted lines within figure 50 represent the magnetic flux surfaces. The bold blue line, the so called **separatrix** is the boundary between closed and and open flux surfaces. As for the volume integration, several flux surfaces within the separatrix have to be considered. Therefore, $\rho_{pol} = 1$ is defined as the Sepatratix.
Figure 50 also provides a new angle of contemplating spatial profiles. A profile matches the value of a plasma-physical parameter (e.g. density) to the radius of a closed flux surface, where the parameter is virtually constant.
However, those closed flux surfaces are far away from being an object that is mathematically easy to describe in the context of volume integration. For inner flux surfaces, the argument of fitting an ellipse might be a decent approximation, however, the further the separatrix is being approached, the more the flux surfaces deviate from an ellipse.
One could still argue that the vast majority of flux surfaces could be described by an ellipse in a proper manner. However, since the edge is being weighted higher than the core, this approximation would lead to unusable results. Therefore, the plasma volume has to be integrated numerically. For this specific case, an integration formula for a Torus with an arbitrary shaped cross-section can be used [79].

$$V = \int_0^{2\pi} \int_{x_1}^{x_2} \int_{f_1(x)}^{f_2(x)} x \, dydxd\theta \tag{88}$$

where , $f_1(x)$ and $f_2(x)$ refer to the functions to fit the upper and lower contour of the flux surface. Figure 54 depicts the relevant parameters to compute equation 88.

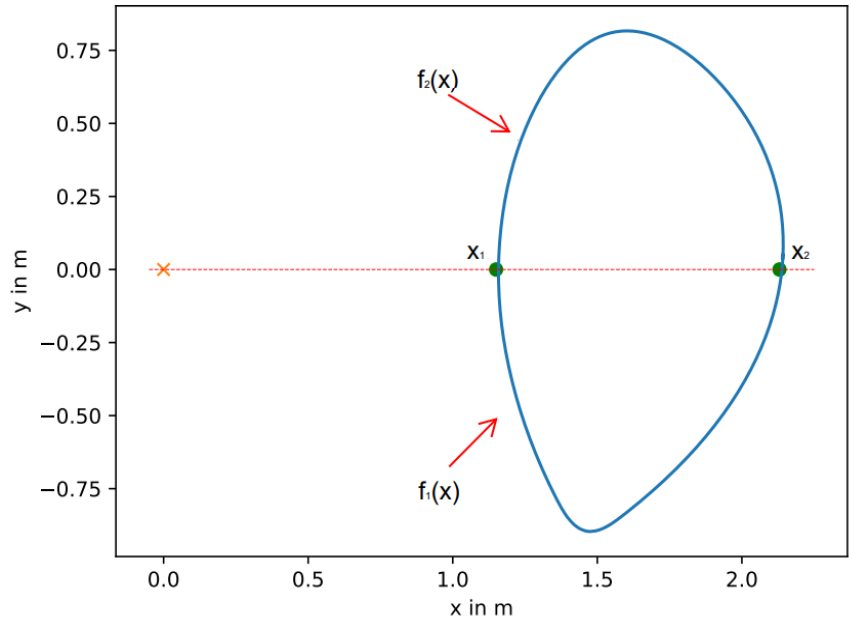

Figure 54: Upper and lower outer contour of discharge 37056

Alternatively, a transformation to polar coordinates can be carried out, where instead of using $f_1(x)$ and $f_2(x)$ only one contour can be described.

$$V = \int_0^{2\pi} \int_0^{2\pi} \int_0^{z(r)} x(r, \varphi)\, r\, dr d\varphi d\theta \tag{89}$$

The integrand of equation 88 got complemented by an extra **r** which is the determinant of the Jacobi matrix, stemming from the coordinate transformation. Furthermore, $x(r, \varphi)$ in equation 89 can be replaced. For that, figure 54 can be reconsidered. There, $x(r, \varphi)$ is simply the distance from the zero point to x_1 (x_{off}) plus the distance x expressed in polar coordinates with x = $r \cdot \cos(\varphi)$. Therefore, equation 89 can be rewritten as:

$$V = \int_0^{2\pi} \int_0^{2\pi} \int_0^{z(r)} (x_{off} + r \cdot cos(\varphi))\, r\, dr d\varphi d\theta \tag{90}$$

The transformation of flux surfaces to polar coordinates is illustrated in figure 55.

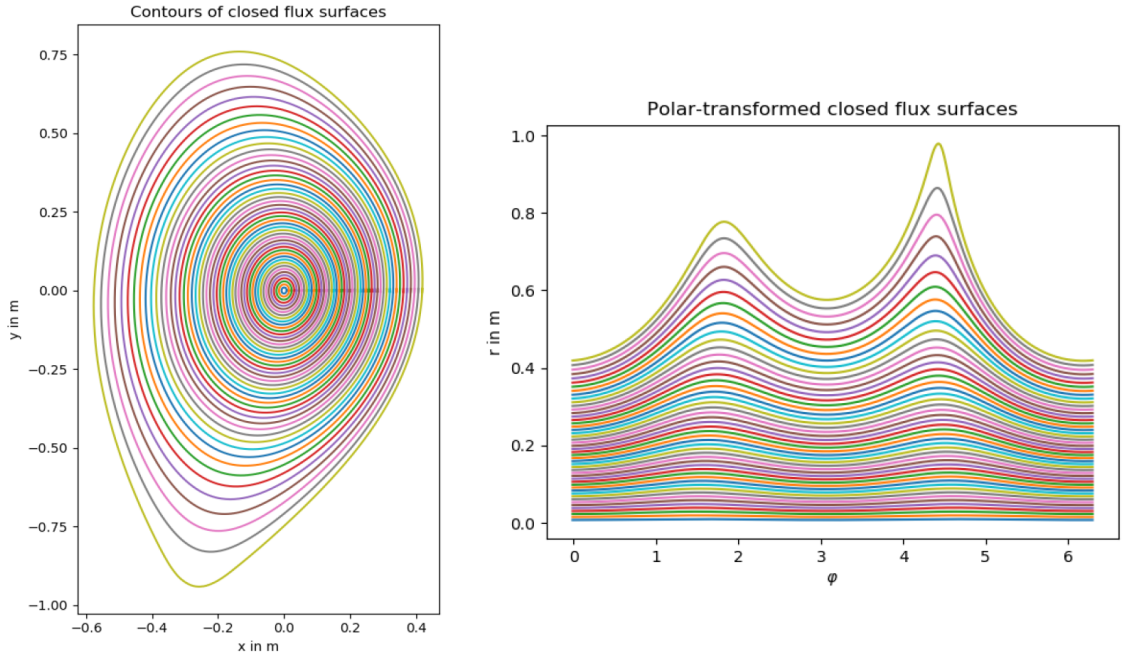

Figure 55: Contours (left) and polar transformed contours (right) for discharge 37055

Equation 90 can now be used to perform volume integrals. For that, the equilibrium for the respective shotfile has to be loaded, which provides discrete values for the flux surfaces which can then be fitted as done in figure 55 (left).

To calculate values like the electron inventory N_e, the respective profile has to be multiplied to the integrand of equation 90.

$$N_e = \int_0^{2\pi} \int_0^{2\pi} \int_0^{z(r)} n_e(r) \cdot (x_{off} + r \cdot cos(\varphi)) \cdot r \, dr d\varphi d\theta \tag{91}$$

Another example of applying this algorithm could be the calculation of thermal electron plasma energy.

$$W_{th,e} = \int_0^{2\pi} \int_0^{2\pi} \int_0^{z(r)} p_e(r) \cdot (x_{off} + r \cdot cos(\varphi)) \cdot r \, dr d\varphi d\theta \tag{92}$$

Lastly, the accuracy of this algorithm should be considered. As for that, the particle inventory of discharge 37056 has been calculated, using a resolution of 5 ms. The calculated data is compared with data from Integrated data analysis (IDA).

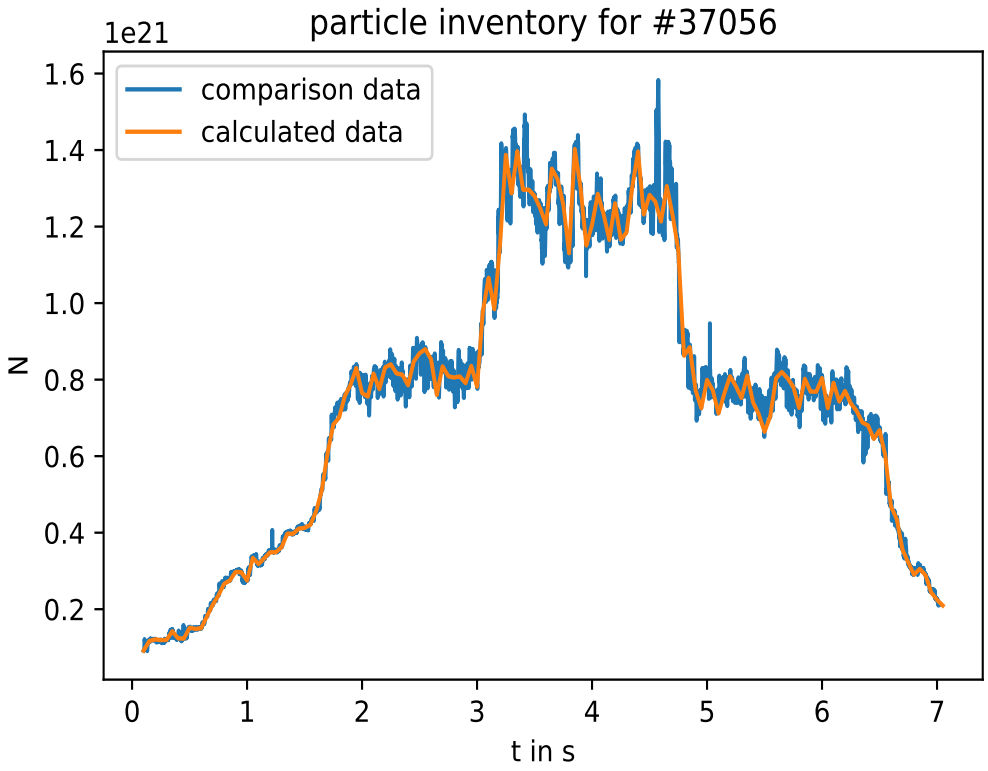

Figure 56: Comparison of particle inventory calculations for discharge 37056

Figure 56 compares the calculated particle content (orange solid line) using equation 91, with the one, provided by IDA (blue solid line). While there seem to be minor deviations, this can be attributed to the fact, that the time resolution of the comparison data is five times higher.

In order to get a bigger sample size, more iterations have been carried out and compared. In several cases, the deviation at identical time stamps has never exceeded 0.5 %.

8.5 Heuristic drift-based model: Particle confinement time τ_p

This segment is dedicated to equation 30 (taken from [4]), which provides a formula for the particle confinement time τ_p. For this specific analysis, formula 30 has been applied to data from discharges carried out for Chapter 5. Therefore, in figure 57, the particle confinement time τ_p is given as a function of the peak-density $f_p = \frac{\Gamma_{plt}}{\Gamma_{tot}}$.

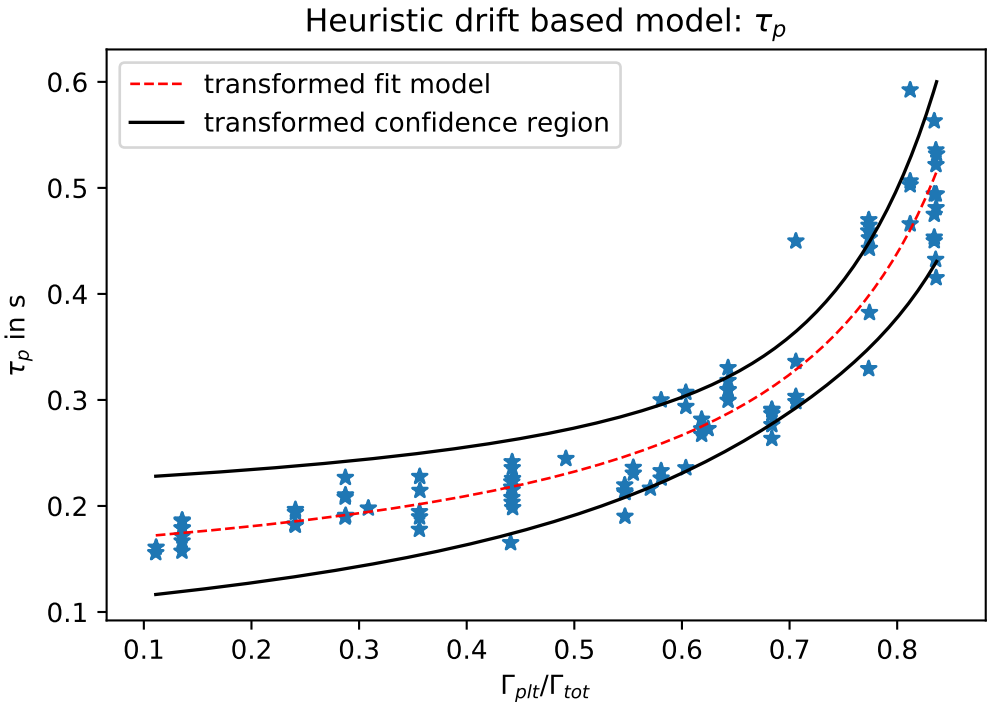

Figure 57: τ_p as a function of $\Gamma_{plt}/\Gamma_{tot}$

The ordinary least square fit and 90 % local confidence bands from figure 57 were obtained by an Odds-transformation of the x-axis, leading to a linear model. It can be seen that the trend of τ_p is similar to the one of $\tau_{p,tech}$, depicted in figure 27 . Therefore, plotting τ_p against $\tau_{p,tech}$ leads to a linear trend with a correlation coefficient of ≈ 0.9:

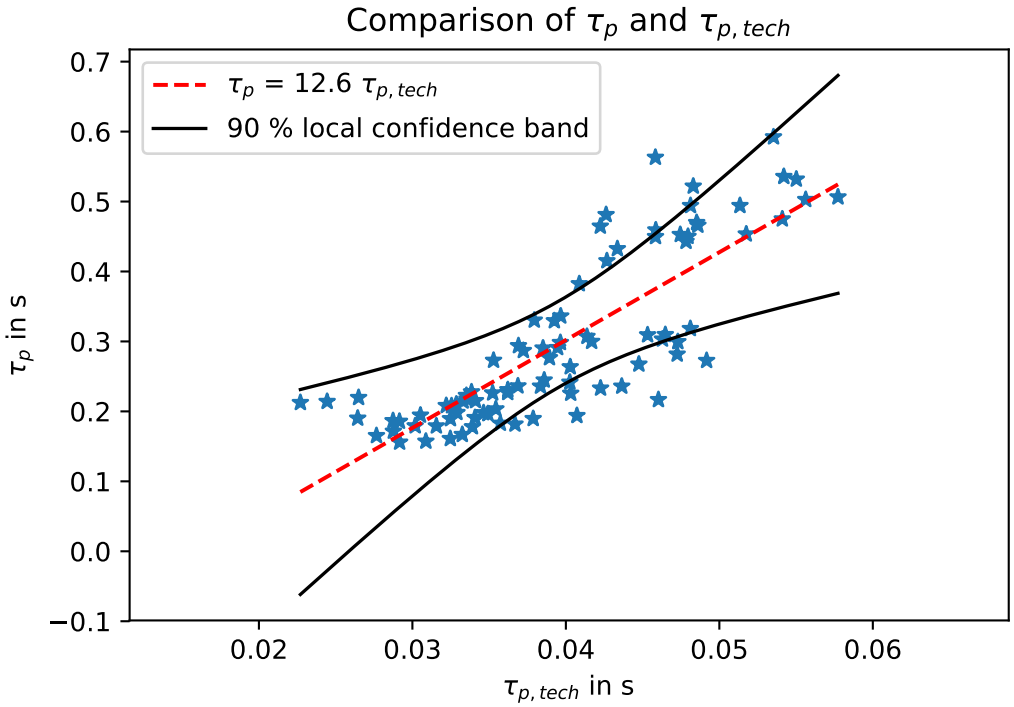

Figure 58: τ_p (eq. 30) as a function of $\tau_{p,tech}$

When considering the linear fit model, given in the legend of figure 58, an marginal offset can be seen. From a physical point of view, this offset is not meaningful. However, since zero lies around the offset within 0.25 standard deviations, it can be argued away.

Due to the strong correlation between τ_p and $\tau_{p,tech}$, equation 30 and its parameters should be considered, if an empirical scaling law for $\tau_{p,tech}$ is designed.

8.6 Estimating N_e by using $\overline{n_e}$

If the electron content of the plasma N_e is needed, a volume integral usually has to be computed. Since those require reliable profiles, information about the equilibrium and often a considerable amount of computing time, a fringe-jump corrected line-averaged density can be used instead, to obtain N_e- values. For the discharges from Chapter 7, plotting N_e against $\overline{n_e}$ (DCK H-0) leads to the following linear trend:

Therefore, the electron inventory N_e is plotted against the line-averaged density $\overline{n_e}$ (obtained from a fringe-jump corrected DCN H-0) for the discharges, which have been

carried out for chapter 5. It should be noted, that the total particle-influx Γ_{tot} was kept approximately constant.

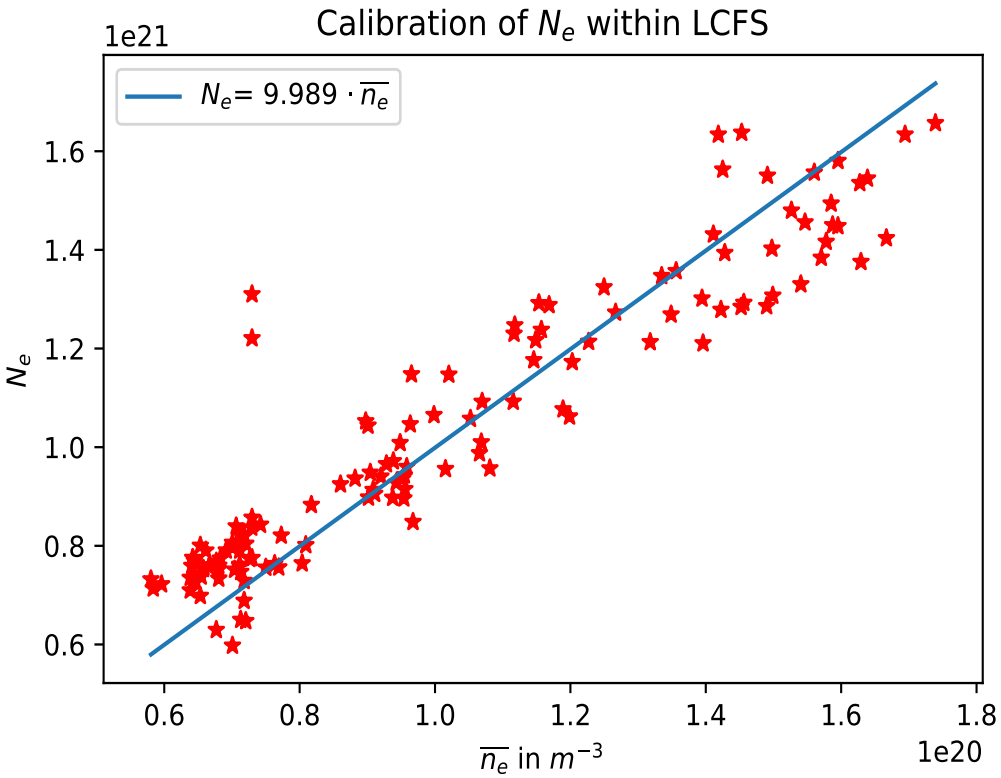

Figure 59: Calibration of N_e using $\overline{n_e}$ from DCN data

Performing a linear regression analysis with the data, illustrated in figure 59, led to:

$$N_e = 9.989 \cdot \overline{n_e} \tag{93}$$

Furthermore, the correlation coefficient for this dataset was computed to be r = 0.92.

It should be noted that, optimal regression parameters were found, when an offset was included in equation 93. However, since zero was within 0.25 standard deviations around the offset and an offset is not reasonable from a physical point of view, the regression was performed without an offset.

Whether this formula is also valid for not keeping Γ_{tot} approximately constant,

will be checked for six further discharges, in which various plasma scenarios (e.g. N-Seeding, High Shaping or technical discharges) were included.

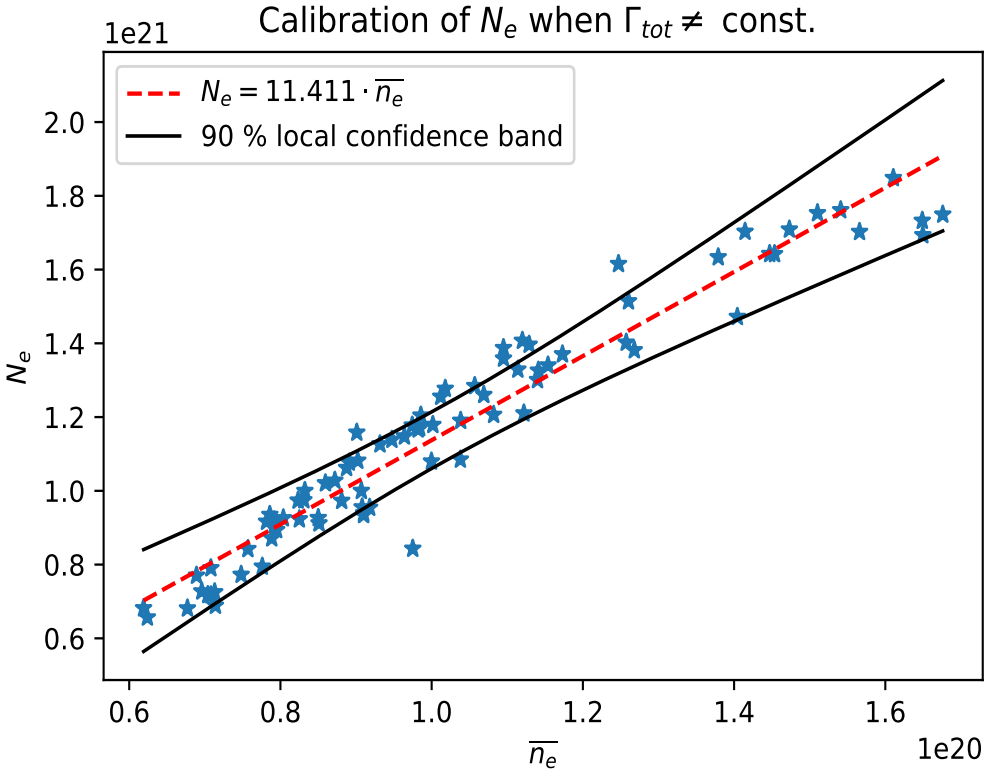

Figure 60: Calibration of N_e, using $\overline{n_e}$. Γ_{tot} was not kept constant

The model, shown in figure 60 is also a linear, with a correlation coefficient of r = 0.97. The model also contained a small offset. However, since zero was within 0.25 standard deviations, the offset was also neglected. As depicted in the legend of figure 60, the slope of this model is slightly higher compared to equation 93. This is likely to be attributed to the fact, that pellet injection was not compensated by a reduction iúb the gas flux Γ_{gas}, which thereby led to a higher particle content (the control of the edge density was, however, lost).

As a consequence of this analysis, N_e when Γ_{tot} is not constant can be given by:

$$N_e = 11.411 \cdot \overline{n_e} \tag{94}$$

With equations 93 and 94 two formulas are given, which can be used to estimate the electron content of the plasma. It should be noted, that these formulas should

solely be used for H-mode discharges.

8.7 Compartment model as a system of differential equations

As mentioned in Chapter 5, a more precise description of the compartment model should be given by considering a linear system of differential particle conservation equations. The system reads as:

$$\begin{pmatrix} \dot{N_c} \\ \dot{N_{SOL}} \\ \dot{N_{plt}} \end{pmatrix} = \begin{pmatrix} \Gamma_{rec} \\ -\Gamma_{pump} + \Gamma_{gas} \\ 0 \end{pmatrix} + \begin{pmatrix} -\frac{1}{\tau_c} & 0 & \frac{1}{\tau_{plt}} \\ \frac{1}{\tau_c} & 0 & 0 \\ 0 & 0 & -\frac{1}{\tau_{plt}} \end{pmatrix} \begin{pmatrix} N_c \\ N_{SOL} \\ N_{plt} \end{pmatrix}$$

To solve this system of differential equations, the Eigenvalues are needed:

$$\det A = \begin{vmatrix} -\frac{1}{\tau_c} - \lambda & 0 & \frac{1}{\tau_{plt}} \\ \frac{1}{\tau_c} & -\lambda & 0 \\ 0 & 0 & -\frac{1}{\tau_{plt}} - \lambda \end{vmatrix} \stackrel{!}{=} 0$$

Which results in a third degree polynomial:

$$\lambda\Big(\lambda^2 + \lambda(\frac{1}{\tau_{plt}} + \frac{1}{\tau_c}) + \frac{1}{\tau_{plt}\tau_c}\Big) \stackrel{!}{=} 0$$

While one Eigenvalue is given by 0, there is a second degree polynomial left. It now depends on its discriminant whether the remaining solutions are real or complex. Complex solutions would indicate a vibratory system. The discriminant is given by:

$$D = \frac{1}{\tau_{plt}^2} + \frac{1}{\tau_c^2} - \frac{2}{\tau_{plt}\tau_c}$$

The sign of this expression now depends on the values of τ_c and τ_{plt} which are not directly available. Within the model of collisionality dominated diffusion, which resulted in equation 70, it has been assumed that the density profile between the radius of pellet deposition ρ_{plt} and the the core is flat ($n_{e,c} = n_{e,\rho_{plt}}$). Therefore, it is a fair

assumption that $D_{core} \approx D(\rho_{plt})$ which means that $\tau \approx \tau_c \approx \tau_{plt}$. As a result, there is only one solution for the remaining polynomial of second order. The resulting eigenvalues are summarized in table 4.

Table 4: Eigenvalues λ

λ	value
λ_1	0
$\lambda_{2,3}$	-1/τ

Since only one eigenvector to the eigenvalue $\lambda_{2,3}$ could be found, instead of another eigenvector, a generalized eigenvector **h** has to be found [80], which satisfies the following equation:

$$(A - \lambda I)\boldsymbol{h} = \boldsymbol{v} \tag{95}$$

where $\boldsymbol{v}$ refers to the eigenvector, which has been found for $\lambda_{2,3}$. Using this method, the general solution for this system of differential equations can be given:

$$y(t) = A \cdot e^{0 \cdot t} \cdot \begin{pmatrix} 0 \\ 1 \\ 0 \end{pmatrix} + B \cdot e^{-\frac{1}{\tau} \cdot t} \cdot \begin{pmatrix} 1 \\ -1 \\ 0 \end{pmatrix} + C \cdot e^{-\frac{1}{\tau} \cdot t} \cdot \left(\begin{pmatrix} 1 \\ -1 \\ 0 \end{pmatrix} \cdot t + \begin{pmatrix} 1 \\ \tau - 1 \\ 0 \end{pmatrix} \right)$$

The particular solution can be determined by either variation of constants or by a specific ansatz which is familiar from linear differential equations of higher degree [81], using:

$$y_p' = A \cdot y_p + \vec{b} \tag{96}$$

where $\vec{b}$ is the inhomogeneity of the system above. Since $\vec{b}$ only contains constants, a special ansatz using eqaution 96 is used for finding A, B and C as particular solution:

$$\begin{pmatrix} 0 \\ 0 \\ 0 \end{pmatrix} = \begin{pmatrix} -\frac{1}{\tau_c} & 0 & \frac{1}{\tau_{plt}} \\ \frac{1}{\tau_c} & 0 & 0 \\ 0 & 0 & -\frac{1}{\tau_{plt}} \end{pmatrix} \begin{pmatrix} A \\ B \\ C \end{pmatrix} + \begin{pmatrix} \Gamma_{rec} \\ -\Gamma_{pump} + \Gamma_{gas} \\ 0 \end{pmatrix}$$

A comparison of coefficients provides the particular solution. Thus the solution of the system of differential equations can be given by:

$$y(t) = A \begin{pmatrix} 0 \\ 1 \\ 0 \end{pmatrix} + Be^{-\frac{t}{\tau}} \begin{pmatrix} 1 \\ -1 \\ 0 \end{pmatrix} + Ce^{-\frac{t}{\tau}} \left(\begin{pmatrix} 1 \\ -1 \\ 0 \end{pmatrix} t + \begin{pmatrix} 1 \\ \tau - 1 \\ 0 \end{pmatrix} \right) + \begin{pmatrix} \frac{\tau}{2}(\Gamma_{pump} + \Gamma_{rec} - \Gamma_{gas}) \\ 0 \\ 0 \end{pmatrix}$$

8.8 Further impurity analysis

To provide additional iterations of 47, figure 61 depicts the tungsten density (GIZ) for four other discharges.

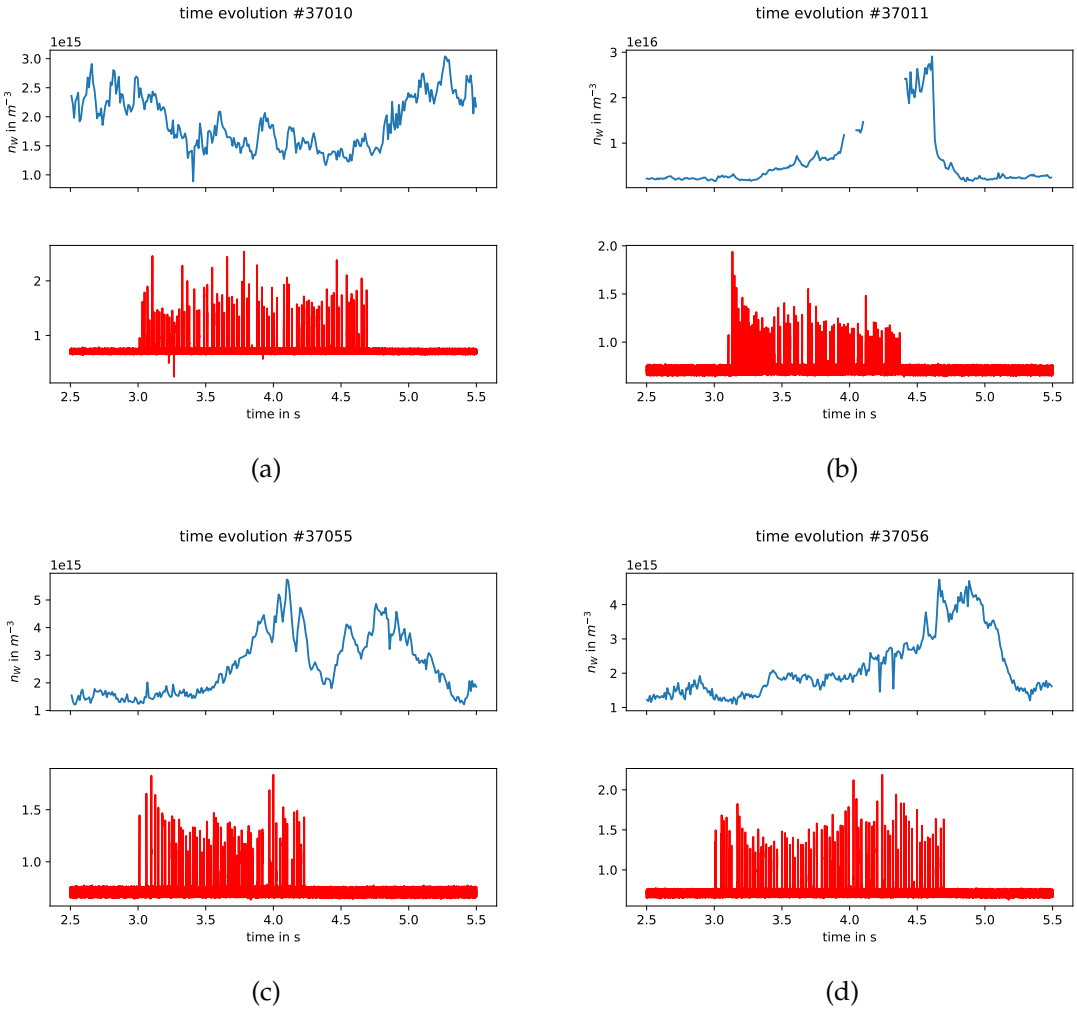

Figure 61: Tungsten density signals for further discharges

Similar to figure 47 the tungsten density n_{Gw} is consistently approximately constant before and after the pellet injection. While there are different behaviours during the pellet injection phase, they cannot be compared in a reliable manner, since the radius of measurement varies as a function of the temperature (figure 46).